Doctoral Dissertation
Doctoral Program in Energy Engineering (33rd Cycle)

Numerical Modelling and Analysis of Combustion in DI and PFI CNG engines:

A study under different EGR dilution and Hydrogen doping conditions

Prashant Goel
****

Supervisor
Prof. Mirko Baratta
Prof. Daniela Misul

Doctoral Examination Committee:
Prof. Tommaso Lucchini, Politecnico Di Milano
Dr. Valentina Fraioli, Consiglio Nazionale della Ricerche/STEMS
Dr. Peter Kelly Senecal, Convergent Science/University of Wisconsin-Madison
Prof. Stefano Fontanesi, Università degli Studi Di Modena e Reggio Emilia

Politecnico Di Torino
June 2021

Declaration

I hereby declare that the contents and organization of this dissertation constitute my own original work and does not compromise in any way the rights of third parties, including those relating to the security of personal data.

Prashant Goel
2021

*This dissertation is presented in partial fulfilment of the requirements for Ph.D. degree in the Graduate School of Politecnico Di Torino (ScuDo).

Acknowledgement

I would like to thank the research group of Prof. Ezio Spessa for providing me this research opportunity. I wish to express my gratitude to my supervisors Prof. Mirko Baratta and Prof. Daniela Misul for their support and suggestions.

My special thanks to Dr. Fredric Ravet and his team (Renault Technical Center) for technical discussions and for hosting me in their research center in 2017. I wish to express my gratitude to the support staff of CONVERGENT SCIENCE GMBH, particularly to Dr. Jyothish Venkataramanan, for their valuable technical support. Whenever I was struck with the software, they went out of the ways to solve the issues.

My acknowledgement goes to all the colleagues that worked with me during this research project and their valuable and fair contribution: Ing. Silvestru Chiriches, Ing. Giorgio De Costanzi and Ing. Antonio De Candia.

My special thank goes to Dr. Ludovico Viglione, Dr. Andrea Bottega, and Ing. Nicola Rosafio for their valuable suggestions in organising a better discussion in writing the thesis.

Last, I wish to express all my gratitude to all my family and friends who stood by me during this research period.

Content

List of Figures

List of Tables

Abstract

The increasing environmental impact and health concerns because of rising greenhouse emissions have pushed global institutions to take necessary measures for a more sustainable future. The road transport sector, which is responsible for 11.9% of global greenhouse gas emissions, has been under special focus for decarbonisation. Natural gas, comprised mainly of methane, can play its role to achieve short-term decarbonization of vehicle fleets as it allows for up to 24% reduction in engine-out CO2 emissions due to its low carbon content. Fast-paced development and adoption of untested technologies for natural gas engines is a crucial factor in meeting sustainable goals. Numerical modelling can play a fundamental role by allowing the optimal development of these technologies.

Within this context, the present thesis is a part of the research work carried out at Politecnico Di Torino within the H2020 'GasOn' collaborative project. The objective of the GasOn project was to develop an advanced mono-fuel natural gas engine, able to comply with '2020+' CO2 emissions targets and with the same performance as that of a diesel engine. The present thesis focuses on the development of the 3D CFD numerical model for evaluating the potential of high charge dilution, hydrogen doping, and a direct-injection given its application on natural gas internal combustion engines which can be applied to achieve the targets.

The thesis is divided into seven chapters. In Chapter 1, an overview of the innovative technologies for high-performance natural gas engines is presented followed by the objectives of this work. Chapter 2 details the experimental setup and engines under investigation whereas Chapter 3 discusses the numerical methodology used in the development of numerical models.

Chapter 4 focuses on the impact of EGR dilution on combustion at different engine load conditions. Firstly, the numerical model was calibrated and validated with experiments, at available working points on a single-cylinder engine in PFI mode. The model was then extended to quantify the EGR dilution limits at low, medium, and full load working conditions. The impact of EGR dilution on combustion and peak burning temperatures is discussed in the last section of this chapter.

Chapter 5 focuses on the Impact of hydrogen addition on the EGR dilution tolerance of an engine. For this numerical model was modified to adapt for the change in laminar flame speeds due to hydrogen addition. The model was validated with experiments available for three

hydrogen fuel blends [0%, 15%, 25% by vol] with no EGR conditions. It was then used to evaluate EGR dilution limits with three fuel blends. The impact of hydrogen addition on combustion is also presented in section 5.3 followed by a summary of the results.

Chapter 6 focuses on the impact of direct injection timing on mixture formation and combustion at full load conditions. First, the numerical model developed in chapter 4 was adapted for a centrally mounted injector. The model was calibrated and validated at full load conditions in PFI mode. After that, the impact of early injection, and late injection timings, on mixture formation and combustion were evaluated. 3D CFD model was also used for quantification of late injection on mixture heterogeneity at high engine speeds at full loads. In the last part of this chapter, the impact of injection timing on volumetric efficiency at the low-end torque range is discussed. Chapter 7 summarizes the main conclusion of this work.

Chapter 1:

Literature review

1.1 Scenario

Human related activities are primary drivers of climate change and at present is one of the world's most pressing concern. Temperature data of near-surface air temperature and sea-surface temperatures have confirmed that the current global average temperature has risen by approximately 0.7°C than the 1961-1990 baseline and by approximately 1-1.2°C from pre-industrial levels [1,2,3]. During the same time, CO2 concentration in the atmosphere has increased from ≈300 ppm to ≈400 ppm [4]. Experts in climate studies gave sufficient evidence linking rising temperature directly to a rise in global greenhouse gas [GHG] emissions [6,7]. The gravity of this situation can be summarized in the statement from an assessment report from 'The Intergovernmental Panel on Climate Change (IPCC) [5]:

"Anthropogenic greenhouse gas emissions have increased since the pre-industrial era, driven largely by economic and population growth, and are now higher than ever. This has led to atmospheric concentrations of carbon dioxide, methane and nitrous oxide that are unprecedented in at least the last 800,000 years. Their effects, together with those of other anthropogenic drivers, have been detected throughout the climate system and are extremely likely to have been the dominant cause of the observed warming since the mid-20th century."

Considering these as the prophecies from Pythia (famous Oracle from Greek mythology), questioning the future of humanity itself, immediate steps in every field of human activities are necessary to address these issues. Nearly every nation has pledged to substantially reduce GHG emissions to limit the global temperature increase to 1.5-2°C above preindustrial levels [8].

The transport sector, being a contributor of 16.2 % of total global GHG emissions [135], has already started its decarbonization drive. Road transport, being the main contributor to mobility, has made some strong steps towards the reduction of CO2 emissions. Tougher regulations on fleet CO2 (g/km) emissions have pushed OEMs (Original Equipment Manufacturers) to search for innovative solutions to meet the targets. With 2020+ CO2 emissions in sight (at the start of this project), the European Commission had set the target to reduce fleet average from 130 g CO2/km to 95 g CO2/km for passenger cars [9]. This meant to focus research on new solutions to reduce CO2 emissions coming from conventional gas or diesel cars. Though new technologies like electric and fuel cell vehicles got a lot of publicity as well as research and development (R&D) subsidies, they are still far away to provide a sustainable answer [137]. To meet the question of future mobility for all, different solutions should be researched. Natural gas (NG) can be a part of the mix, as a bridging technology, due to its potential in reducing direct engine-out emissions, compatibility with current engine technologies, large and widespread availability, and cheaper cost.

1.2 Natural gas

The earliest use of NG has been documented as far back as 500 BC in China where surface seeping gas was used for boiling seawater to extract drinking water. The first commercial use of natural gas occurred in Britain in around 1785 when it was used as fuel for lighthouses and streetlights. Its use in transportation can be traced back to the first and second world wars, where it was captured in balloons and were carried on rooftops of vehicles for use as fuel [10].

Methane, the main constituent of NG is a single carbon saturated hydrocarbon with single bond between carbon and hydrogen. Methane has higher hydrogen to carbon ratio and has high energy content on a mass basis [Table 1.1]. These properties allow for a direct tank-to-wheel CO2 reduction by 24 % relative to gasoline [13] (0.35kg less CO2 per kg of fuel burned) [Table 1.2]. Well-to-tank analysis has also shown that, depending on the fuel chain used, NG generates 11 to 25% fewer emissions per unit of energy than conventional fuels [14,15,16].

Table 1.1: Properties of Methane and Isooctane at 1 atm and 300K [12]

	Methane	Iso-octane
Molecular formula	CH4	C8H18
Hydrogen –to-carbon Ratio [-]	4	2.25
Molecular weight [g/mol]	16.043	114.236
Lower heating value [MJ/kg]	50	44.3
Higher Heating value [MJ/kg]	55.5	47.8
Density gaseous [kg/m3]	0.65	-
Density liquified [kg/m3]	430-470	692
Volumetric energy content[KJ/m3]	3041	3704
Boiling point [K]	111	372.4
Stoichiometric air-to-fuel ratio [kg/kg]	17.1	15
Flammability limits	2-0.6	1.51-0.26
Autoignition temperature [K]	813	690
Mole Expansion (after/before combustion)	1	1.058
Ratio of specific heats	1.354	1.389
AKI	120	100

The physical and chemical properties of NG have their advantages during combustion as well. NG, due to its lower adiabatic flame temperatures (≈1963K, at 1 atm pressure, 293K temp, and stoichiometric fuel-air ratio) compared to liquid fuels (gasoline ≈ 2138), produces lower nitrogen oxide emissions when used in engine conditions. Lower combustion temperatures could delay in achieving light-off temperatures of three-way catalyst (TWC) which can be

detrimental for engine-out unburned hydrocarbons (HC's). However, these issues can be resolved by optimization of precious metal loading on the catalyst brick.

Being a gaseous state under atmospheric conditions, methane has another advantage in terms of miscibility and diffusivity with air compared to liquid fuels. It can adequately form homogeneous mixtures with air without undergoing atomization and evaporation thus reducing chances of locally fuel-rich zones. This property combined with the absence of aromatic compounds in methane reduces the likelihood of particulate matter (PM) formation during combustion.

Table 1.2: Potential and challenges with CNG [13]

Fuel properties	CH4	Gasoline	CNG (+) potentials / (-) challenges
CO2 from 1 kg fuel (tank to wheel)	2.74 kg	3.10 kg	(+) Co2 benefit of ≈11%
Density	0.72 kg/m3	0.75 kg/l	(-) Requires pressure storage (-) Low driving range
Octane rating	> RON120	RON95	(+) Reduced knock (-) demand for higher peak pressure

Despite advantages, NG has its share of drawbacks. NG, due to its three times less density than gasoline, has low volumetric energy density. This limits vehicle range for the same tank volume when compared to gasoline. To reach the same operating range in one full tank, NG requires a large onboard storage capacity. It is generally stored in compressed form at pressures such as 16-25 MPa. It can also be stored in liquid form at low pressure such as 70-210 kPa but due to the lower boiling point of methane, this will require cryogenic set up in the vehicle which can be complex for LDV (Light Duty Vehicle) applications.

Another issue that has been studied by Nguyen et al. [23] is related to the molar expansion ratio (MER) of fuels and its impact on output efficiency. MER is the ratio of the number of moles of products to that of reactants. Consider constant volume combustion, where fuel is burned in a pure oxygen environment. Combustion products are burned and then cooled such that initial and final temperatures are nearly identical. In this case, fuels with a higher MER value will have higher final pressure at the end of cooling compared to initial pressure. This represents the potential to perform additional work on the piston [24,25]. Methane has the MER of unity whereas gasoline is around 1.058 (iso-octane). This would decrease the engine efficiency when fuelled with methane compared to gasoline, for similar operating conditions. However, due to the high knock resistance of methane, a higher compression ratio (CR) is achievable compared to gasoline. This can result in higher efficiencies in methane engines and help overcome some of its drawbacks.

Additionally, the unburned HC's from NG combustion contains a large amount of methane, a very stable compound. This together with lower exhaust gas temperatures, especially at part

loads, causes lower HC-conversion rates in TWC [138]. To obtain the optimum methane conversion rates, optimization of precious metal loading has been performed by various researchers and shown to have achieved good results [139,140,141].

Though NG fuel has its shortcomings, its advantages make it an interesting fuel to be completely overlooked. The drawbacks related to fuel can be resolved using proper technologies and can help in creating an efficient NG engine. Already existing engines based on conventional fuel architectures can be optimized using innovative technologies. Numerical modelling can be used as a virtual test bench to evaluate the impact of design modifications and help in fully exploiting these innovative technologies.

1.3 Natural gas use in engines.

Natural gas (NG) is used in spark-ignited (SI) engines that work as per the otto cycle, where fuel and air are introduced to form a premixed mixture. It is then compressed and burned with the help of electric discharge provided by a spark plug. Following which a turbulent flame develops that propagates through the mixture until it reaches combustion chamber walls and then extinguishes. The mixture is generally kept around stoichiometric conditions so that engine out emissions (CO, HC, and NOx) can be substantially reduced by a three-way catalyst that works efficiently at stoichiometry [17].

SI engines designed for gasoline are highly compatible with NG as well. In the current market, most natural gas engines in operation are retrofitted from gasoline engines. Generally, these retrofitted engines use port fuel injection (PFI) technology where NG is mixed with air in the intake port, with the help of an injector [18]. This gives enough time for the air to mix with fuel and form a homogeneous mixture before the spark event. The use of gaseous fuel such as NG, avoids wall wetting on intake ports and cylinder liner especially during cold start which improves cold startability and reduces engine-out emissions in cold ambient conditions. This is achieved because it is possible to control the air-fuel ratio (AFR) of gaseous fuels compared to liquid fuels (where fuel condensates), especially during cold starts. Although gaseous fuels lack latent heat of vaporization which results in higher temperatures of the piston, cylinder walls, valves, and valve seats as cyclic cooling from fuel evaporation is missing, this issue can be resolved by using heat-resistant materials and some design changes in piston pin, piston pins, and cooling systems [19].

The main drawback of a PFI system with gaseous fuels is that the injected fuel in the intake manifold replaces some of the incoming air. It reduces the amount of intake air per stroke, resulting in a loss of torque. The volumetric loss is pronounced at low engine speeds and part-load conditions. At this engine operating point, low-end torque is significantly affected and impacts vehicle drivability in city driving conditions [11]. Anderson et al. performed vehicle level tests on a chassis dynamometer over several driving cycles with two similar naturally aspirated vehicles and a PFI system with gasoline and CNG [20]. The CR of the NG engine was increased to 12.7:1 compared to the gasoline engine at 10.6:1. Despite higher CR, the PFI

NG vehicle yielded 3-9% lower fuel economy and 21% lower power density throughout the operation.

Another issue with PFI is at low engine speed and part load condition where scavenging plays a significant role in exploiting full engine potential. Increased scavenging can replace residual gases with fresh air, thus improving engine breathing. With the PFI system, an increase in scavenging could result in higher CH4 emissions as some fuel can escape the cylinder along with residual gases [21].

The limitations of the PFI engine in terms of low-end torque and scavenging can be overcome by direct injection (DI) systems, in which NG is injected directly into the cylinder using an injector. Literature showed that with an NG-specific turbocharger, the low-end performance can even exceed that of a gasoline DI engine. Hofmann et al [22] performed experiments comparing the full-load performance of gasoline direct injection turbocharged engines with different NG injection systems. The tests were performed with NG PFI, DI, and DI with optimized turbocharge. Gasoline engine had a CR = 8.8 whereas to exploit the knocking resistance of NG, CR was changed to 13.6 with NG fuelling. Results discussed at full load and under 3000 rpm showed that PFI system performance was lower than all other cases. With NG DI and optimized turbocharger, full-load performance was comparable to gasoline engine with some improvement in the low-end torque zone. Full load torque was realized 500 rpm before that of the gasoline engine.

Husted et al. as well showed similar results in which an engine with a PFI system had 30% lower torque compared to DI mode at engine speeds lower than 1500 rpm. With the introduction of DI, 2/3 of the torque lost due to the PFI system was straightforward recovered, as long as the spark setting is optimized for efficiency [21]. It was shown that by moderate spark advance, the exhaust turbine speeds were increased through higher heat flux in the exhaust resulting in an increase in boost. It was concluded that a DI injection system, where fuel is added directly into the combustion chamber, along with improvement in charge motion and NG specific turbocharging could meet the efficiencies compared to gasoline fuelled engines. The scavenging issue can also be addressed with the DI system as fuel injection can be optimized to achieve better scavenging without loss of fuel into the exhaust system.

Direct injection use with NG engines is an interesting concept with its own challenges. If fuel is injected into the cylinder during the intake stroke, there would be a limited improvement in volumetric efficiency with respect to the PFI system [26]. Song et al evaluated during experiments that the volumetric efficiency improvement with DI comes only if injection time is around IVC or later. For injection from bTDC 330 CA deg to 180 CA deg (early injection), the averaged volumetric efficiency was about 38.6% for DI which was similar to PFI systems. He concluded that fuel injection during intake stroke (early injection), either in port or in the cylinder, reduced the intake air mass. However, the volumetric efficiency was improved by 2.2% with direct fuel injection timing after intake valve closure. Another advantage with DI is the added turbulence inside the cylinder due to the incoming fuel jet. The increased turbulence intensity increases turbulent flame velocity and reduces the combustion duration.

Late injection strategy in NG engines can influence mixture homogeneity, especially during full load conditions. To meet high fuel demand, injection duration is generally longer with current low-pressure DI systems. The choice of low operating pressure injection (in the range of 16-30 bar) is justified as it allows more CNG to be used from the tank and increases the vehicle range [22]. While the strategy of a low-pressure operating injection system is justified, it limits the mass flow rate for a given injector nozzle and thus increases injection duration.

Extensive research has been performed to find out the optimal injection timing for the DI NG engine [11,36,37]. Sevik et al. performed experimental tests to assess the influence of injector location and injection timing on combustion and thermal efficiency of NG DI engines [36,37,43]. The impact of injector location was evaluated for side-mounted and central mounted location. It was concluded that the side-mounted injector was optimal for improvement in the tumble motion, which also led to shorter combustion with an increase in thermal efficiency. Results showed that regardless of injector location, injection events occurring midway through the intake stroke resulted in better thermal efficiency. This injection timing allowed for an optimal trade-off between mixing time as well as preservation of charge motion of gaseous injection events. It was also shown that the DI system improved the charge dilution due to increased turbulence due to the injector jet resulting in lower engine-out emissions compared to the PFI system.

Shinga et al. studied the combustion behavior of NG DI in a rapid compression machine with a CR of 10:1 by varying the SOI at 90 bar injection pressure [39]. In this study, the mixture was introduced by two methods: in PFI and DI mode. It was concluded that NG DI can have a positive impact on the combustion process over the PFI operation. Under stoichiometric conditions, the initial burn duration (theta0-10) and main burn duration (theta10-90) of the combustion event were decreased due to a higher level of turbulence from the gaseous injection. Moreover, DI resulted in a higher combustion efficiency than PFI mode due to less wall quenching resulting from increased turbulence.

Combustion system for NG engines can be divided into a stoichiometric or lean burn approach. In lean-burn technology, the intake charge is diluted by the excess air. The main advantage of a lean-burn engine is that it provides further improvement in fuel economy over stoichiometric NG combustion. Combustion stability in ultra-lean combustion (lambda, λ>1.6) can be achieved by using a premixed ignition chamber [38]. This research is in its nascent stage and will take more time to unlock its full potentials. Also, this option would require changes in exhaust after-treatment or post-fuel injection to maintain the stoichiometric ratio at the exhaust. For commercial use of lean-burn technology, other auxiliary subsystems still need attention.

A combustion system with a stoichiometric air-fuel ratio is a straightforward approach. The already existing three-way catalyst can be used for reducing pollutant emissions, with proper control calibration and TWC optimizations for unburned methane conversion. To control high exhaust temperatures, cooled exhaust gas recirculation (LP-EGR) dilution is the most used method in SI engines. EGR dilution offers an attractive means to further improve engine efficiency and fuel economy as it offers the benefits of charge dilution (lower pumping and

cooling losses) while allowing stoichiometric air-fuel ratio. The disadvantage connected to higher EGR rates is the occurrence of excessive cyclic variation which negatively affects the fuel economy advantages offered. An engine has a limit to tolerate EGR in a fresh mixture. This limit is dependent on the burning velocity of fuel, charge motion, and fuel-air ratio near the spark plug. Kuroda et al. studied the concept of heavy EGR use with a dual spark plug which improved the fuel economy as well as Low NOx emissions [27]. He concluded that dual spark use and increasing swirl inside the combustion chamber can improve EGR tolerance of the engine and can tolerate EGR rates as high as 20% under part-load conditions.

Nakajima et al had similar conclusions that fuel economy gain with EGR dilution is mainly due to reduction of pumping loss, cooling loss, and dissociation [28]. Whereas further increment of EGR rates after a certain limit will increase fuel consumption which is due to increased cycling fluctuations which makes optimum spark timing difficult. However, these EGR limits can be further improved by achieving 'fast burn' through increased turbulence and dual point ignition.

Neame et al investigated the effect of fuel economy improvement using EGR and advanced ignition systems with different fuels (Gasoline, Natural gas, Methanol) [29]. Natural gas has the lowest laminar flame speed out of all the tested fuels [30] and showed the lowest tolerance to EGR dilution (20% EGR rate compared to 40% in the case of Methanol). The use of plasma jet ignition extended EGR tolerance limits until combustion quality exceeded an allowable threshold.

As discussed before, due to the low laminar flame speed (LFS) of NG, EGR addition leads to high cyclic variability in combustion. Moreover, despite the wide lean burn range of NG with respect to gasoline, methane does not allow stable homogeneous combustion beyond $\lambda \approx 1.6$ which limits lean-burn combustion development of NG engines. To extend the EGR tolerance and lean-burn limits for NG engines, the addition of Hydrogen is an interesting area of research. Alger et al. experimented on the single-cylinder engine and found that 1% hydrogen addition by vol can increase EGR tolerance from 20% to 28% for CNG at low load conditions. The tests were limited to low load cases to characterize the benefits of hydrogen-enriched EGR for stoichiometric heavy duty NG engines [31].

Besides improving EGR tolerance, Hydrogen addition offers advantages in fuel economy benefits and emission reduction as well. Experiments performed on a Chevrolet engine by Wallace and Catellan showed that a blend of 85% methane and 15% Hydrogen allowed for reduced brake specific fuel consumption and HC emissions while still maintaining the same level of NOx [32]. Other researchers have shown that Hydrogen addition increases NOx emissions but has a positive impact in reducing HC, CO, and CO2 emissions [33,34,35]. The reduction in HC emissions is not only due to the reduced carbon content of the fuel mixture but also to high combustion efficiency and smaller quenching length of Hydrogen.

The optimization of the best technologies suitable for a specific engine architecture would require trials on an engine test bench. Physical experimentation of all possible designs could

lead to increased product development time. To understand the impact of certain technology on an engine, numerical modelling can be used as a virtual test bench which provides an option to make quick design changes and optimize the design phase.

1.4 Numerical modelling applications in optimization of NG engines

Numerical modelling has been used in past to optimize the in-cylinder flow of a 3.5L V6 Ford EcoBoost engine [40]. Numerical models were experimentally validated for select hardware configuration. For part load conditions, a series of port blockers were used to increase the tumble ratio. It was observed that an increase in tumble was beneficial for stable combustion due to higher turbulence intensity achieved at TDC. This resulted in higher flame speeds with the reduction in cyclic variation. It was also shown that the start of injection (SOI) has an impact on the in-cylinder turbulence. Simulations were performed by delaying SOI which led to a more developed tumble motion at TDC. Due to this tumble motion, higher turbulent kinetic energy at spark timings was achieved which led to faster combustion. But too much delay in SOI also led to higher mixture heterogeneity resulting in poor combustion.

In the work of Douailler et al., the effect of NG DI on a high CR NG SI engine was investigated [45]. Numerical simulations were performed to optimize the piston and combustion chamber shape to achieve higher in-cylinder turbulence. Models were then used to account for the impact of SOI timing on the volumetric efficiencies of the engine. it was concluded that late injection timing would result in better volumetric efficiencies with a compromise on mixture homogeneity. Results showed that the PFI NG engine had 9% less power output compared to the PFI gasoline engine while the DI NG engine was comparable due to improved volumetric efficiency.

Numerical studies have been performed in the Polito CFD research group on different engine configurations. Polito has been involved in the development of direct injection natural gas engines through various collaborative projects such as ‘InGAS’, ‘BioMethAir’ and European Project ‘GasOn’ with main focus on numerical modelling of DI. This created a knowledge base for direct injection modelling with different injector geometries.

In the work of Rapetto [41], a numerical model for DI was developed and validated against PLIF images obtained in collaboration with AVL. This study was focused to analyse the mixture formation processes with DI. Mixture formation for different injection timings from EOI 220 CA deg bTDC till 50 CA deg bTDC were analysed. The methodology adopted for CFD modelling was discussed. The model accurately captured the DI flow structures of an under-expanded jet. It was able to capture the periodic shock structures and was able to validate numerical results with experimental PLIF images. CFD model was used to describe optimal injection timings in different engine operating conditions in terms of mixture formation. Using a numerical model, he confirmed that the nozzle pressure ratio exerts a strong influence on the jet configuration. At high load conditions, he showed that a strong interaction between the injected fuel and charge motion exists, in particular, the fuel jet is strongly deviated by the

inducted air. He also studied the impact of injector protrusions on jet behaviour. It was shown that an optimal protrusion of the injector nozzle had an impact on mixture formation.

The work of Viglione [42] was developed in collaboration with FIAT, CRF, and AVL under the BioMethAir project. The objective was to numerically investigate a high-efficiency natural gas engine through the optimization of the in-cylinder charge motion. He focused on the optimization of the cylinder head design to deliver the best possible charge motion, suitable for high compression, high tumble engine. The work was performed by developing a CFD model to evaluate the effect of intake masking on tumble formation and volumetric efficiency. He further developed the model to evaluate the impact of CR in terms of fuel economy benefits. He found that CR=13 was a good compromise between desired fuel consumption reduction and cyclic variability. Further simulations were performed on the optimized cylinder head and CR with a side-mounted DI model in full engine geometry. A side-mounted DI injector was tested for two different injector orientations. It was found that the configuration which assisted tumble motion was effective in promoting the mixing process as well. It was concluded that early injection was good for homogenous mixture while late injection with a side-mounted injector increased the turbulence intensity. The conclusions of this work were coherent with experimental work performed in [43].

The work of Xu [44] was to develop an experimentally validated numerical model for a downsized high-performance engine fuelled with dedicated CNG. The study investigated the mixture formation process in PFI and side-mounted DI engines. Following previous work, a numerical methodology for suitable mesh optimization to capture the correct Mach disk position and shock structures was used. The direct injector numerical model was validated against schlieren optical images. The model was able to capture the three distinctive jet development stages. The first stage was described as the formation of toroidal vortex ring as jet issues from the nozzle followed by the enlargement of the vortex ring and its convergence towards the jet centerline. The final stage was described by the vortex shedding phenomenon which results in loss of jet asymmetry. The injector model developed was used in a full engine to study the mixture formation for side-mounted configuration. Mixture formation was studied for different injection timings and discussed in detail the mixture formation for different working points.

1.5 Summary

The potential of natural gas as an alternative fuel has been extensively researched in the past few decades. Researchers have shown that the full load capability of an NG engine is comparable to that of gasoline. The use of high CR with NG has increased the possibilities of efficiency improvement, due to the high knock resistance of the fuel. As noted in previous studies, the PFI system has poor part-load capabilities due to air displacement in the intake manifold. A part of this power loss can be recuperated using turbocharging. In gasoline engines, the issue of high temperature at full load conditions is solved by mixture enrichment. In an NG engine, enrichment of fuel does not bring the same cooling effect due to lack of latent heat of vaporization. On one hand, the fuel economy benefits of this are clear, the issue to control high

temperature would need another approach. EGR dilution is among the most used approach in current engines. It is also clear from the literature that EGR tolerance with Hydrogen addition with NG can be improved with benefits in emission and combustion efficiencies as well.

Literature has shown that EGR dilution can help achieve better engine efficiencies by reducing pumping losses and NOx emissions in stoichiometric NG engines. In addition to that, at full load conditions, EGR provides an opportunity to control peak combustion temperatures, allowing to optimize spark timing for maximum output. This issue will be addressed in this work where EGR dilution limits using a numerical modelling approach will be explored. In addition to that, the numerical modelling approach will be extended to evaluate the impact of H2 addition on combustion characteristics and EGR dilution tolerances.

Direct injection is another area of improvement that has shown good capabilities at full load conditions. Extensive work has been performed on optimizing the injection timings with NG DI. Injection timing has a crucial impact on combustion characteristics. The SOI dictates the air trapped mass inside the cylinder, ultimately affecting volumetric efficiency. With injection timing during the intake stroke, results showed no volumetric benefits compared to the NG PFI engine. Though injection during compression has shown improved volumetric efficiencies, it can also impact the mixture formation due to restriction in the time available for mixture formation. With DI, injection jet increases in-cylinder turbulence intensity. While the added turbulence is helpful in mixture formation, its interaction with in-cylinder air motion can sometimes be detrimental to combustion progress. The aspect of injector orientation on the cylinder head is another factor that has been studied in the literature. Injector orientation has a direct impact on the evolution of in-cylinder tumble in SI engines.

Across literature sources, numerical modelling has also been extensively used for the optimization of in-cylinder flow and DI of NG. Numerical modelling was used for optimization of tumble motion, DI timings and mixture formation. However, the issue of combustion coupled with DI injection of NG has not been explored in the literature. In this work, combustion has been coupled with DI event to numerically quantify the impact of mixture heterogeneity on in-cylinder events. To achieve this, ECFM-3Z combustion model was successfully adopted in this work with DI injection of NG. ECFM-3Z combustion model was coupled with tabulated laminar flame speed tables which further improved the flame speed prediction. To simulate spark event, state of the art spark ignition model (ISSIM) was used to accurately capture the spark event. Additionally, higher order numerical schemes and more refined techniques for meshing were used due to the availability of higher computational resources within adequate time.

The numerical model was developed for a new engine configuration with the focus to study the impact of injection timing on in-cylinder turbulence, charge motion, mixture formation, and combustion for a centrally mounted injector fuelled with NG. This thesis work is part of a collaborative project which aims to develop innovative technologies for a highly efficient NG engine and will be discussed in next sub-section.

1.6 GasOn Project Objectives

Current work is part of the work performed in a research project funded by the European Commission. The project was focused on the development of an advanced dedicated CNG engine that would be able to comply with the 2020+ CO2 emission targets. The direct benefit from NG combustion would help achieve 20% CO2 emission reduction with respect to the current best in class NG vehicle. H20202 GasOn [46] project has been preceded by the 'InGas project' and is aimed to utilize the lessons learned.

In the GasOn Project, working group 4 was composed of Renault, IFPEN, Continental, FEV, Politecnico Di Torino (Polito), Czech technical university, Universitat Politecnica De Valencia and CEA. The objective of this group was to develop a high-performance NG engine with the same performance as that of a diesel engine. A 27% reduction in CO2 emissions over its diesel counterpart was targeted with improvement in engine and vehicle technologies. The proposed system design for the engine and vehicle are shown in figure 1.1 below.

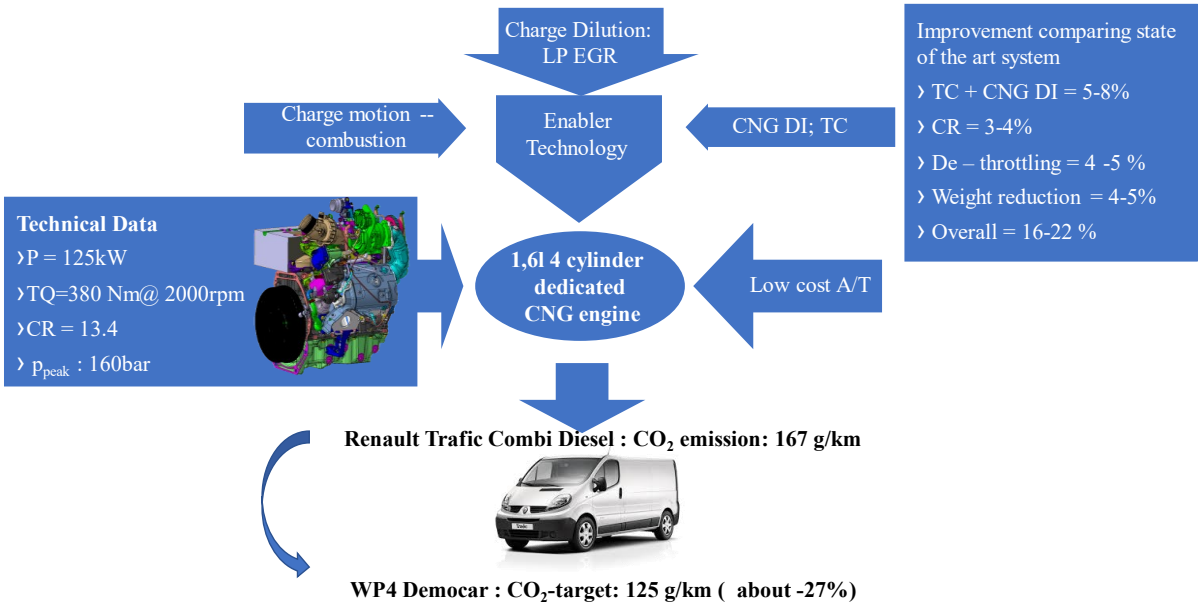

Figure 1.1: GasOn- Working group 4 Project overview

To achieve targets from the engine side, innovative technologies (as discussed in the Literature review) were to be introduced and accessed. First, Stoichiometric combustion was chosen over lean-burn combustion to ensure efficient conversion of pollutant emissions using a three-way catalyst (TWC). Along with this, EGR dilution was envisioned to improve indicated efficiency and output power. This is due to further stretch in knock limit, besides benefits from NG, at high load and high engine speeds. EGR also helps to control exhaust gas temperatures and allows optimization of spark timing to achieve full load performance. Besides this, high EGR dilution also permits to improve indicated efficiency at low loads thanks to the de-throttling

effect which leads to reduced pumping work and heat transfer losses. Finally, EGR at stoichiometric conditions is compatible with conventional TWC.

NG combustion is intrinsically slow and EGR dilution would be further detrimental for this. So the fast-burning solutions were required to efficiently use EGR in this engine. Another issue that needed attention was mixing between NG and air in DI mode. For this, the cylinder head design was changed to improve turbulence and turbulent kinetic energy inside the cylinder. This work was performed by Renault and IFPEN starting from the Mogador project (a bilateral project between the two) [45]. The cylinder head design was optimized by changing the shape of intake ducts. The trade-off between tumble number and permeability coefficient was optimized to achieve the best results [47]. The compression ratio (CR) of this engine was optimized to 13.4:1 to take advantage of the high knock resistance of NG. To increase the specific performance similar to that of the Diesel engine, turbocharging was also required. This would help improve the low-end torque of the engine. These design optimizations led to a high turbulence engine and is described in detail in section 2.1.

Polito research group was responsible for developing numerical models to aid in the optimization of EGR dilution rates at different engine load conditions. Along with this, Polito was given the task to assess the effect of injection timing on mixture homogeneity and its impact on combustion at different engine working points with centrally mounted injection (as was located in this engine).

1.7 Present work objectives

The present work discusses the results of the research activity performed in the GasOn project at Politecnico Di Torino.
With the context of design optimization of NG DI engine, the following aspects were numerically assessed:

- The impact of high intake turbulence on EGR dilution limits achieved through the optimization of the cylinder head
- Quantification of EGR dilution tolerance at low, medium, and full engine loads
- Impact of EGR dilution on combustion
- Impact of hydrogen addition on EGR dilution tolerance
- Effects of direct injection timing on mixture homogeneity and combustion at low-end engine speeds, full loads
- Quantification of mixture breakdown limits with late injection timing at high engine speeds, full loads
- Effects of injection timing on low-load case especially at low-end torque range

Chapter 2

Engines and Experiments

2.1 High turbulence engine

The engine under study has been derived from Renault 1.6L 4valve diesel engine architecture and is used to evaluate the dedicated CNG combustion. The use of a high compression ratio with CNG has been possible because of its fuel characteristics and high-octane number which is helpful in knock resistance. The combustion chamber design has been revised including air induction ports to allow high tumble motion inside the cylinder. This was developed to maximize mixture formation and is beneficial in increasing the EGR tolerance of the engine [Table 2.1]. This engine will be referred to as 'new engine design' in the results section. The experiments were carried out on a single-cylinder engine with a displacement of 405cc and a compression ratio of 13.4. Experimental test setup and results are discussed in sub-section 2.1.1.

Table 2.1: 'New engine design' details:

Engine displacement	405 cm^3
Bore / Stroke	80 mm / 80.5 mm
Compression ratio	13.4:1
Piston	Central shallow bowl
Ignition system	Mercedes Coil (90 mJ) NGK spark plug (ILZKR8A)
Intake valve	Opening duration = 169 CAD / maximum lift = 8.5 mm IVO = -6 ATDC / IVC = -5 ABDC
Exhaust valve	Opening duration = 200 CAD / maximum lift = 8.5 mm EVO = +38 BBDC / EVC = -18 BTDC
Fuel system	Continental CNG-DI prototype
Engine limits	Average max. cylinder pressure = 160 bar Average max. cylinder pressure + 2 σ = 180 bar Max air pressure = 3 bar Maximum exhaust temperature = 850° C

2.1.1 Experimental setup and Results

An experimental campaign was performed by IFPEN and Renault on a single-cylinder prototype engine (with a new engine design) on the engine bench. Air was delivered to the system from the grid which was compressed at 7bar. To simulate turbo boosting at different engine speeds and loads, the pressure was controlled by using sonic nozzles which were connected to surge tankA [Figure 2.1]. Air would expand at the nozzle outlet and then further in Tank A and air temperature would drop. Air was heated before allowing air to enter the engine such that air is delivered at temperature representing turbocharged conditions. Micromotion CMF010 Coriolis type mass flow meter was used to measure fuel mass flow rate. Exhaust backpressure was controlled with the help of an exhaust backpressure valve which represents back pressure coming in actual conditions due to the turbine, after-treatment system,

exhaust pipe, etc. A low-pressure EGR (LP-EGR) line was used along with an EGR cooler and compressor to represent the real working conditions of exhaust gases before mixing with inlet air. In-cylinder pressure was monitored by a flush-mounted cooled AVL QC34D pressure transducer. During measurement, 100 consecutive cycles were measured at 0.1CAD interval. The ensembled average pressure has been used for the calculation of combustion parameters as well as for validation with the numerical model. Exhaust gas composition such as (HC, CO, CO2, O2, and NOX) was measured using an AVL AMA4000 analyser.

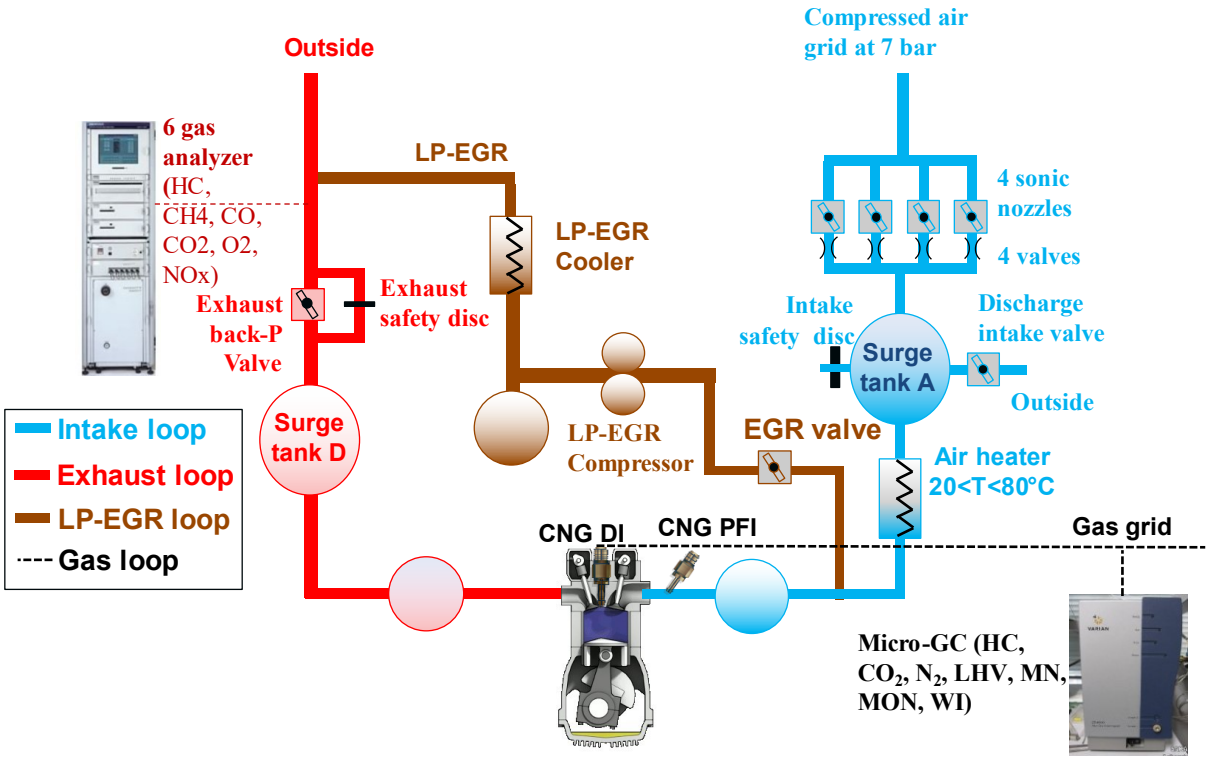

Figure 2.1: Experimental bench setup performed at IFPEN

LP-EGR tests were performed at 2000 rpm and low load to validate the high dilution tolerance with 'new engine design'. The LP-EGR tests were extended for high loads to quantify the improvement in exhaust gas temperatures and knock mitigation capability. Figure 2.2 shows the results in 2 conditions, without and with 20% LP-EGR. Figure 2.2-(a) shows that the addition of LP-EGR has led to an apparent reduction of pumping work due to engine de-throttling. MGB50 (figure 2.2-(b)) presented are cycled average values, evaluated using single zone heat release analysis [110]. As can be seen, in the case of EGR addition, an optimal combustion phasing was not achieved. This was due to the high cyclic variation obtained in the EGR case and consequent difficulty in detecting combustion phasing in real-time. Moreover, higher vibrations in single-cylinder engine played their part in spark timing optimization. At full load, spark timing was retarded to limit peak exhaust gas temperatures. Break specific fuel consumption (BSFC) with EGR is negatively impacted at 3 bar Imep due to high cyclic variations and non-optimal MFB50 phasing.

The addition of EGR has increased specific unburned hydrocarbon (ISHC) by 70% as per expectations whereas specific Nitrous Oxide (ISNOx) emissions have been reduced with EGR

dilution. EGR dilution has an impact on exhaust temperatures downstream of the cylinder head. 20% EGR has reduced exhaust temperatures by 50degC at full load. However, cyclic variability in Imep (CoV Imep) with EGR addition has increased due to slower combustion and MFB50

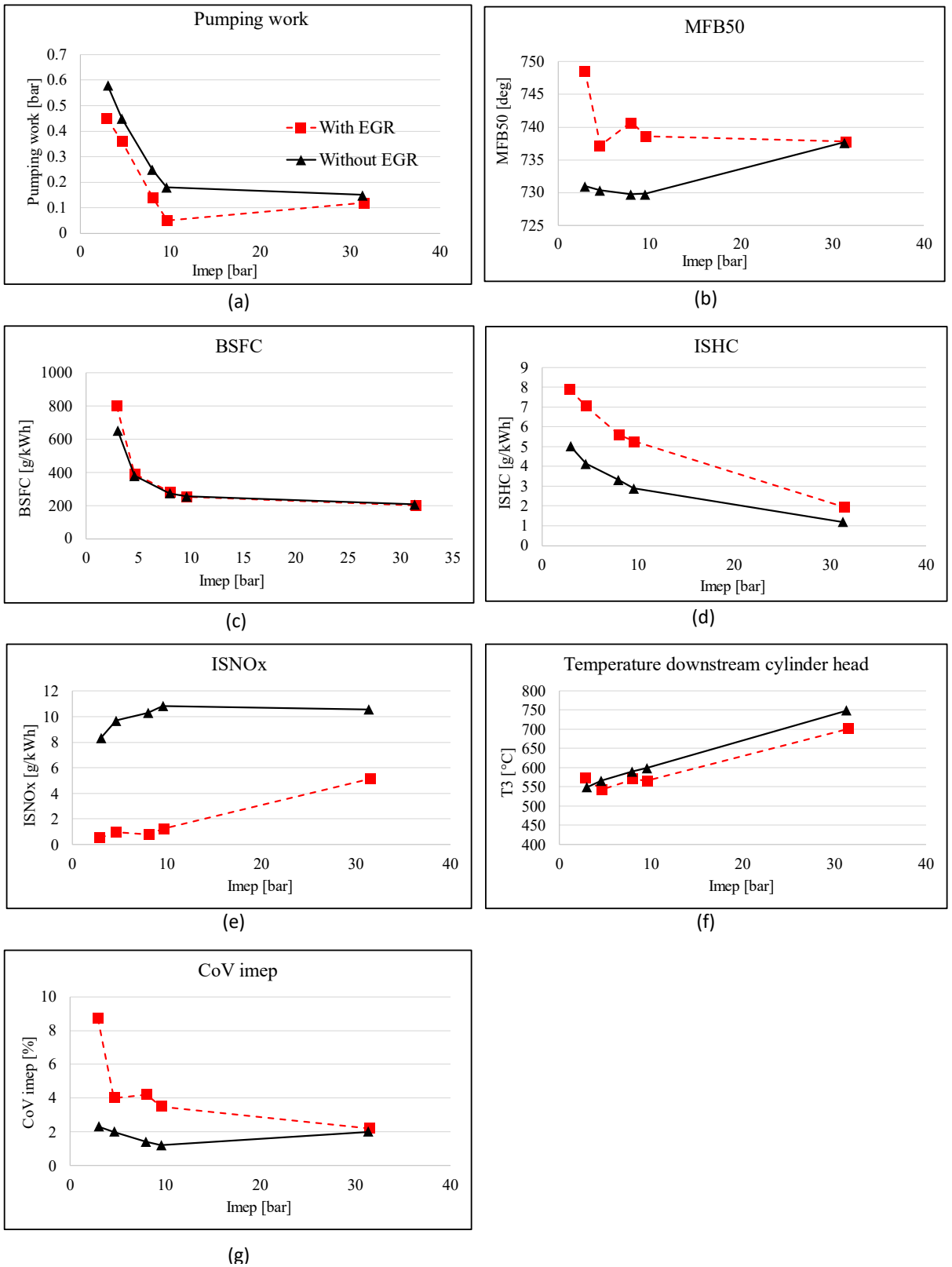

Figure 2.2: 'New engine design'-Experimental results from single cylinder engine tests performed with and without EGR

optimization. This variability is more apparent at low loads. At high speeds, due to higher in-cylinder turbulence, combustion speeds are higher and thus lower cyclic variability.

These experiments were used for the validation of the numerical model developed to quantify the EGR tolerance limits. During experiments, high cyclic variation was observed above 20% EGR. As experiments were performed on a single-cylinder engine, the optimal spark timing with EGR was difficult to detect in real-time. Literature suggests that with increasing EGR quantity, spark timing needs to be advanced to allow extra time for combustion to grow and achieve the maximum brake torque (MBT) spark timing [17,48]. It can be seen from figure 2.2-(b) that during experiments, the MFB50 timing was difficult to optimize. At 8 bar Imep with 20% EGR, MFB50 was 10 CA deg reduced compared to 0% EGR. In this numerical work, spark timing was optimized to keep MFB50 constant to that of MBT timing represented by without EGR case.

To evaluate the improvement of high turbulence 'new engine design' on combustion characteristics with EGR dilution, results are compared with a conventional NG, low turbulence engine. Details of 'Low turbulence engine' are discussed in the next sub-section.

2.2 Low Turbulence engine

The engine is a 1.4L turbocharged FIAT engine, designed to run on CNG. The main specifications of the engine are listed in Table 2.2. Experiments were available on this engine with CNG at different engine speeds and load conditions. Engine bench tests were performed on 'Low turbulence engine' with different amounts of hydrogen (H2) added to NG [0%, 15%, and 25% by volume]. A test matrix of engine and load conditions was designed, and tests were performed under MBT timing. Air was controlled to keep stoichiometric conditions, with no EGR. As the experimental campaign was part of previous research [115,116], they are used as the starting point for this work. The testbed was equipped with a "Degussa Hartmann & Braun" hot-film air mass sensor in the intake system. Air-fuel ratios were taken using two "NGK" universal exhaust gas sensors dedicated to the rich mixtures and lean mixtures field in the exhaust system. A pressure sensor in the injection rail; a hygrometer in the intake system; and several thermocouples for measuring the temperatures of the intake flow, the fuel, and the exhaust gases. Pressure time histories are captured using water-cooled piezo-electric transducers installed in each cylinder, allowing insight into cylinder-to-cylinder variation. The engine speed was measured by means of a crankshaft-driven encoder, which also generated the time base for the acquisition system. The test facility includes a "Fisher-Rosemount" exhaust-gas analyser. This is a multipurpose analyser that can measure the levels of THC, methane unburned hydrocarbon (MHC), NOx, CO, CO2, and O2 in the exhaust gases for gasoline, diesel, or alternative fuel (such as liquefied petroleum gas (LPG) and CNG) operations. All the measuring instruments were connected to a PC-based "National Instruments" data acquisition system allowing for the simultaneous acquisition of the major engine working quantities. A high-frequency acquisition card enabled measurements of the in-cylinder pressure-time history to be recorded over the whole engine cycle.

Table 2.2: 'Low turbulence engine' details

Low turbulence Engine	
Cylinder displacement	342 cm3
Bore / Stroke	72 mm / 84 mm
Compression Ratio	9.8:1
Valves per cylinder	4
Combustion chamber	Pent-roof
Intake valve	Opening duration = 250CAD / maximum lift = 7.5mm
Exhaust valve	Opening duration = 244 CAD / maximum lift = 7 mm
Injection system	Port Fuel injection
Turbocharger	Wastegate-controlled, fixed geometry turbine

Experiments on 'Low turbulence Engine' are used to develop a numerical model for this engine. Results from the model are used to compare EGR tolerance improvement with 'new engine design' in sub-section 4.2. Furthermore, as experiments on this engine were available with different fuel blends of H2 added in NG fuel, it is used as the base engine for evaluation of hydrogen addition on EGR tolerance in section 5.

Chapter 3

Methodology

The numerical model developed for the current work has been the steppingstone for the investigation required to meet the objectives of the present work. The numerical model was to be used for the EGR dilution tolerance prediction under homogeneous charge conditions on 'new engine design'. EGR was premixed with the incoming air-fuel mixture and was burned at optimal spark timing. Combustion behaviour in an engine is highly dependent on the turbulence levels inside the engine, especially near the spark plug location. As the engine under study has high intake turbulence, thanks to the modified cylinder head, it was important to accurately capture in-cylinder turbulences with the numerical model. With high EGR tolerance, the complexity in combustion behaviour further increases as EGR slows down combustion speed. So, the choice of the combustion model was depended on its capability to adjust the flame speeds with the change in fuel and EGR rates. The research work was extended to quantify the impact of hydrogen addition on EGR tolerance on 'Low turbulence engine'. Accurate modelling of hydrogen flame speeds with different residual gas content was another requirement to be delivered by the model.

Furthermore, the same numerical model was to be used for the DI injection timing investigation. To achieve this, engine geometry was modified by adding an outward opening poppet valve at the cylinder head in a centrally mounted location. Simulations were to correctly capture the impact of injection timing on in-cylinder turbulence and its impact on combustion. To achieve this, accurate modelling of the interaction of injector jet with in-cylinder tumble was important as it rearranges turbulence structures inside the engine and affects mixing. It was necessary for the model to capture mixture behaviour under different engine operating conditions as well. Furthermore, combustion was simulated to quantify the impact of mixture distribution on engine performance. Apart from the requirements mentioned, the computational time is the one that tips the balance between accuracy and speed. It was necessary to optimize both for the given computational resources.

In this chapter, the choice of numerical schemes to achieve forementioned requirements has been described. First, section 3.1 deals with the turbulence model used followed by the combustion model in section 3.2. This section also discusses the reason for the choice of ECFM-3z combustion model for highly turbulent and high EGR dilution case. In this same section, adoption of tabulated flame speed model has also been discussed. Section 3.3 details the engine geometry and meshing strategies followed by grid dependency tests. In the last section, the cyclic variation in URANS observed during this work has been discussed.

3.1 Turbulence model used

In Internal combustion engines, a highly compressible and transient flow field is accompanied by geometric complexities. This makes turbulence prediction a difficult task for IC engines. In

cases with direct injection, the bulk gas motion and turbulence characteristics of in-cylinder flows are one of the major factors that control air-fuel mixing and combustion. Inlet port, valves and cylinder head geometry influence the mass flow rate and charge motion. During the intake stroke, air enters inside the chamber creating large rotating flow patterns which are geometrically confined between piston, cylinder walls and cylinder head. These large rotating flows decays and break down into small scale turbulence motions. This turbulence enhances the mass, momentum, and energy diffusion. The correct prediction of these quantities is fundamental for a good simulation [17,49].

Generally, there are three methods for turbulent flow prediction: direct numerical simulation (DNS), large eddy simulation (LES) and Reynolds average Navier-Stokes (RANS) simulation. DNS compute the mean flow and all turbulent velocity fluctuations. The unsteady Navier-Stokes equations are solved on the spatial grids that are sufficiently fine that they can resolve the length scale at which energy dissipation takes place (Kolmogorov length scales). Time steps in DNS are such that they can resolve the period of fastest fluctuations. This approach is also limited to flows with low-to-moderate Reynolds numbers and is highly costly in terms of computational resource requirements.

In LES, the equations are solved for a filtered velocity field which represents the large-scale turbulent motions. The influence of smaller-scale motions is modelled by a sub-grid turbulence model. Equations are solved in unsteady flow field which are quite demanding in terms of computations as well. Also, Numerical schemes still need work to be compatible with LES model.

RANS is based on ensemble-averaged governing equations that calculated mean flow and the effects of turbulence on mean flow properties. Reynolds stress tensors, that appear due to averaging, must be closed using models. The computational resources required for reasonably accurate flow computations are modest.

LES offers advantages for engine simulations, including higher-fidelity and prediction of cycle-to-cycle variation compared to the RANS method. However, the availability of computational resources and objectives in the current work led to the choice of RANS.

RANS method is widely used in the CFD community for engine application. Many research groups are using RANS based approach for SI and CI engine applications [50-53. 124-126]. As experimental results are ensemble-averaged, to mitigate white noise or instrumental errors, the RANS approach suits well to be used for predicting average flow parameters.

In this work, the RNG k-ε model closure model is chosen to close Reynolds stress terms. In this model, k (turbulent kinetic energy) and ε (viscous dissipation) transport equations are derived from the Renormalization Group Theory. This closure model has been shown to work quite well in predicting engine performance parameters and it is widely used for combustion system optimization and design using CFD simulations [52,54,55]. In the context of engine simulations with NG and EGR dilution, researchers have used this turbulence model with good overall accuracy [56,57]. RNG k-ε model has also been evaluated for direct injection of NG.

Scarcelli et al. [58] compared different RANS k-ε closure model predictions with experiments for under-expanded gaseous jets. He concluded that all numerical models were able to predict the Mach disk location and jet width with some accuracy. However, Standard k- ε with higher-order discretization provided the highest accuracy in terms of jet width in the near field, in the far field region, all models were comparable. In this work, combustion simulations were to be performed with DI of NG in an engine environment. RANS with k-ε closure model works reasonably well for engines and DI mode and thus was chosen as the closure model.

3.2 Combustion model

Classically, RANS engine combustion models have been divided into premixed combustion model for SI engines and non-premixed combustion models for diesel engines. In Premixed combustion, the cylinder is filled with premixed air and fuel charge. A spark plug discharge is used to generate a small spherical propagation flame between electrodes which propagates in the combustion chamber until it has consumed the premixed fresh charge.

3.2.1 Premixed Turbulent combustion

Combustion modelling in a premixed turbulent combustion environment is a topic of continuous research. It is quite difficult to exactly model the flame behaviour interaction with turbulence. As 'new engine design' has high turbulent intensity (due to cylinder head design), it was important to choose a model which accounts for various physical attributes of flame-turbulent interaction. These interactions include flame stretch and curvature due to turbulent scales, the effect of a tumble on flame, and flame quenching. Secondly, as this work would require combustion prediction with high EGR levels, the combustion model needed to account for the residual (internal or external) mass fraction in the unburned gas mixture.

Premixed turbulent combustion requires that fuel and oxidizers are completely mixed before heat source is supplied. With the application of heat source, flame front propagates through the mixture with some velocity which depends on the pressure, temperature, air-fuel ratio, residual fraction, and turbulence flow field. This flame front divides the combustion chamber in two states, the unburned gases, and the burned gases, separated by the flame front where transition from one to another takes place. To model the combustion, various combustion models have been proposed. In this work, we will discuss on the model which are based on 'flamelet' assumption.

In the models based on flamelet approach, flame structure is composed of a distribution of laminar flame elements, whose thickness is negligibly small in comparison with the large eddies. Under flamelet assumption, chemistry is fast enough to have a very thin reaction zone, so one can consider that the flow consists of just two zones: the fresh gas zone and Burned zone. These two zones are separated by the elements of flames called flamelets. In most flamelet models, one also assumes that each flamelet behaves like a laminar flame. These elements retain their identity during flame development though they are strained in their own plane by turbulence. This phenomenon on one hand extends their surface area while on the

other hand, establishes the consumption rate of reactants by the flame elements. This increase in surface area due to flame stretching is counterbalanced by flame shortening mechanism where adjacent flame elements annihilate each other when comes in the vicinity by consuming intervening reactant. Under these considerations, the mean turbulent reaction rate for the reactants may be expressed as the product of flame surface density by the consumption rate of fuel per unit flame area (equation 1.1). The flamelet velocity, S_L and thickness δ_L are mean values, integrated along the flame front and is strongly dependent on pressure, temperature, equivalence ratio and EGR mass fraction. The conditional averaging technique is used to accurately calculate these quantities using species tracers and fresh gas enthalpy equations. While defining fresh gas state, EGR fraction in fresh gases is also included in the species calculations.

Under this assumption, the mean consumption rate of the fuel may be expressed as

$$\overline{\dot{\omega}} = w_L \Sigma \qquad (1.1)$$

where $\sum$ is the flame surface density (flame surface per unit volume) and w_L is the fuel laminar mass consumption rate per unit surface. For the laminar flamelet case, the mean consumption rate can be written as:

$$\overline{\dot{\omega}} = \rho_0 S_L^0 I_0 \Sigma \qquad (1.2)$$

where ρ_0 is the density of fresh gases, $S_L^0 I_0$ is the mean laminar burning velocity along the flame front, averaged over the flamelet surface. The quantities I_0 and Σ are interrelated because turbulent production of the flamelet interface area is influenced by laminar flame propagation and factor I_0 represents the effect of curvature and stretch on the flame surface. Bray et al [60], in his research has demonstrated that the stretch factor I_0 is a function of mean viscous dissipation ($\bar{\varepsilon}$) and standard deviation of the log-normal distribution of the dissipation (σ):

$$I_0 = I_0(\bar{\varepsilon}, \sigma) = I_0(K, \sigma) \qquad (1.3)$$

This expression was further modified to relate flame stretch as a function of Karlovitz number (K) and was determined from the experimental data from Abdel-Gayed et al. [61]. Further work on this was developed using DNS simulations [62], where it was shown that for cases with Le=1, local flamelets are not affected by stretch and were identical to an undisturbed laminar flame meaning $I_0 = 1$. This makes mean consumption rate ($\overline{\dot{\omega}}$) of the fuel proportional to laminar flame speed (S_L^0). To solve equation (1.2), formulation for $\sum$ is still needed.

The balance conservation equation for the turbulent flame surface density, $\sum$ is written as [63]

$$\frac{\partial \Sigma}{\partial t} + \frac{\partial u_i \Sigma}{\partial x_i} = \frac{\partial}{\partial x_i}\left(\frac{\mu}{S_c}\frac{\partial(\Sigma)}{\partial x_i}\right) + (S_1 + S_2 + S_3) - D \qquad (1.4)$$

where Sc is turbulent Schmidt number, μ is turbulent viscosity and ui are the mean flow velocity components. First term on the left-hand side corresponds to local rate of change. Second term in equation (1.4) corresponds to the transport by the mean flow whereas first term on right-hand side corresponds to turbulent diffusion. Next 3 terms are the source terms followed by the destruction term. Table 3.1 presents the different models proposed for source terms and destruction terms. In all the models mentioned in table 3.1, terms corresponding to convection and diffusion are modelled in the same way. S_1 terms corresponds to the flame stretch by convection whereas S_2 corresponds to flame stretch by turbulence. S_3 is the terms which has been proposed in Extended coherent flame model (ECFM) and corresponds to the thermal impact on flame curvature.

In this work, CPB model [64] is briefly discussed with different versions of CFM models [65]. It should be noted that in all models, source terms are proportional to the flame surface density $\sum$ whereas destruction terms are proportional to the square of flame surface density $\sum^2$ due to the fact that flames consumption occurs due to collision between flame surfaces. CPB proposes that the flame stretch due to turbulence is induced by Kolmogorov scales and is proportional to $\sqrt{\varepsilon/\nu}$. CFM2-b, an improvement over CFM1 and CFM2-a, approach is a physically based one where results from DNS simulations are incorporated in the sub-models. In this approach, the flame stretch due to turbulence is based on the 'Stretch efficiency function', which is determined by measurements and simulations of stretch rates. The Stretch efficiency sub-model is based on the fundamental concept that flame-vortex interaction. In the work of Duclos et al [138], various proposed models have been compared with one dimensional premixed turbulent combustion experiments [66]. It was shown that CFM2-b model performed best against experimental data. This model was able to correctly predict the flame stretch, bending of turbulent burning velocity and flame quenching in sufficiently intense turbulence.

Table 3.1: Flame surface density based models with the source and destruction terms used in equation 1.4. α, β, C_a are model constants. $\tilde{c}$ is the combustion progress variable based on the fuel mass fraction.Γ_k is the efficiency function of the ITNFS model.

Models	$S_1 = k_m\Sigma$	$S_2 = k_t\Sigma$	S_3	D	Assumption
CPB	$A_{ik}\frac{\partial\tilde{u}_k}{\partial x_i}\Sigma$	$\alpha C_a\sqrt{\varepsilon/\nu}\,\Sigma$		$\beta\bar{S}_l\frac{2+e^{-aR}}{3(1-\tilde{c})}\Sigma^2$ $R=\frac{1-\tilde{c}}{\Sigma\,\bar{S}_l\,k}$	Propagating surface theory
CFM1	$A_{ik}\frac{\partial\tilde{u}_k}{\partial x_i}\Sigma$	$\alpha\frac{\varepsilon}{k}\Sigma$		$\beta\frac{\bar{S}_l+C\sqrt{k}}{1-\tilde{c}}\Sigma^2$	Physical balance for $\sum$
CFM2-a	$A_{ik}\frac{\partial\tilde{u}_k}{\partial x_i}\Sigma$	$\alpha\Gamma_k\frac{\varepsilon}{k}\Sigma$		$\beta\frac{\bar{S}_l+C\sqrt{k}}{1-\tilde{c}}\Sigma^2$	
CFM2-b	$A_{ik}\frac{\partial\tilde{u}_k}{\partial x_i}\Sigma$	$\alpha\Gamma_k\frac{\varepsilon}{k}\Sigma$		$\beta\frac{\bar{S}_l+C\sqrt{k}}{\tilde{c}(1-\tilde{c})}\Sigma^2$	
ECFM	$A_{ik}\frac{\partial\tilde{u}_k}{\partial x_i}\Sigma$	$\alpha\Gamma_k\frac{\varepsilon}{k}\Sigma$	$\frac{2}{3}\bar{S}_l\frac{1-\tilde{c}}{\tilde{c}}\Sigma$	$\beta\bar{S}_l\frac{\Sigma^2}{1-\tilde{c}}$	

ECFM [59,67,68,69,70] is the extension of this approach in which:

- terms corresponding to flame stretch due to flame temperature has been added which was missing in previous versions of CFM2-b model.
- In addition to that, ECFM model has improvements in combustion progress description for stratified mixture condition. CFM2-b model is based on the assumption that the flame can be seen as an infinitely thin interface separating fresh and burned gases with no accumulation of mass within this interface. In this case, calculation of local burned mass fraction or combustion progress ($\tilde{c}$) is simplified by applied conservation of mass principle

$$\tilde{c} = 1 - \frac{\tilde{Y}_F^u}{\tilde{Y}_{TF}}$$

where, $\tilde{Y}_F^u$ is the unburned mass fraction of fuel and $\tilde{Y}_{TF}$ is the total mass fraction of fuel before the onset of combustion. In case of perfectly mixed charge, $\tilde{Y}_{TF}$ is constant in time and space in which case the calculation of $\tilde{c}$ is straightforward. However, in case of mixture stratification, $\tilde{Y}_{TF}$ varies in space and time. To solve this issue, fuel traces are used in ECFM model which makes it possible to be used in stratified charge cases such as with DI of NG.
- precise description of unburned composition (ERG) has been provided. This helps to achieve improvements in terms of local mixture composition.

These improvement in ECFM model makes it good combustion model to be used for this work.

Premixed turbulent combustion regime is defined in terms of lengthscale ($^{L_t}/_{\delta_L}$) and velocity scale ratios ($^{u'}/_{S_L}$) and was proposed by Bray [71], Barrere [72], Borghi [73], Peters [74], Williams [75], Abdel-Gayed and Bradley [76,77] and Poinsot et al [78]. When the turbulence integral scale and turbulent kinetic energy are known, these diagrams indicated whether the flow contains flamelets, pockets or distributed reaction zones. This information is essential for turbulent combustion behaviour. In classical premixed combustion theory, Klimov-Williams limit (Karlovitz number, Ka=1) [79,80] indicates the transition between flamelet regime and thickened-wrinkled flame regime. EGR dilution changes flame speed as well as flame thickness, which changes its turbulent combustion regime. Figure (3.1-3.3) are results obtained in this work and are presented here to explain the discussion. Figures are comparing lengthscale to velocityscale ratio for different combustion events such as, at 10 %, 50% and 90% mass burned fraction (MFB10, MFB50, MFB90 respectively) for different EGR conditions. Figures have lengthscale on X-axis while velocityscale on Y-axis and are in the log-log scale. Origin of the figures starts at (1,1) to remove the regions with Re =1, and $\frac{u'}{S_L} < 1$ (indicating wrinkled regime). At the start of combustion, flame takes time to develop due to physical and chemical delay. From mass burned fraction 0-10%, the flame speed gradually increases. MFB10 corresponds to the flame development where flame speed has still not reached its maximum value. After the initial delay, flame speed increases exponentially reaching its maximum value followed by flame quenching once flame reaches cylinder walls. In the case of EGR = 0%, during whole combustion duration, flame speed is dominant over the turnaround velocity of

Gibson scale (characteristic eddy size that interacts locally with flame front [79]). This can be seen in figure 3.1 as all 3 mass burned events are below Ka =1 line indicating that the flame front is continuous and the flamelet assumption is valid.

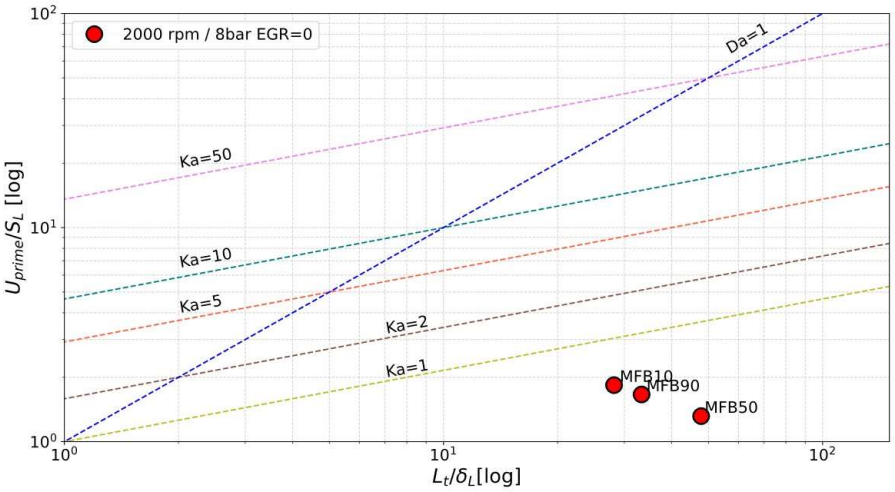

Figure 3.1: Premixed turbulent combustion regime: Spark advance (SA), mass burned fraction 10% (MFB10), mass burned fraction 50% (MFB50) and mass burned fraction 90% (MFB90) plotted for EGR=0%

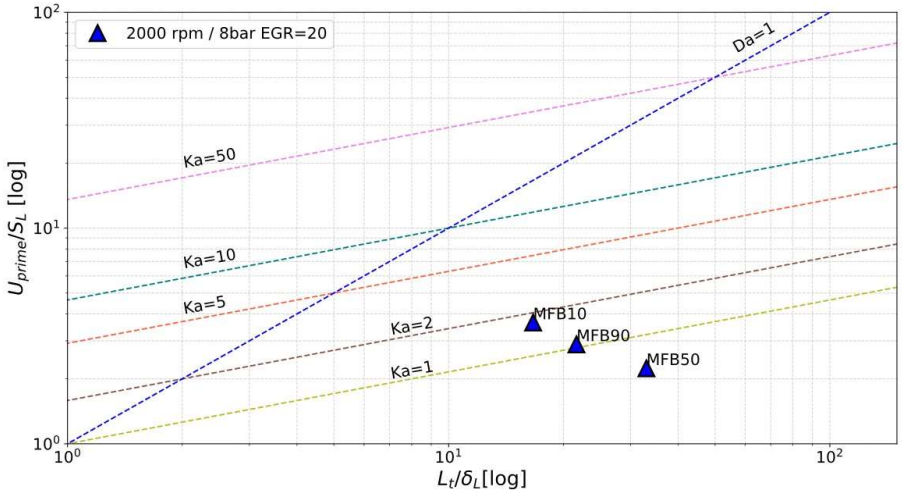

Figure 3.2: Premixed turbulent combustion regime: Spark advance (SA), mass burned fraction 10% (MFB10), mass burned fraction 50% (MFB50) and mass burned fraction 90% (MFB90) plotted for EGR=20%

With the addition of EGR = 20% (figure 3.2), the flame speed at the start of combustion is slower causing the eddies to enter preheat zone and increase scalar mixing and may create flame pockets. However, till combustion reaches MFB50 point, flame speed recovers and overcomes the turnover velocity of eddies. As combustion moves towards the end, flame speeds slow down again and may cause the flame to break at the end of combustion. In this case, most of the combustion takes place in the flamelet regime. Even though MFB10 and MFB90 combustion events are outside the flamelet regime, it was found (discussed in section 4) that the whole combustion event was stable with overall low cyclic variability (discussed in

section 3.6). Whereas in the case of EGR = 30%, the whole combustion is taking place at Ka>1(figure 3.3). This means that the flamelet assumption with this EGR fraction is invalid. This can create pockets of fresh charge surrounded by flames. High EGR % in fresh charge can also thermally quench these flames which would result in high variation in combustion.

From the figures, it can be noticed that the MFB50 event is more crucial for flame stability study and will be used to validate the flamelet assumption criteria in the rest of this work.

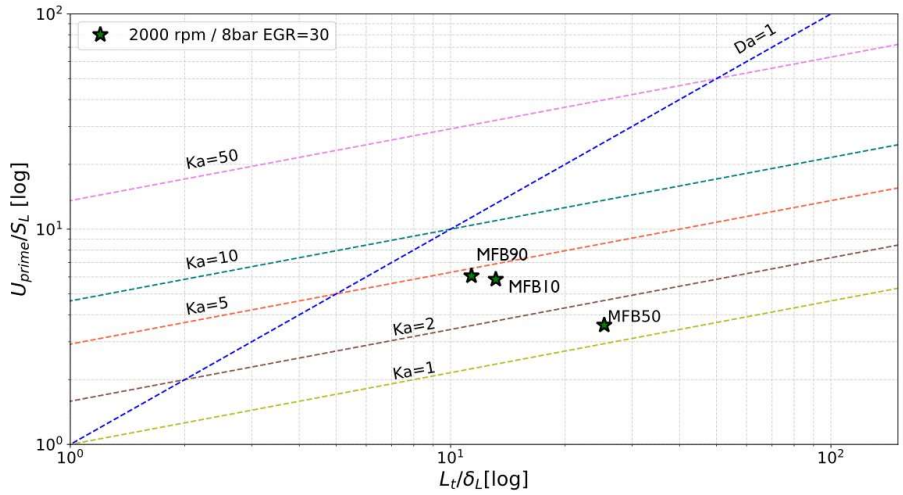

Figure 3.3: Premixed turbulent combustion regime: Spark advance (SA), mass burned fraction 10% (MFB10), mass burned fraction 50% (MFB50) and mass burned fraction 90% (MFB90) plotted for EGR=limit

ECFM model is highly sensitive to Laminar flame speeds (LFS) and is directly used in the transport equation of flame surface density (equation 1). Thus, it is important to use accurate LFS data for simulations. LFS can be calculated either using empirical or semi-empirical correlations for specific fuel or using a detailed kinetic mechanism. Empirical or semi-empirical functional relations were shown to work well with stoichiometric combustion. In this work, combustion in DI mode will be performed which can have high mixture heterogeneity which could limit the use of these functional relations. Also, various researchers have argued about the value of coefficients to be used in these functional relations during application [96]. For this reason, detailed kinetic mechanisms were used to calculate LFS in a wide range of pressure, temperature, EGR rates and equivalence ratio.

In this work, LFS was calculated using two mechanisms: GRI-Mech 3.0 [81] and ARAMCO 2.0 [82-88] using 0-D chemistry solver LOGEresearch [89]. For LFS validation, numerical LFS results were compared with available constant volume experiments at different pressures from the literature [90-95]. Figure 3.4 shows laminar flame speed (LFS) values with GRI-Mech 3.0 (in green) and ARAMCO 2.0 (in black). It can be noticed that at pressure =1 atm, both mechanisms are comparable with experiments. However, at Pressure = 5 atm, GRI-mech 3.0 over predicts LFS at higher equivalence ratios (above 1.2) and at p = 10 atm, GRI_mech over predicts in all equivalence range. ARAMCO 2.0 predicted LFS values accurately at all pressure ranges. ARAMCO 2.0 is a quite detailed kinetic mechanism that was needed to reduce

to make it more viable for CFD simulations. In this work, LFS values were simulated for a wide range of pressure (1 bar – 200 bar), temperature (300 K-1600K), equivalence ratio (0.3-2) and residual gas fractions (0-70%) with ARAMCO 2.0 kinetic mechanism and provided as input to combustion model.

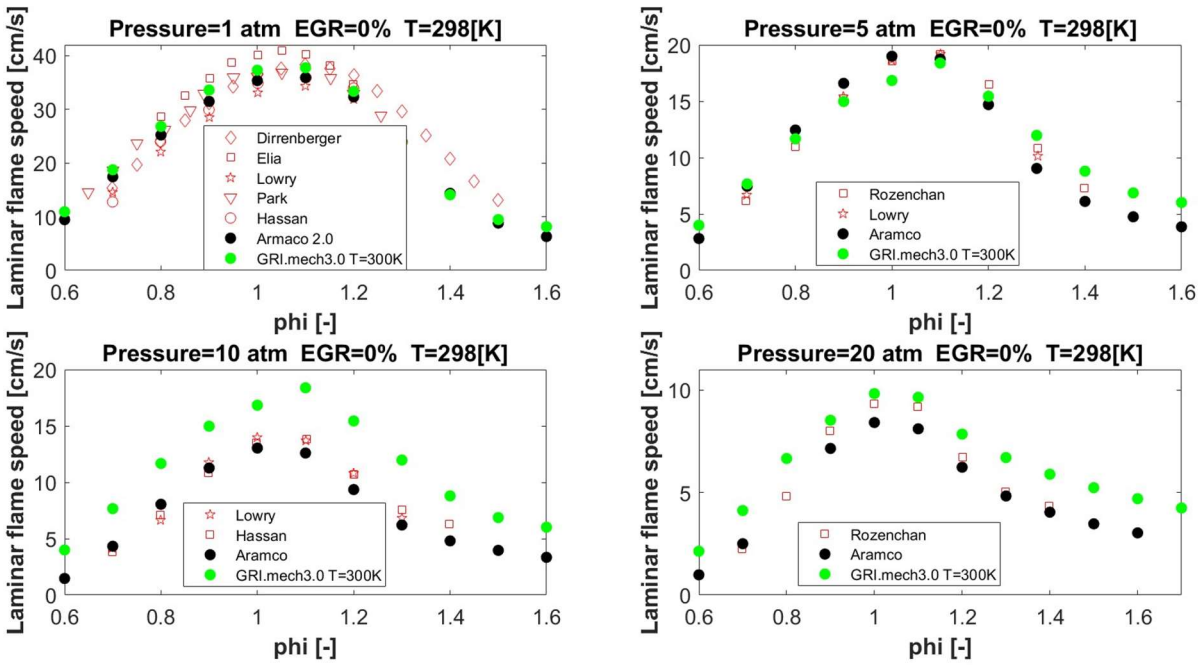

Figure 3.4: Laminar flame speeds calculations from GRI-Mech3.0 and ARAMCO 2.0 is compared with experiments at different pressure conditions.

Imposed stretch spark ignition model (ISSIM) has been used with the ECFM model to simulate spark in this work [97]. This model has been widely used for engine combustion simulation with LES [99,100] and RANS [101,102]. ECFM model has two calibration parameters: one is the coefficient for flame surface production due to turbulent stretch (ITNFS model constant) and the second is for initial flame wrinkling (C_{surf}). Calibration of both model constant is a necessary step to match the heat release rate (HRR) for a particular operating point [98,102].

3.2.2 ITNFS model

Basically, this model is applied to the flow containing flamelet reactions where main parameters for combustion due to turbulence is flame stretch and flame wrinkle. This mainly depends on the turbulent eddy scales and vortices through which the flame front is interacting. So, the variation of the surface due to turbulence is given by this model.

This model accounts for the production of the flame surface due to interaction of flame front with intermittent turbulent eddies and destruction due to high eddy velocity which leads to mutual annihilation of the flame surface. The eddies length scale smaller than laminar flame thickness will have a negligible effect on stretching even at a higher strain rate. The strain created due to turbulence not only affects the increase in the flame surface area but also determines the reactant consumption per unit of flame surface. There are three phases of vortex

interacting with the flame surface. The first one is an induction phase in which the vortex pair enters into the influence zone. The second phase is the vortex pair starts stretching the flame which increases the total reaction rate with time. The third phase is the flame fronts interact and merge, leading to flame surface consumption by mutual annihilation. A curve fitting method is used to calculate source term (S1 in equation 1.4) due to flame stretch which is given by the equation [103]

$$\frac{K_t}{\varepsilon/k} = ITNFS_{factor} * f\left(\frac{u'}{S_L}, \frac{L_t}{\delta_L}\right) \quad (1.5)$$

where,

ε = turbulent disspation,

k = turbulent kinetic energy

u' = turbulent RMS velocity

S_L = laminar flame speed

L_t = turbulent length scale

δ_L = laminar flame thickness as described in [58]

3.2.3 Effect of Initial flame wrinkling factor (C_{surf})

At spark ignition, the flame kernel produced will have wrinkling on the surface due to induced turbulence in the cylinder. C_{surf} value controls surface wrinkling in the kernel and has a dominating effect on initial kernel growth. $C_{surf} = 1$ is for laminar flames where the kernel will be spherical. $C_{surf} \geq 2$ increases wrinkling of the kernel surface, increasing its surface area. The increase in surface area will increase the combustion rate as well. Sai et al. investigated the effect of C_{surf} at various engine speeds and loads [98] and found that for lower engine speeds, low C_{surf} value is sufficient whereas, for high engine speeds, C_{surf} value should be increased to achieve appropriate combustion rates. Similar results were found in this work where model was validated with $C_{surf} = 2$ for all cases.

3.2.4 Effect of stretch factor constant (α)

As mentioned in equation 1.4, α is the constant which is multiplied to flame stretch (K_t), coming from equation (1.5). In this work, it was found that with increasing engine load at the same engine speed, α needed to be reduced. This behaviour can be due to limitation of combustion model to properly adapt for the effect of pressure on flame stretch. It is found in the literature that with an increase in pressure, the stretch rate decreases [25] which would decrease the flame surface production due to stretch as well. More work is needed to understand this phenomenon which is not performed in this work.

However, model was able to adapt for the change in mixture composition at the same working point (EGR at the same engine speed and load). This was sufficient to use this combustion model to achieve the objectives of this work. The stretch factor at different working points used in this work reported in Appendix I.

Literature has shown that the EFCM model for premixed combustion has worked well in IC engines [70,105,106]. It can be noted in the literature that with ECFM model, CO2 and NOx emission were predicted within certain accuracy. In the work of Duclos et al. on gasoline DI engine [105], the ECFM model well predicted the in-cylinder pressure traces. Also, the Nitrogen oxide emissions were well matched with experiments for 2 out of 3 cases. The case with the high error between experiments and computation was reported due to the underprediction of Imep.

3.3 Computational domain, numerical grid and boundary conditions

For current work, the same geometry in the computational domain was used as that in the experiments including ports, valves orientation and combustion chamber as can be seen in Figure 3.5. Pressure and temperature boundary conditions were taken from experiments. The length of the intake and exhaust runners were decided based on the location of pressure transducers used during the experiments. A build-in mesh generation algorithm of CONVERGE was used to generate orthogonal, block-structured mesh during runtime based on user-specified grid parameters. The uniform base mesh of 2mm was applied in the computational domain. The specific areas were further refined as per the requirement and required accuracy. In-cylinder volume had a mesh of 1 mm in the majority of the section. The locations with high shear velocity, such as valves and corresponding seats were refined to achieve the mesh size of 0.5mm, which has been widely discussed in the [44,107,108] and accepted to be sufficient for non-reacting flows.

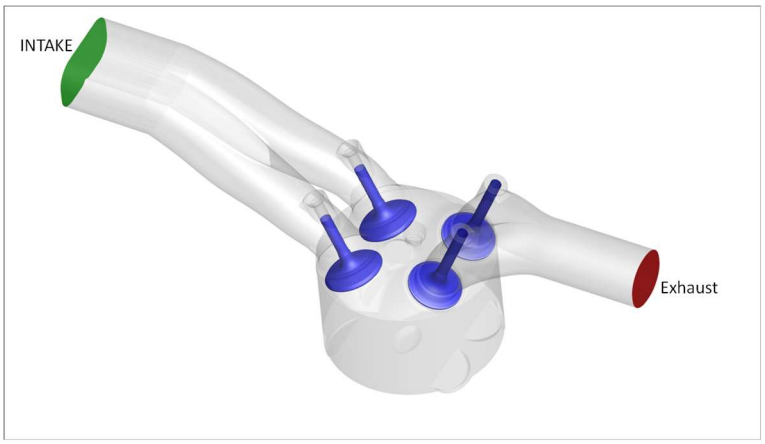

Figure 3.5: Geometry of 'new engine design'

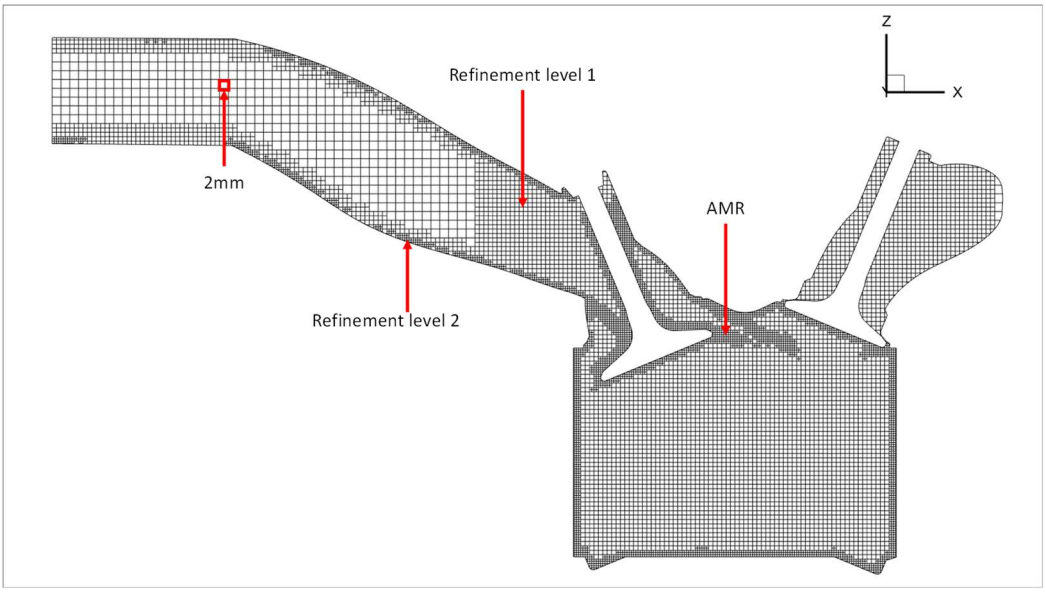

Figure 3.6: Mesh size and AMR used during simulations

CONVERGE CFD allows to refine the mesh based on vector or scalar gradients wherever they reach a user-defined limit. This option is helpful to use highly refined grids to simulate complex high-velocity flows or flame propagation. Automatic Mesh Refinement (AMR) reduces the computational costs while increasing the computational accuracy of the case. In this work, AMR was used for velocity and temperature gradients to further refine the localised areas of the computational domain with the cell size of 0.5mm as described in figure 3.6. In the figure, the intake runner has a mesh size of 2mm in the free stream region (as indicated). The energy equations at the wall boundaries are solved using the law-of-wall boundary condition. For high Reynolds number turbulent flows, the viscous sub-layer of the flow may not be possible to resolve accurately [109]. The Launder and Spalding wall model [110] is used to fit a logarithmic curve of the turbulent boundary layer. This wall model works well when coupled with the RNG k-ε model. The transition from refined cells ~0.5mm of the boundary wall to the free stream grid of ~2mm was realized by using a multi-layer transition zone. Mesh was also refined by cell size of 0.5mm at the flame front location during combustion.

RANS equations are integrated with the Redlich-Kwong equation of state in the present work. This choice is because, at high pressure and low-temperature conditions, gas behaviour deviates from ideal law, as it was shown in the work of Kaario et al [111]. This work has compared ideal gas law behaviour at high load points with the Redlich-Kwong model and Peng-Robinson model. It has been shown that the Redlich-Kwong model is in good agreement with experimental data in predicting the compression phase. In the present work, since the engine has a high compression ratio (CR=13.4) and simulations will be performed at full load working point, the use of a real gas model is justified.

An experimental campaign was performed (as discussed in chapter 2) on the same engine and its data has been used to set the boundary conditions. Inlet/exhaust pressure and temperature

conditions were applied at the same location where measurements were acquired. Wall boundary conditions were taken from an experimentally calibrated model in GT-power. Geometry was divided into three regions namely Cylinder, intake and exhaust and the initialization conditions were set using the GT-power model. The start of simulations was set at 180deg CA representing exhaust stroke. Such strategy, rather than starting the simulation from intake stroke, is crucial to calculate the correct residual exhaust gases inside the cylinder which will be mixed with intake air during the first cycle itself.

The temperature boundary conditions for all geometries in the cylinder are treated with the law of wall function along with the Angelberger heat transfer model [112]. The thickness of the viscous sublayer depends on engine speeds and compression ratio which can reach a value of around 10μm in case of high load condition in high compression ratio engines [113]. To solve the boundary layer, algebraic wall function models are employed to describe both momentum and thermal boundary layer. The assumed distribution of velocity, temperature and turbulent kinetic energy and dissipation rate are represented by algebraic formulae [110], is applied to cells lying in the logarithmic region of the boundary layer where molecular and turbulence effects are of comparable magnitude.

Convective fluxes in the finite volume discretized RANS conservation equations are approximated by a second-order accurate differencing scheme. A flux blending scheme that ensures physically realistic results with a high-resolution scheme is employed. This scheme uses a flux limiter near the discontinuities in the computational domain, that switches locally to first-order spatial discretization to avoid spurious oscillations in the solution while the rest of the domain is still solved with second-order spatial discretization. The time advancement is handled by an implicit scheme that is based on the unconditionally stable implicit first-order Euler scheme and explicit deferred correctors which leads to a formal accuracy between first and second order. The pressure velocity coupling is solved by using a modified pressure implicit with splitting of operator (PISO) method. The Rhie-chow algorithm is used to solve the colocation of pressure and velocity at the cell center by interpolating velocity to the cell face [114]. This scheme introduces some error, although smaller than but similar to the staggered approach (which is also used in CFD solvers).

3.4 Mesh dependency with premixed combustion cases

The mesh mentioned above was chosen after careful study of different mesh sizes and their impact on the result. Table 3.1 shows the mesh details at different engine locations.

With Mesh1, the trapped mass inside the cylinder is lower compared to the other 2 meshes. Mesh2 and Mesh3 have comparable trapped mass with 2mg difference. This difference can be because of under resolved mesh on the intake and exhaust valves which can influence the gas exchange process.

Table 3.2: Mesh settings for mesh dependency test

	Embedding type	Mesh 1	Mesh 2	Mesh 3
Base Mesh[mm]	Fixed	8	4	4
Minimum cell size in cylinder	Fixed	2	1	0.5
	AMR	1	0.5	0.25
Intake valve	AMR	1	0.5	0.5
Exhaust valve	AMR	1	0.5	0.5
Spark location	Fixed	0.25	0.125	0.125
Maximum number of cells (averaged in 1 cycle)		200,000	1,200,000	3,500,000
Trapped mass [mg]		413	418	420
Computation time (core hours/cycle)		216	960	2496

Figure 3.7 shows the average in-cylinder pressure and average heat release with three mesh settings. It can be noticed that till 685 deg CA (spark timing), all three cases have similar in-cylinder pressure. However, the difference in heat release is clearly visible. Mesh 2 and Mesh 3 has similar total heat release. Figure 3.8 shows the combustion duration parameters for three cases. Mesh2 and Mesh 3 has similar combustion duration in all 3 phases whereas Mesh1 has underpredicted theta0-10 and theta10-50 by 1deg CA each.

Mesh 2 and Mesh 3 have similar performance in terms of combustion performance and trapped mass. However, Mesh 3 is 2.6 times more computationally expensive compared to Mesh2 (Table 3.2). As during this work, many simulations with multiple cycles will be run, Mesh 2 was decided to be the optimal choice.

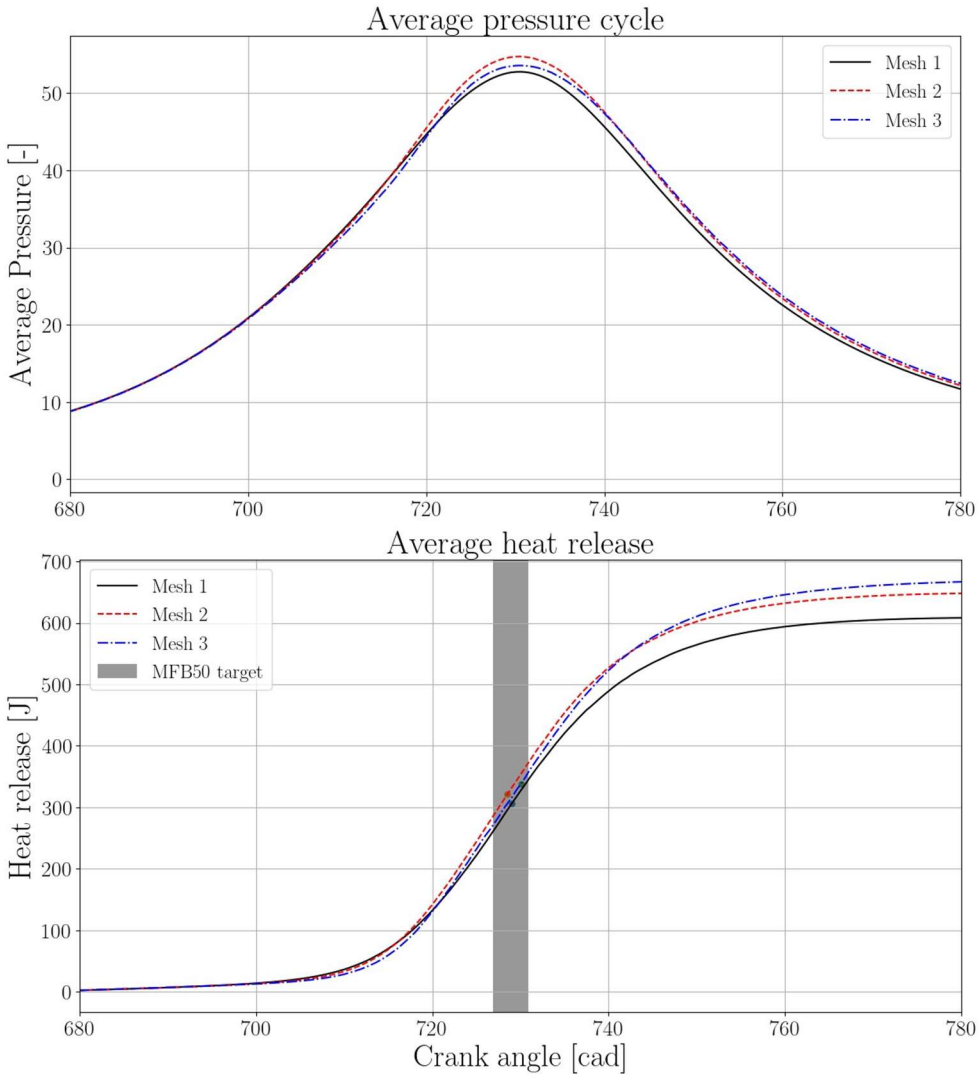

Figure 3.7: Average in-cylinder pressure and heat release for different mesh settings

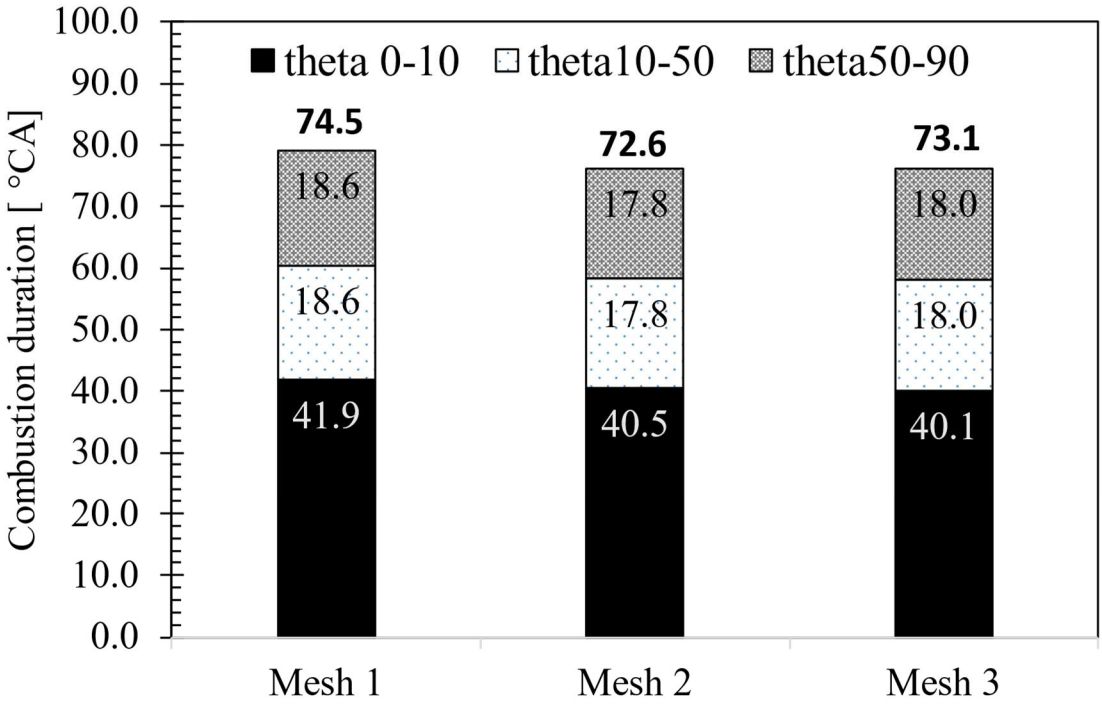

Figure 3.8: Combustion duration with different mesh settings

3.5 Mesh with DI simulations

To correctly capture the gas-dynamic structure of an under-expended jet which originates due to an expansion fan at the nozzle exit, fine mesh at the nozzle throat is important. It was shown in the work of Baratta et al. that to correctly capture the shock-cell elements in which gas is alternatively expanded and compressed, a cell resolution of 40-cells at nozzle height would be required [115]. Resolution of 10-cells can also give acceptable results in terms of jet penetration with compromise on Mach reflection. However, these simulations were performed with a first-order upwind scheme. It was mentioned that with a second-order scheme, more accurate results can be captured with lower mesh resolution at high computational costs.

Scarcelli et al. performed simulations on direct gaseous jet injection in hydrogen engines. It was reported that grid resolution strongly influences the jet penetration while it has almost no effect on fuel dispersion as it is underpredicted with every resolution [116]. It was also reported that resolution in the near-nozzle region is the dominating factor for jet penetration and the rest of the work was performed with 8 cells across the nozzle throat which showed good accuracy for mixture formation.

In the present work, multi-cycle reactive simulations were performed with direct injection with the objective to define mixture breakdown at high engine speeds. For this, a compromise between mesh resolution and computational time was realised. Mesh was divided into two zones: one near the nozzle throat and area around it and the second, cylinder area. A mesh size of 0.25mm at the nozzle throat area was used as shown in figure 3.9 (black lines). Further,

downstream, to accurately describe the jet shape, adaptive mesh refinement (AMR) was used. The results of injector jet shape were qualitatively compared with the literature mentioned above and were found to be acceptable.

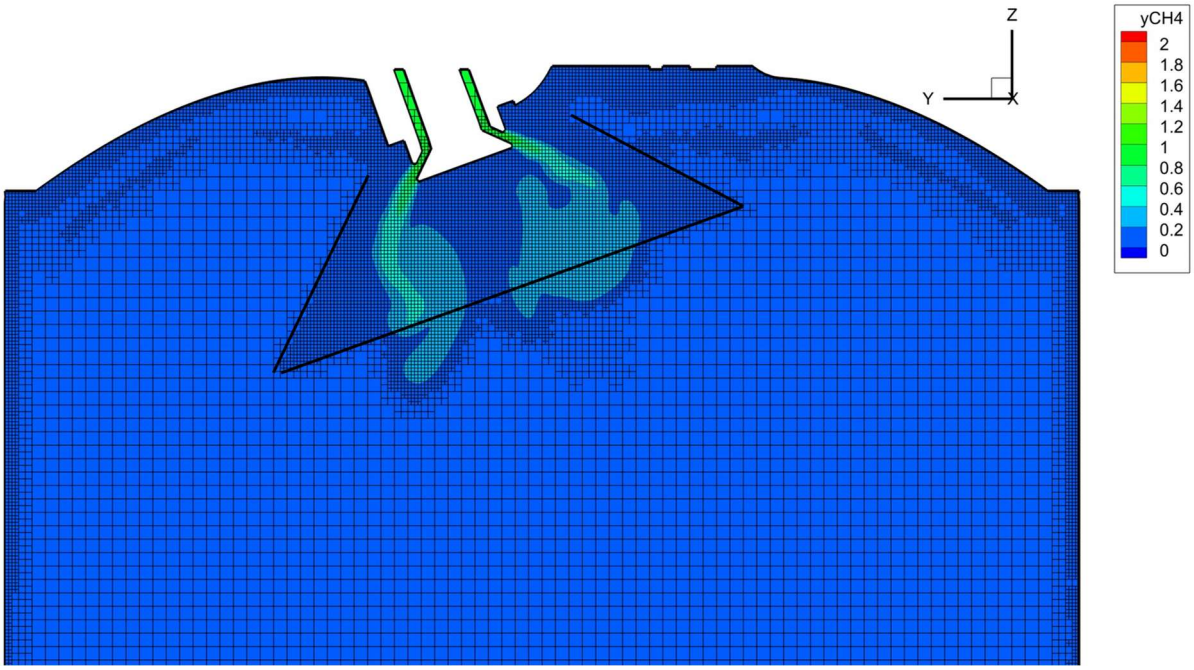

Figure 3.9: Injector mesh

3.6 Numerical model quality assessment for cyclic variation in URANS

Cyclic variability with URANS is an open question among scientific community. Cyclic variation analysis has been long performed with Large-eddy simulations (LES) as it captures the large scale (sub-grid scale) turbulent flows while effectively modelling the small-scale eddies. However, LES is computationally expensive. RANS turbulence model, as an alternative to LES, is expected to capture an ensemble-averaged result. RANS models the time-varying smaller eddies and replaces their mixing effect with enhanced viscosity. In IC engines, large-scale time-varying structures changes during each cycle and may not be small enough to be damped out by the RANS turbulent viscosity. Richards et al [117] have demonstrated that reducing the numerical viscosity can help in preserving these time-varying large scales. The study concluded that though Reynolds stress tensors are closed by adding viscosity which effectively damps the smaller time-varying scales from the solution but may not remove all time-varying scales. These large-scale eddies lead to cycle-to-cycle variation in the RANS model which is similar to, but not as predictive as the LES turbulence approach.

Another study by Scarcelli et al [118] from Argonne National Laboratory and Convergent science Inc. demonstrated that the cyclic variations while using RANS are not a numerical artifact or the effect of change in the computational grid. A several step detailed analyses was

performed on the impact of multi-cycle RANS on cyclic variability. In the first step, simulations were performed on GDI with diluted combustion with RANS and the reason for cyclic variability were discussed. In the next step, it was demonstrated that AMR is not the cause of cyclic variability. The work was also extended to describe the effect of numerical viscosity on the trade-off between accuracy and repeatability. The study concluded that cyclic variations in flow velocity and equivalence ratio at spark location effectively leads to cyclic variation and can be captured by the RANS model to an extent. The same conclusions were also drawn in other literature [119].

Similar evidence was found in this study as well. Figure 3.10 shows multi-cycle in-cylinder pressure with URANS simulation for the case with 20% EGR. The numerical pressure trace features large cyclic fluctuations in 7 consecutive cycles with no convergence pattern. The first cycle was discarded from averaging analysis as it was affected by the initialization and boundary conditions.

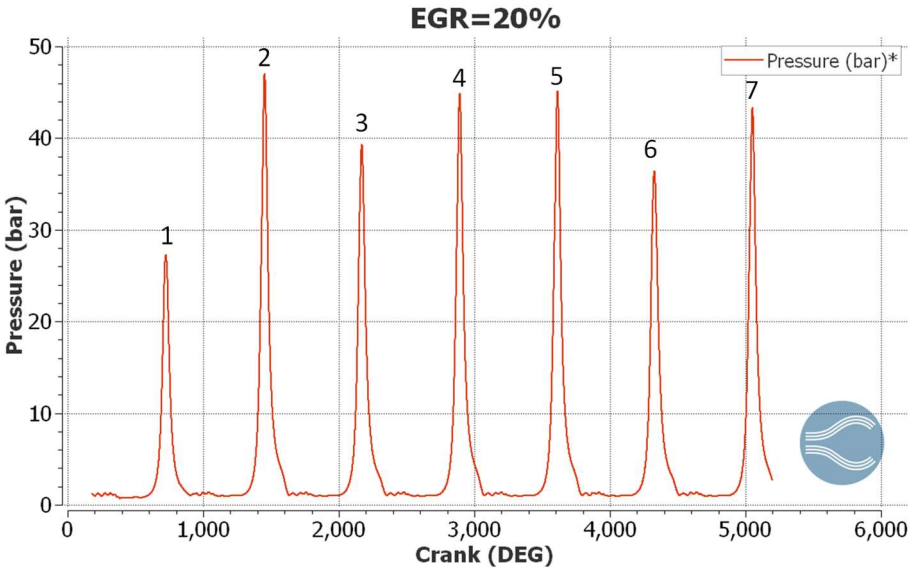

Figure 3.10: Cycle-to-cycle variation with URANS. In-cylinder pressure shown for 7 consecutive cycles

Figure 3.11 compares the average experimental cycle with an errorbar representing the extent of peak pressure of multiple experimental cycles. It can be observed that the average simulation cycle traces well with the average experimental cycle whereas cyclic numerical pressures peaks are within the experimental cyclic variation. This cyclic variation in the numerical simulation is generated due to different initial conditions at the start of each cycle and are not damped out even after a large number of cycles.

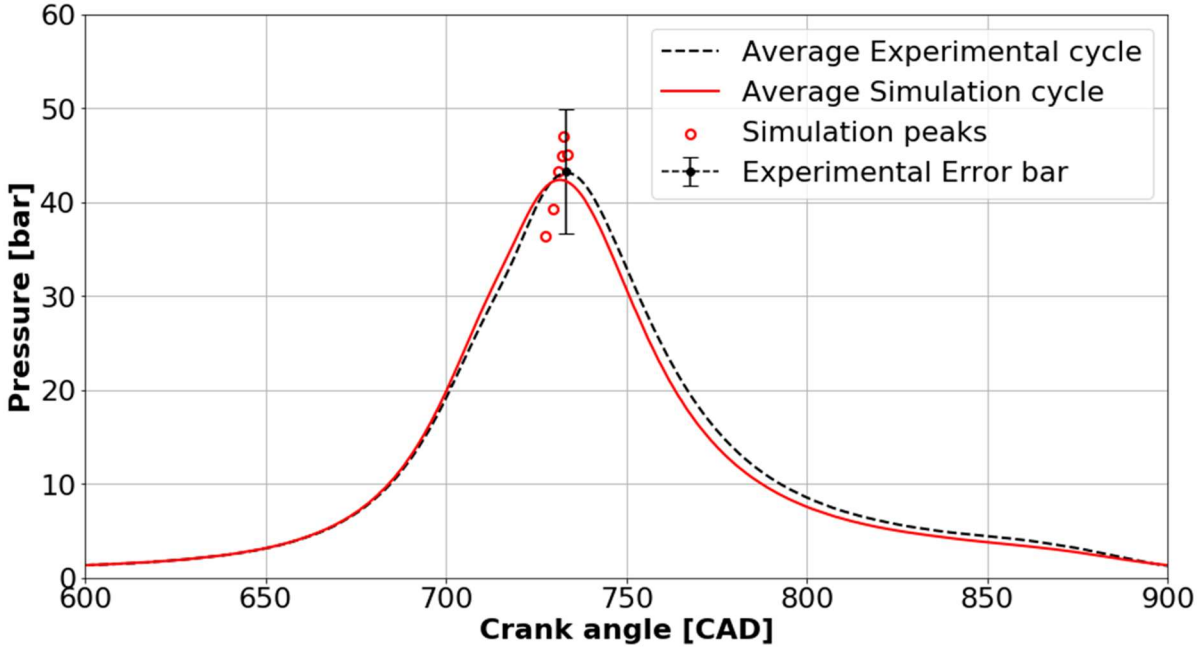

Figure 3.11: Average In-cylinder pressure comparison between experiments and numerical prediction. Experimental error bar represents variation in experimental peak pressure while Simulation peak represents cyclic numerical peak pressures

Figure 3.12 shows the cycle resolved total trapped mass calculations in the cylinder at spark event. As mentioned earlier the results of the first cycle are affected by initial and boundary conditions, this can be clearly observed in the figure as the difference in mass of the first cycle and the rest of the cycles. For this reason, the first cycle was removed from the analysis. After the first cycle, the mass has converged to a stable value and thus does not cause the cycle-to-cycle variation.

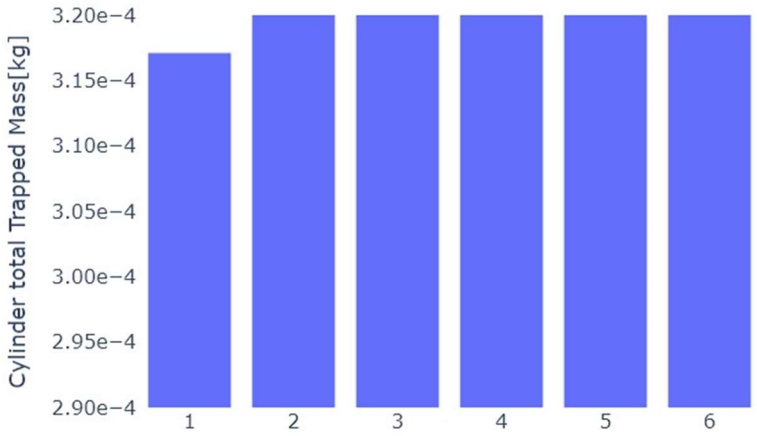

Figure 3.12: Average In-cylinder trapped mass

Figure 3.13 shows the cyclic comparison of the Global Tumble index and flow velocity magnitude near the spark plug region. Global tumble index was calculated as an average in the computational domain at spark event while flow velocity magnitude was calculated in a spherical region centred in the spark plug gap with a radius of 3mm. While comparing figure 3.13 and figure 3.10, a clear indication of fluctuation of pressure can be linked to the Global tumble and flow velocity near the spark. Figure 3.14 shows the velocity magnitude in the spark plug plane at the spark timing. It can be further observed that the velocity at the spark plug location has a variation from one cycle to another. This affects the flame kernel development and thus affects the flame propagation which in turn will affect combustion speed.

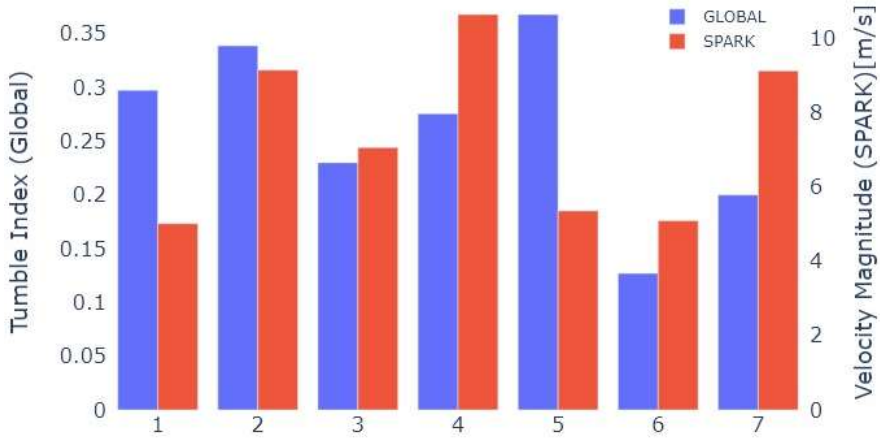

Figure 3.13: Global Tumble number (Primary axis) and local velocity magnitude (spark) for 7 consecutive cycles

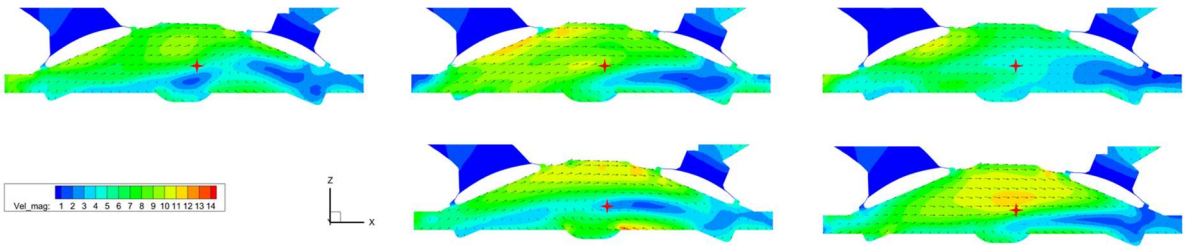

Figure 3.14: Velocity magnitude at spark timing for different cycles

In this section, an effort has been made to analyse the cause of cyclic variation observed during this work. Evidence has shown that the cause of cyclic variation is due to changed velocity field at the spark location during ignition event. This variation in velocity field would affect the kernel development and this also impact the combustion speed. Cyclic change in velocity field is attributed to the lower numerical viscosity achieved through the numerical code used. Further analysis is needed to ascertain this phenomenon using different numerical codes. This was not performed in this work and thus remains an open point of discussion.

3.7 Nomenclature

3.7.1 Flame development angle and combustion duration

Figure 3.15 shows a mass fraction burned (MFB) curve as a function of engine crank angle, used to describe the stages of the combustion event.

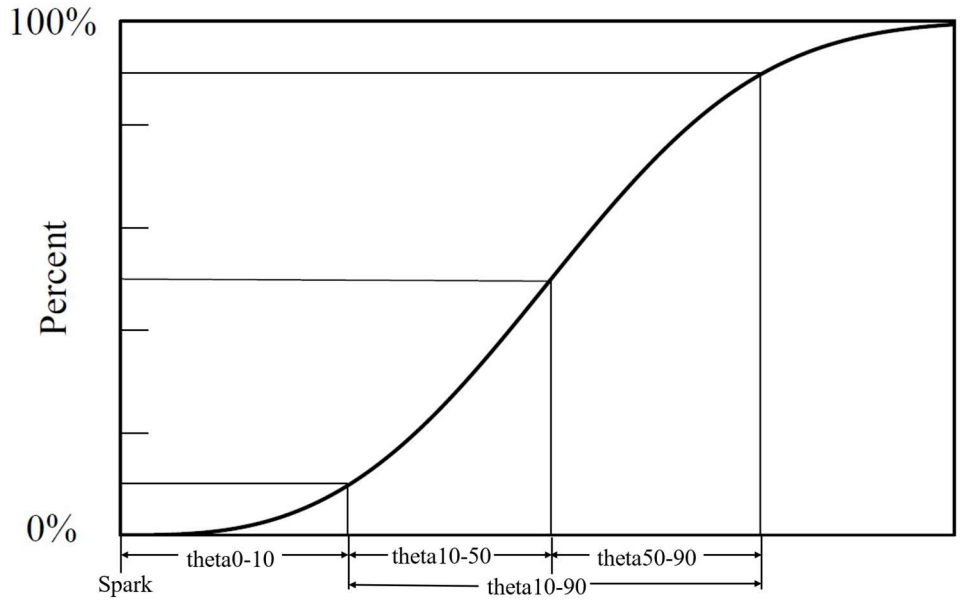

Figure 3.15: Mass Fraction Burned (MFB) curve

theta0-10 is known as the flame development angle, is defined as the crank angle interval from the time of ignition until 10% of cylinder mass has burned [17]. theta10-90 is known as the combustion duration and is the crank internal from 10% to 90% MFB.

3.7.2 Coefficient of Variation (CoV)

The Coefficient of variation is a non-dimensional parameter that gives the index of homogeneity inside the computational domain. It is calculated by comparing the cellwise standard deviation of the mass of fuel over the average fuel mass in the domain. CoV of zero means that all fuel in the domain has cellwise deviation meaning fuel is homogeneously distributed.

$$CoV = \frac{\sqrt{\frac{1}{N}\sum_i^N \left([CH4]_i - \frac{1}{N}\sum_i^N [CH4]_i\right)^2}}{\frac{1}{N}\sum_i^N [CH4]_i}$$

3.7.3 Flammable Fraction (FF)

The flammable fraction indicates the ratio between the quality of fuel included in a flammable mixture to the total mass of fuel present inside the chamber. It is calculated by summing up all the mass of fuel in the computational domain whose relative air-fuel ratio is in the range of 0.7-1.7 (flammability limit of methane). FF = 1 means that all fuel is within flammable range inside the computational domain.

$$FF = \frac{Mass\ of\ fuel\ in\ flammable\ mixture}{Total\ mass\ of\ fuel}$$

3.7.4 Fuel conversion efficiency (η_f)

The fuel conversion efficiency is defined as the ratio between the useful mechanical work produced by the engine and the theoretical energy content of the fuel mass.

$$\eta_f = \frac{W_c}{m_f \,.\, Q_{LHV}}$$

The indicated work per cycle W_c [J] is a function of in-cylinder pressure (P) and volume (V):

$$W_c = \int PdV$$

$m_f = trapped\ mass\ of\ fuel\ inside\ the\ cylinder\ per\ cycle$

$Q_{LHV} = Lower\ heating\ value\ of\ fuel\ (for\ methane\ 50MJ/kg)$

3.7.5 Length scale and velocity scale ratio

For turbulent premixed flames, the chemical time scale, τ_c, maybe estimated as the ratio of flame thickness $\delta_L$and the propagation speed $S_L$of the laminar flame. Estimation of turbulent time from turbulent integral scale $L_t$and turbulent fluctuations u' (u_{Prime}) gives the formulation for Damköhler number (Da) as:

$$Da = \frac{\tau_t}{\tau_c} = \frac{L_T}{u'}\frac{S_L}{\delta_L}$$

where a velocity scale ratio ($^{u'}/_{S_L}$) and lengthscale ($^{L_t}/_{\delta_L}$) are evidenced.

Chapter 4

EGR dilution limits

In this chapter, the results obtained with the numerical model on EGR tolerance limits with the 'new engine design' are presented. First, the numerical model (discussed in section 3) has been validated against the experimental data available. Then EGR tolerance of 'new engine design' will be compared with a conventional 'Low turbulence engine'. The latter differ from each other for the different levels of in-cylinder turbulence. Finally, EGR tolerance limits at part load and high loads are discussed along with their impact on performance and efficiency.

4.1 Model validation

The numerical model described in section 3 was validated against experimental data with no EGR conditions at 2000 rpm/ 3bar and /8bar imep. The Numerical model calibration constants used for flame stretch (α) and surface wrinkling (C_{surf}) (section 3.2) were calibrated at each working point without EGR. For simulations with EGR =20%, the calibration parameters were kept constant, and the results were compared with experiments. This strategy indicated that the developed numerical model is able to capture the effects of EGR on the mixture velocity and can thus be used for EGR tolerance prediction. Figure 4.1-4.2 shows the comparison between experimental average and numerical average pressures and Rate of heat release (ROHR) [J/deg)] at 2000 rpm and low load (3bar) and medium load (8bar) Imep respectively at EGR = 0%. Figures indicate experimental peak pressure variation (maximum cylinder pressure ± σ) labelled as 'Experimental Error bar' (black dotted line with circles at ends) and peak pressures of numerical simulation, labelled as 'Simulation peak pressure' (red circles). It can be noted that the numerical model is able to capture the compression phase quite well in both cases compared to experiments. At 3 bar Imep, an optimum value of combustion constants (α and C_{surf}) was difficult to calibrate. Still, the average pressure and ROHR is well within acceptable limits. However, at 2000 rpm / 8bar Imep, optimum combustion calibration was found, and average numerical results are in good agreement with experiments. Along with in-cylinder pressure, the heat release rate is used for validation. The heat release rate is derived by the applying single-zone heat release model by Brunt [120]. Both experimental and numerical heat release are calculated from in-cylinder pressure using the same technique. Both average numerical pressure and cyclic pressure peak are well within the experimental variability range. As 2000 rpm / 8bar Imep with no EGR had more accurate combustion phasing than 3 bar Imep. So, this point was chosen to validate the numerical model with EGR.

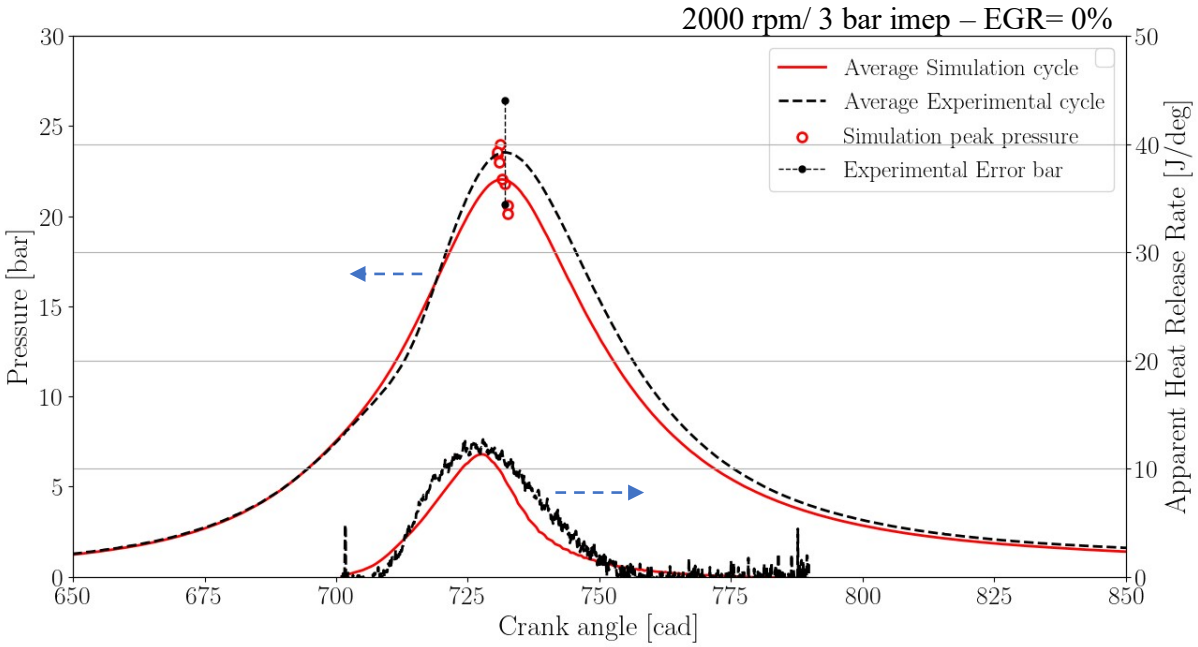

Figure 4.1: 2000 rpm / 3 bar Imep -Model validation

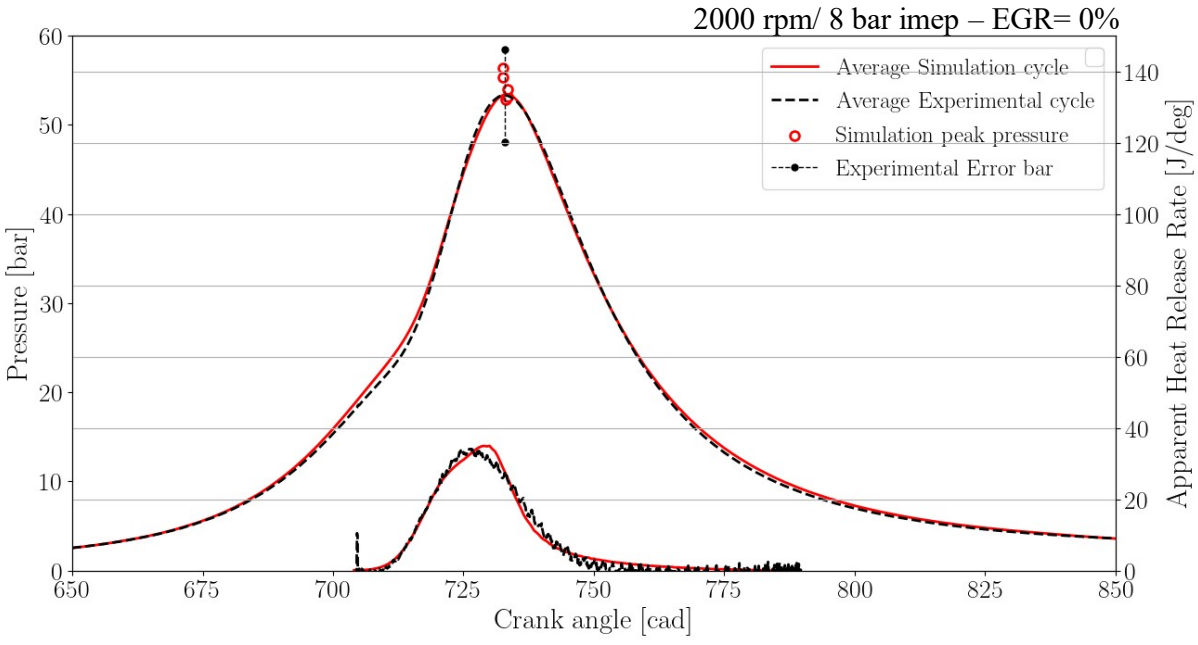

Figure 4.2: 2000 rpm / 8 bar Imep – Model validation

Figure 4.3 shows model validation with 20% EGR at 2000 rpm / 8bar Imep. In this case as well, the numerical model has predicted in-cylinder pressure and ROHR well within the experimental limits. It should be noted that combustion constant with and without EGR was kept constant for a particular working point. Considering the same flame stretch and surface wrinkling at a certain load, combustion speed would be highly dependent on the laminar flame speed of the fresh gas composition. The ability of the model to correctly capture in-cylinder pressure and ROHR indicates that tabulated LFS data is able to correctly capture the laminar flame speed trends vs. EGR.

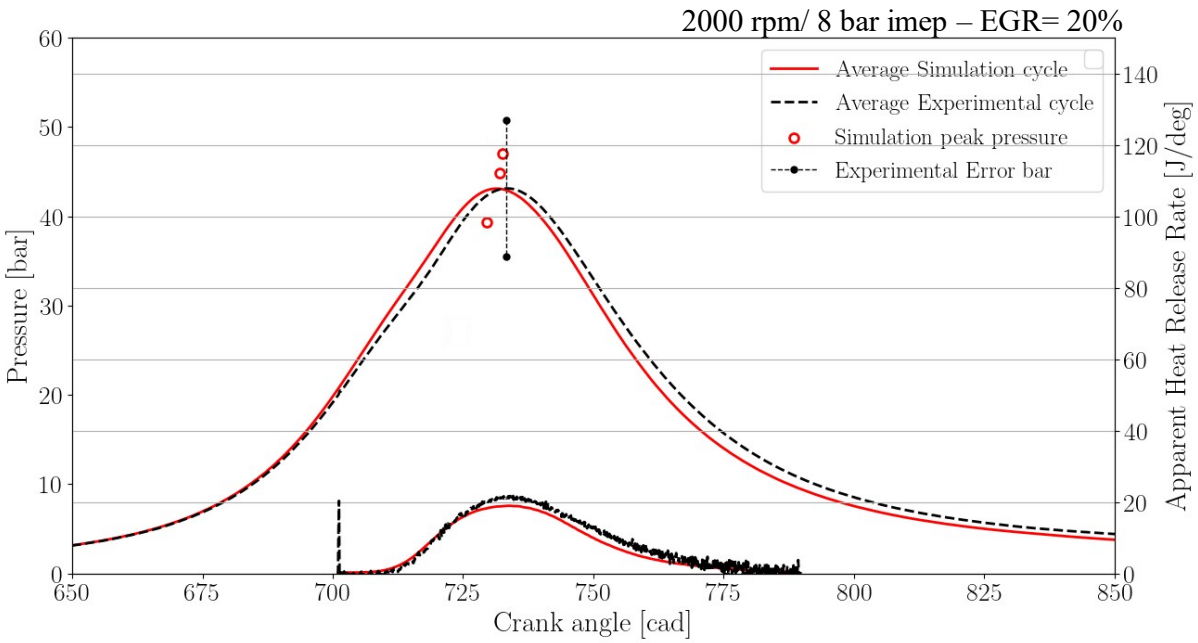

Figure 4.3: 2000 rpm / 8 bar Imep – Model validation with EGR

Figure 4.4 shows the combustion parameters comparison between experiments and numerical prediction for 2000 rpm / 8bar Imep. The figure reports two distinct phases of combustion, flame development angle (theta0-10) and rapid burning angle (theta10-50 and theta50-90). For EGR = 0%, numerical theta0-10 is -0.1 deg CA compared to experiments indicating a correct calibration of the surface wrinkling constant (C_{surf}). For EGR = 20%, numerical theta0-10 is -0.7 deg CA compared to experiments whereas theta10-90 is -0.1 deg CA. The difference in flame development angle indicates that ignition delay with EGR in the numerical model is shorter compared to experiments. However, the overall combustion duration in both cases is within 1 deg CA and was considered to be sufficiently accurate. It can also be noticed that 20% increase in EGR, has increased overall combustion duration by ≈54%.

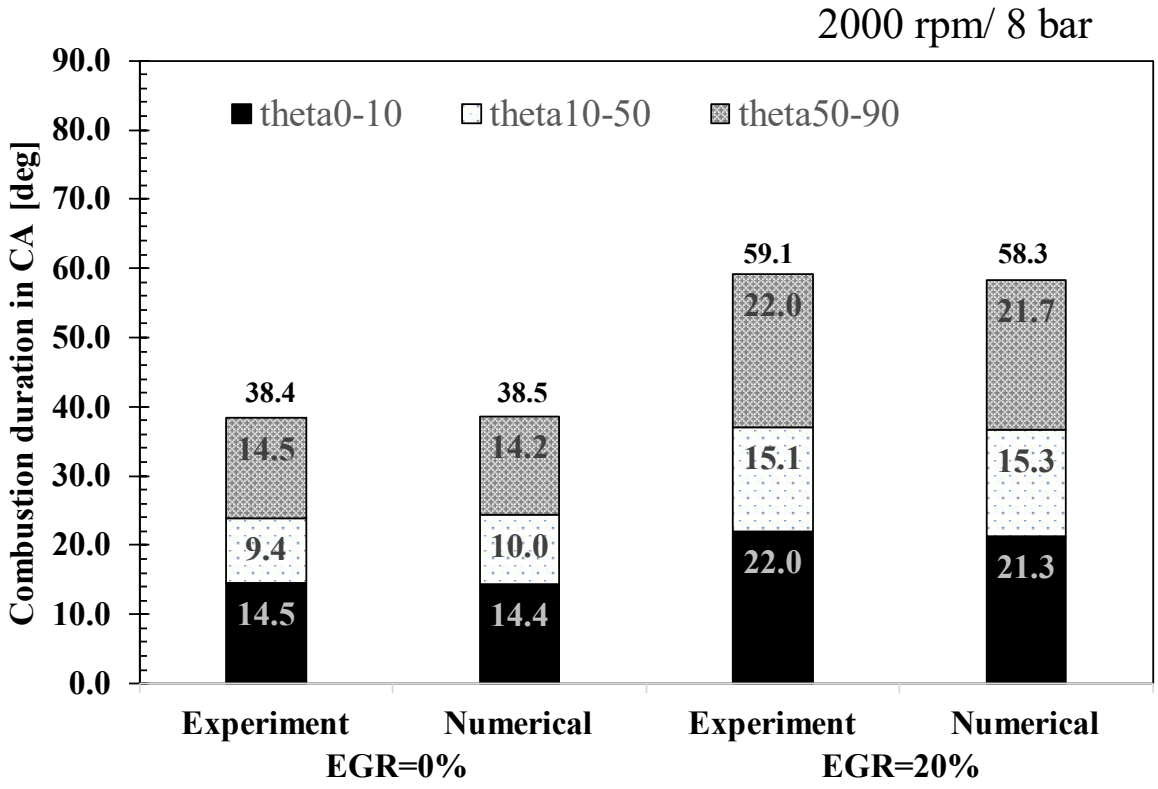

Figure 4.4: 2000 rpm / 8 bar Imep – Combustion duration comparison between experiments and numerical

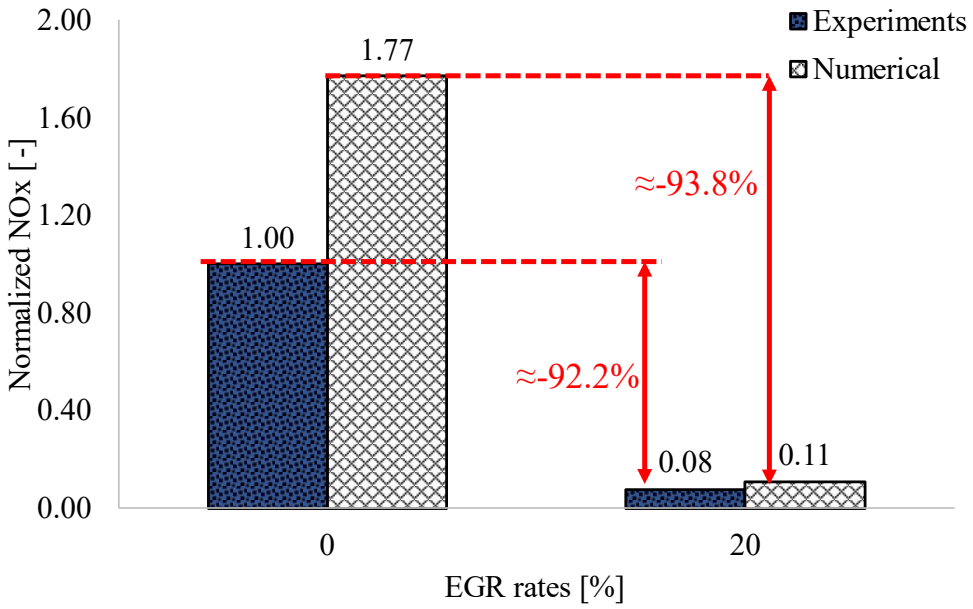

Figure 4.5: Normalized NOx emissions comparison between numerical and experiments at 2000 rpm / 8 bar Imep

Figure 4.5 shows NOx values of EGR rates 0% and 20% for experiments and simulations, normalized with experimental EGR=0%. The numerical model has overpredicted the NOx value in terms of absolute values. However, if we focus on the trends, it can be observed that NOx reduction with EGR addition has been correctly predicted. EGR rate of 20% has reduced NOx by around 92% compared to no EGR case.

In the next section, the validated numerical model will be used to compare the impact of high turbulence design on EGR tolerance.

4.2 Impact of EGR tolerance with new engine design

In this section, EGR dilution results of 'new engine design' with high tumble ratio is compared with 'low turbulence engine'. The design of the new engine was optimized to increase turbulence in the combustion chamber without compromising permeability and has been discussed in section 2.1. Rouleau et al [47] performed this study on the engine test bench and showed that the new design was able to achieve a higher tumble number but with 10% reduction in permeability coefficient. Keeping this in perspective, results are compared for 3000 rpm / 8bar imep with EGR = 0% and at the EGR limit specific to both engine designs.

Figure 4.6-4.7 shows the global turbulent kinetic energy (TKE) and Tumble number comparison between Low turbulence engine and new engine design at constant intake pressure of 0.75bar respectively. It can be noticed that the 'new engine design' has a higher global TKE of about 15% at the TDC location compared to the 'Low turbulence engine'. The maximum tumble number during the intake stroke of 'new engine design' is 1.9 compared to 1.4 of 'low turbulence engine'. For each case, peak tumble occurs close to the point of maximum valve lift on the intake stroke.

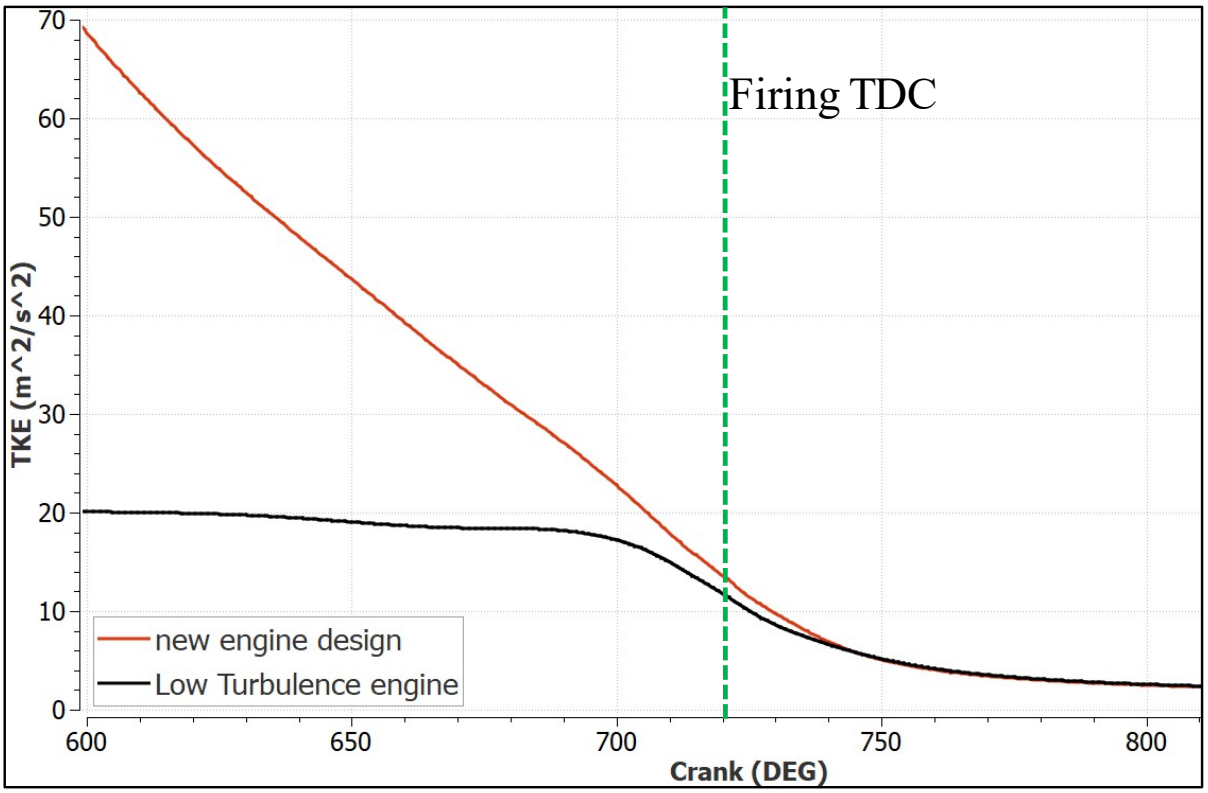

Figure 4.6: Global TKE comparison between two engine designs

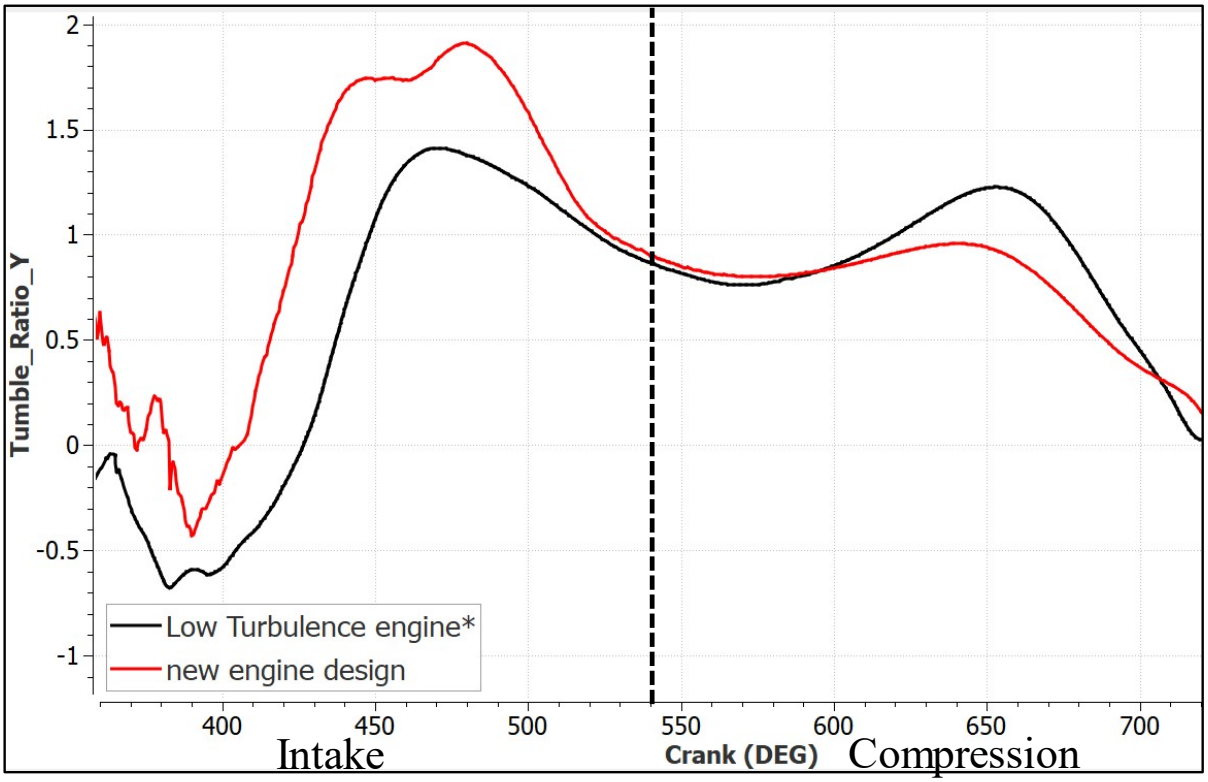

Figure 4.7: Tumble number along Y-axis comparison between two engine designs

Figure 4.8 shows the combustion duration of both engine designs with EGR = 0% at 3000 rpm / 8 bar imep. It can be noted that for both engine design, the overall combustion duration is comparable. This phenomenon can be explained using Figure 4.9 that shows the global TKE comparison between two engine designs with black squares indicating spark timing. Due to high TKE in 'new engine design' at spark timing, initial flame development is faster which is evident from the comparison of theta0-10. TKE of new design remains dominant till 10 degCA aTDC which indicate faster combustion during this time and is evident from the theta10-50 phase. However, in the last phase of combustion (theta50-90), TKE values in both cases have converged to similar values. In the 'Low turbulence engine', intake pressure is 0.92 bar compared to the new design (0.7 bar). Combining the effect of high volumetric efficiency (0.83 compared to 0.68 in new design) and higher intake pressure, trapped mass in the cylinder is higher for 'Low turbulence engine'. In the theta50-90 phase of combustion, better mixture conditions overcome the advantages achieved from high turbulence and resulted in faster burn rates in the last phase.

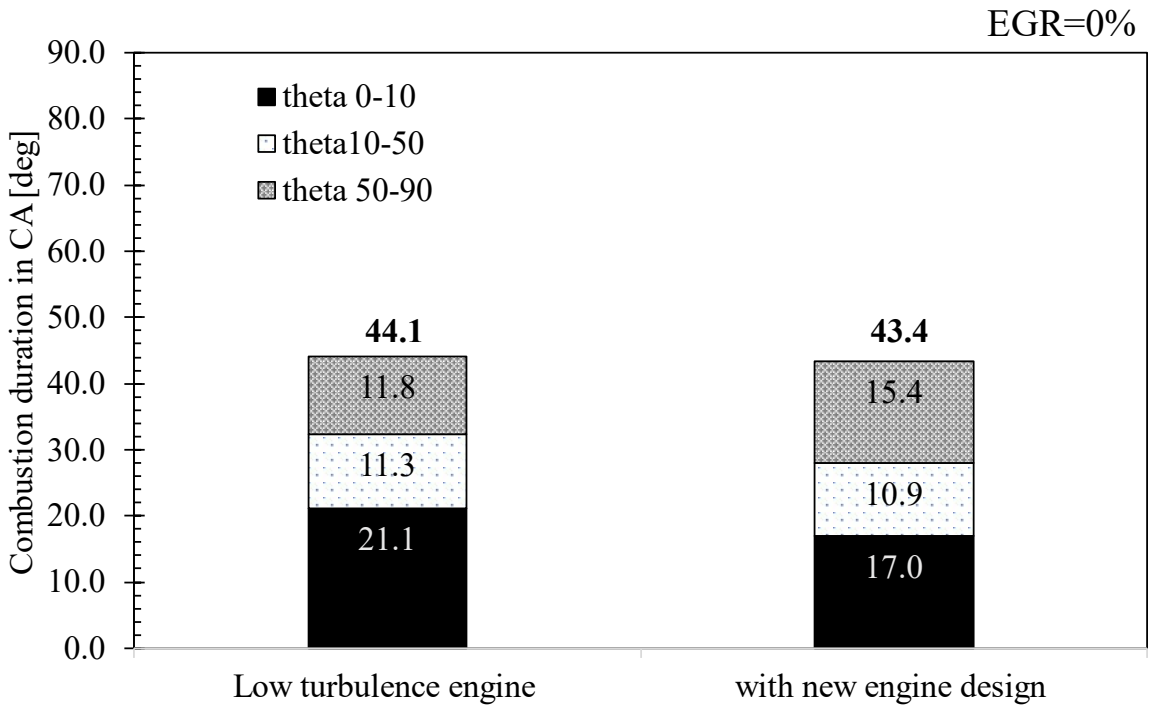

Figure 4.8: 3000 rpm / 8bar Imep – combustion duration

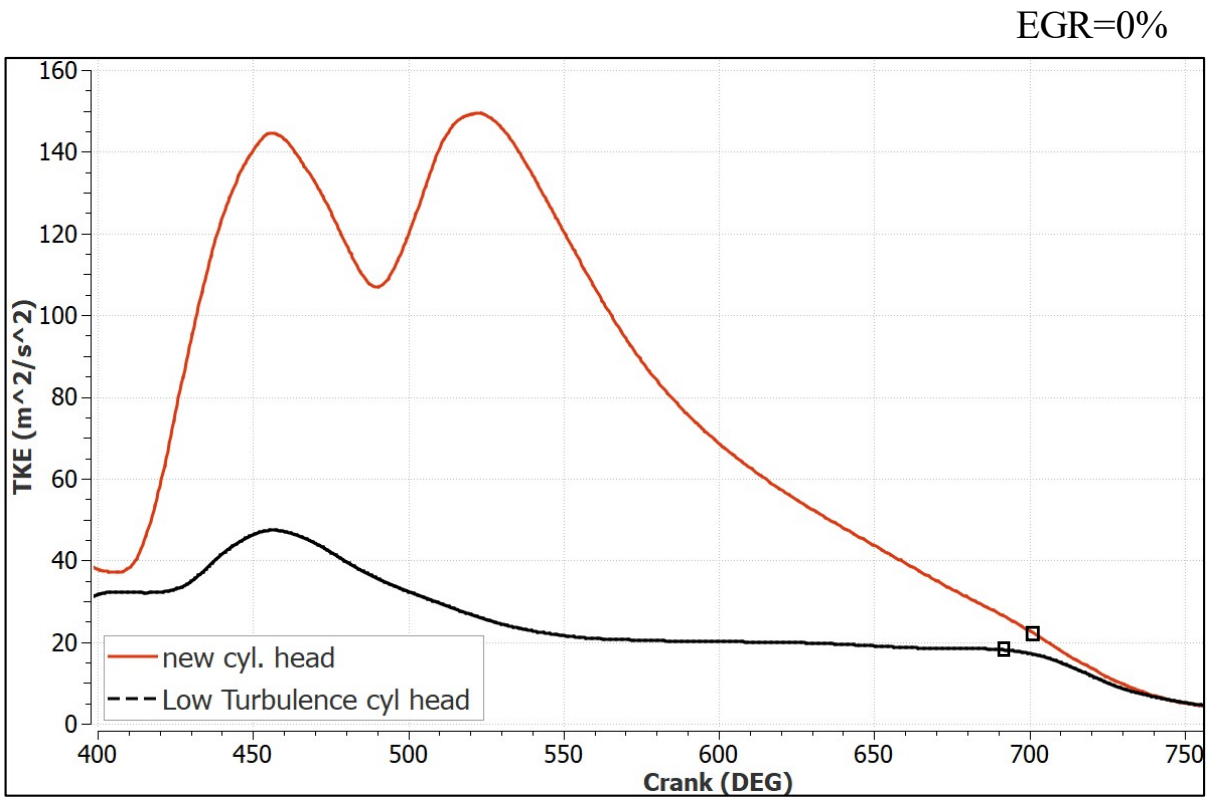

Figure 4.9: Global TKE comparison between new engine design and Low turbulence engine

Simulations were extended to predict EGR dilution tolerance by introducing low-pressure EGR (LP-EGR) in both engine designs. To accommodate high EGR rates, intake pressure was increased. This represents the de-throttling required with EGR. Figure 4.10 shows the combustion duration comparison whereas figure 4.11 shows the global TKE comparison between two engine designs at EGR limits. For 'Low turbulence engine', the EGR limit was found to be around 20% whereas, for 'new engine design', EGR tolerance was around 30%. The new design has shown to tolerate high EGR rates due to higher in-cylinder turbulence (figure 4.11). In the new design, the combination of high flame surface area provided by turbulence and slower laminar flame speeds with 30% EGR has led to a similar combustion duration compared to 'Low turbulence engine' with 20% EGR. Similar results were observed in the work of Zheng et al. where the increase of tumble from 1.12 to 1.6 improved EGR tolerance by 5 % at 1500 rpm and 2.2bar Imep [121].

In the next section, EGR dilution limits at part load and full load at 2000 rpm for 'new engine design' will be discussed in detail.

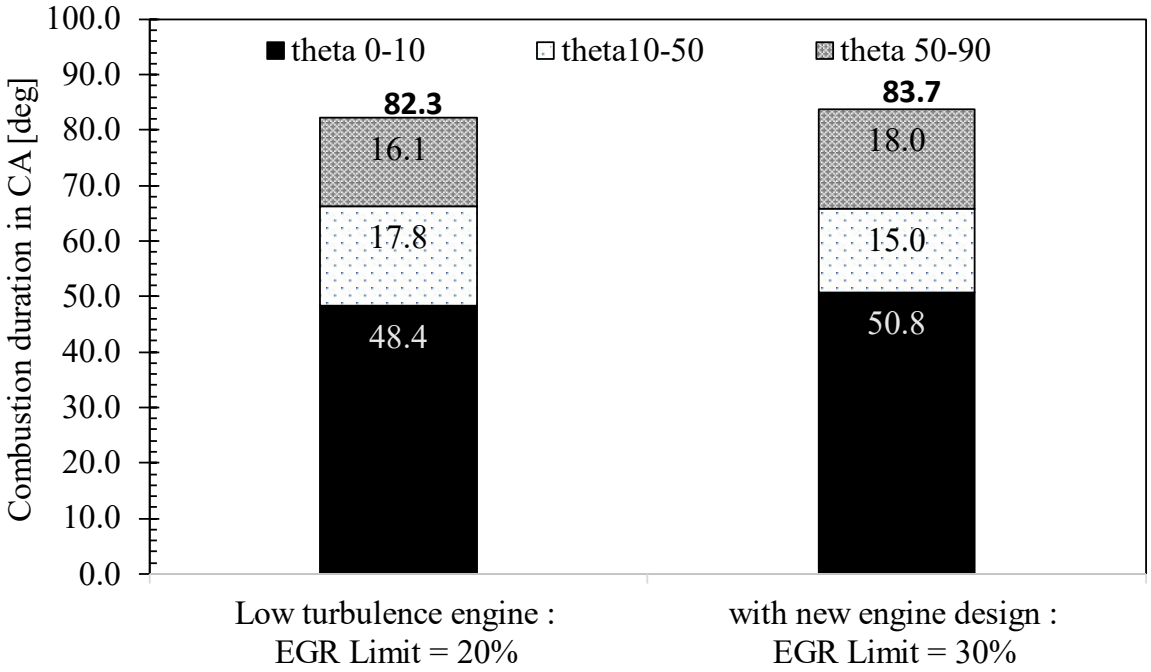

Figure 4.10: Combustion duration comparison at EGR limits between two engine designs

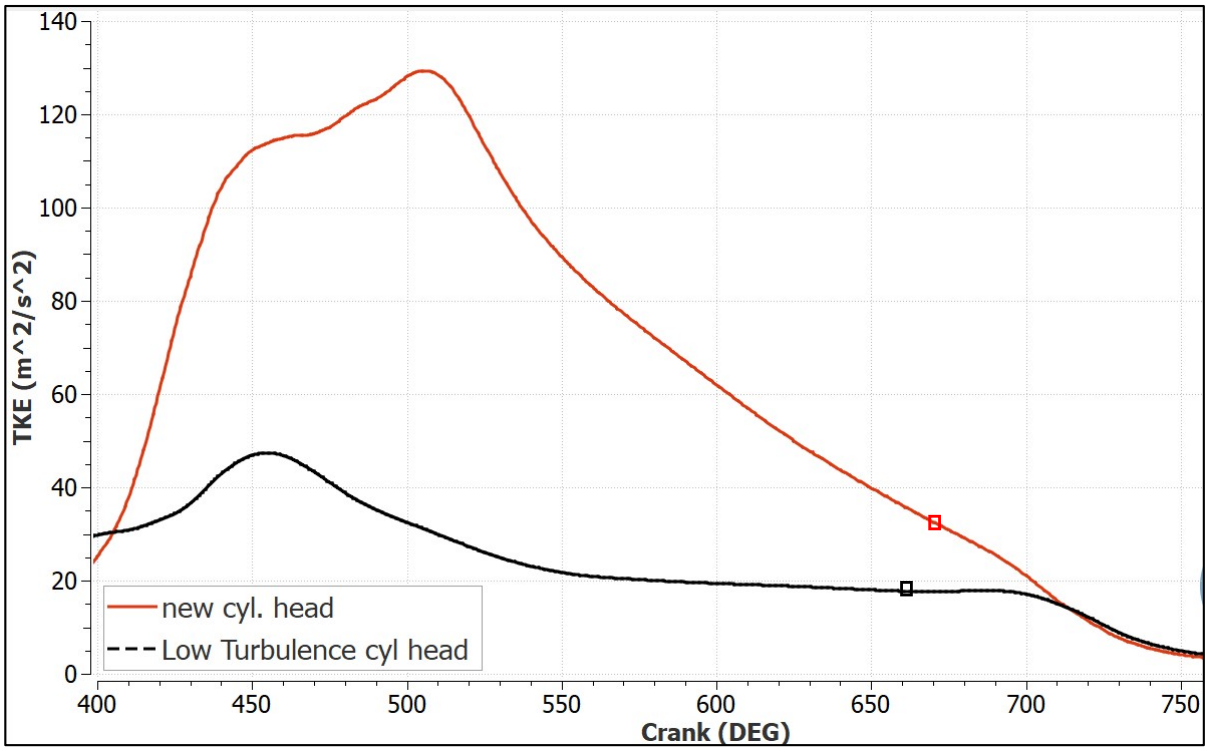

Figure 4.11: Global TKE comparison at EGR limits between two engine designs

4.3 EGR dilution tolerance at part loads

In this section, EGR tolerance limits for new engine design at 2000 rpm and part load condition are presented. For that purpose, a series of EGR sweeps were set up and carried out using numerical model validated in the last section. To study the impact of EGR addition on engine tolerance limits, parameters such as combustion phasing, Imep, fuel mass inside the combustion chamber were kept constant. Combustion timings target was selected to keep the MFB50 location fixed at 728±2deg CA. The homogeneous mixture was inducted into the combustion chamber in order to get rid of combustion behaviour on mixture variability. To simulate the conditions of ideally cooled EGR, intake temperatures were kept constant for various EGR rates.

An experimentally calibrated GT-power model was used to derive boundary conditions for EGR sweeps cases. With increasing EGR, air inlet pressure was calibrated to achieve target Imep using the GT-power optimization tool. The obtained boundary conditions were used as input for 3D simulations for EGR sweep cases. Spark timing was optimized to reach target MFB50. Since the impact of EGR on combustion speed was not known a priori, simulations were performed to get optimum spark timing [123,124]. 3D-CFD model was run for three consecutive cycles with an initial spark advance value. Average MFB50 between second and third cycles were checked with target MFB50 (728±2deg CA). In case of agreement within the tolerance limits, the simulation was continued until 7 cycles to decrease the effect of numerical cyclic dispersion on the results. Otherwise, the case was stopped, and described procedure was followed with a new spark advance value.

Figure 4.12 shows trapped fuel mass at 2000 rpm and part loads (3 bar and 8 bar Imep) as a function of EGR. In all cases, the mass of methane trapped in the cylinder is within ± 1 % except for the case of 35% EGR at 8 bar Imep. Figure 4.13 shows spark advance and turbulent intensity at spark advance for part loads as a function of EGR. Spark timing was advanced as EGR rates were increased to accommodate slower combustions with EGR rates. As a function of advance in spark timing, turbulent intensity (u') value at spark timing was also increased. The increase in u' at spark advance with increased EGR will help in the flame development phase.

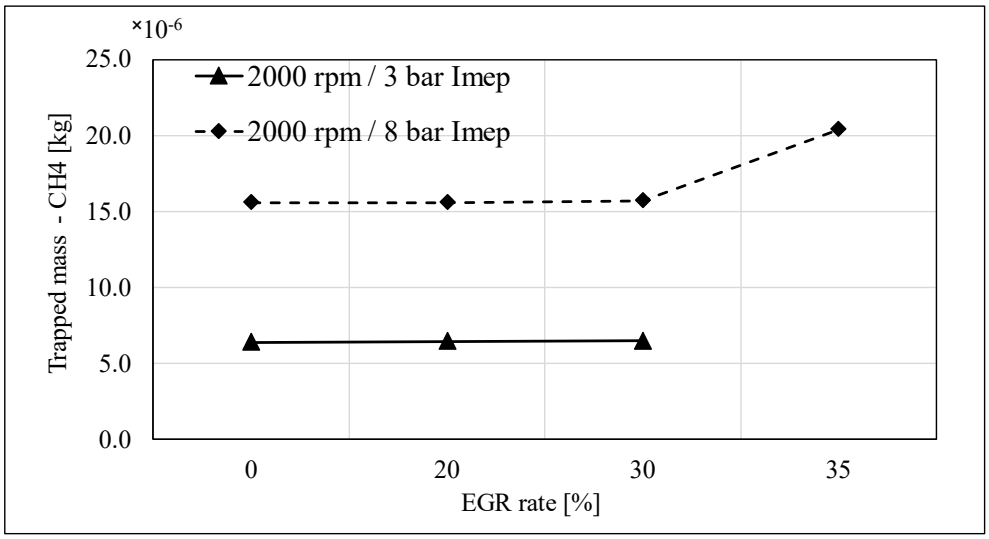

Figure 4.12: Trapped mass at part loads as a function of EGR

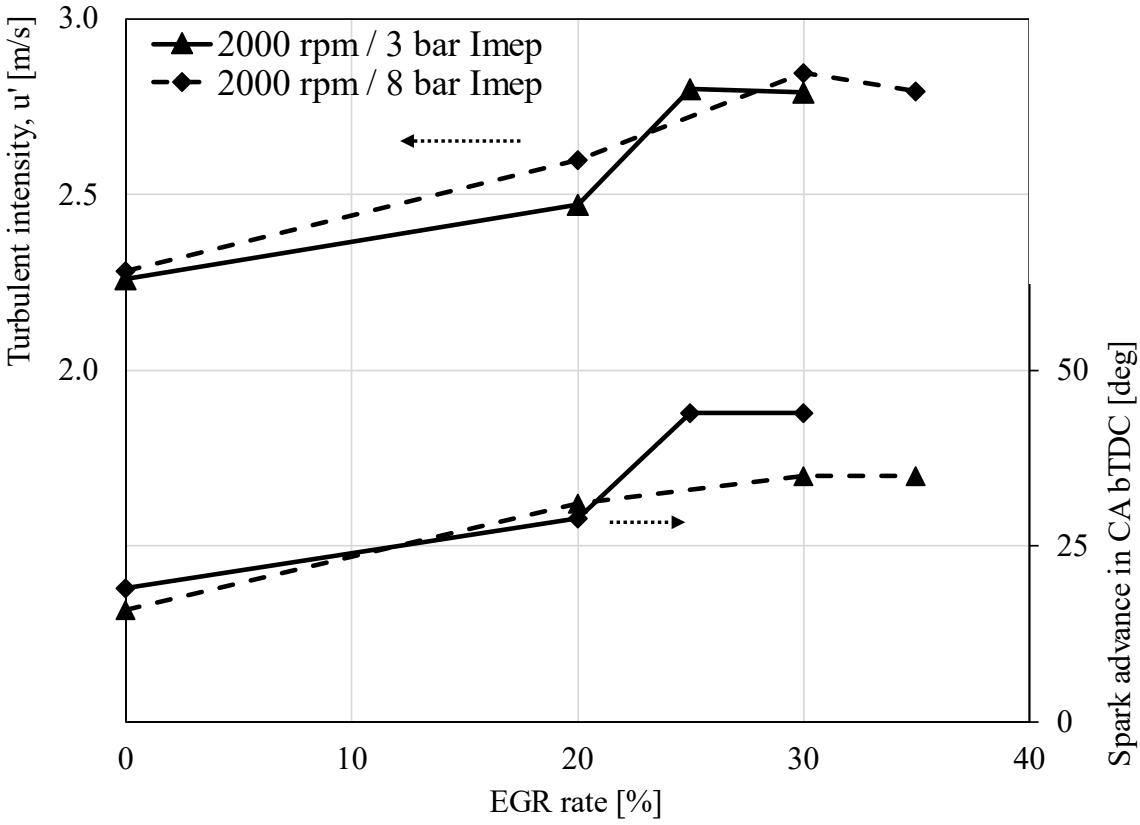

Figure 4.13: Spark advance and Turbulent intensity (u') for part load cases as a function of EGR

Figure 4.14 shows the average in-cylinder pressure and heat release rate for different EGR rates at 3 bar Imep. The higher intake pressure with increasing EGR rates had resulted in higher trapped mass inside the cylinder and a thus higher-pressure during compression. It can be noticed from the figure that with the addition of EGR, peak cylinder pressure increased (till 25% EGR). Above EGR >25% combustion is not sustainable for 3 bar Imep.

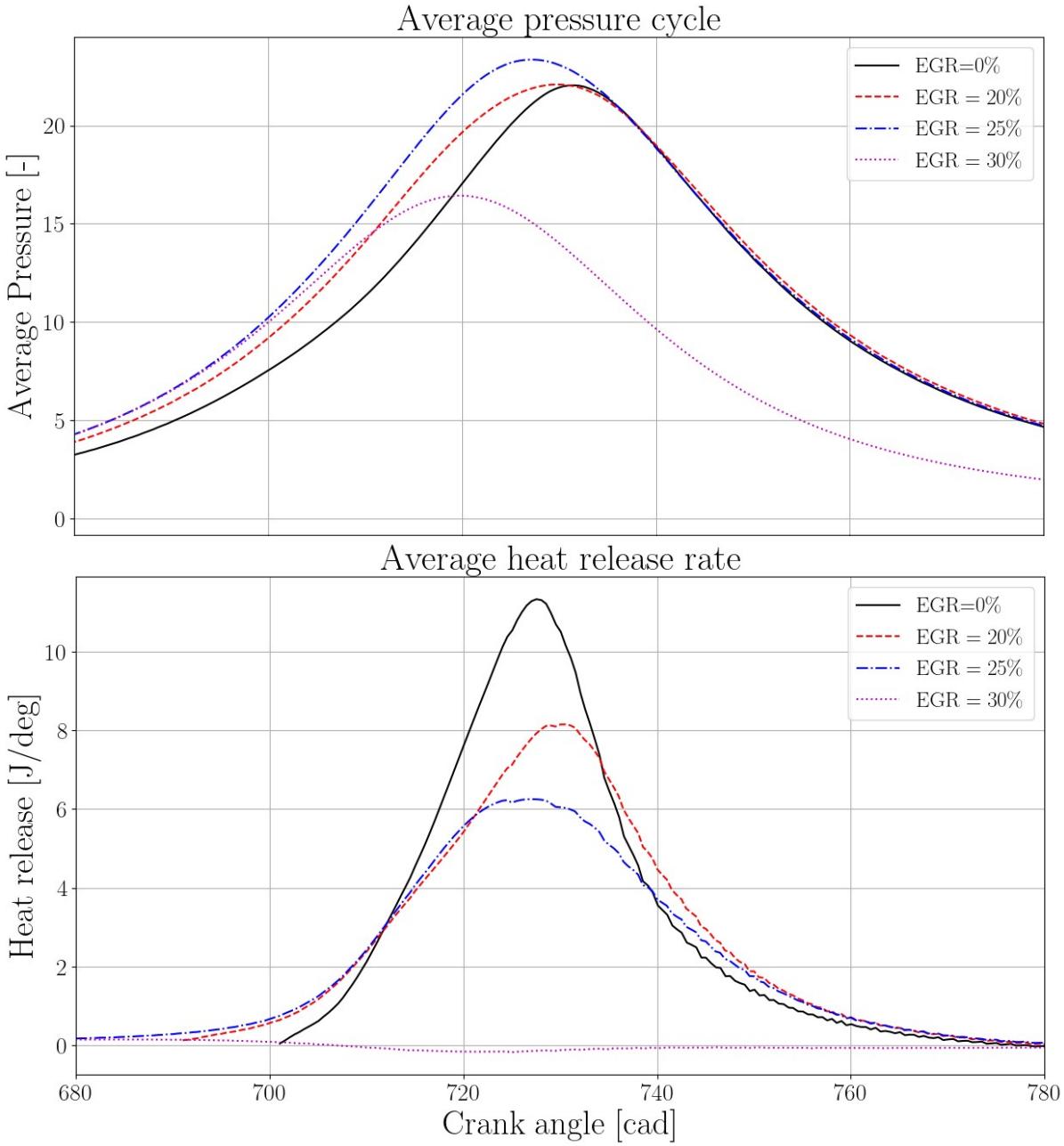

Figure 4.14: 2000 rpm / 3 bar - Average in-cylinder pressure and heat release rates at different EGR rates

Figure 4.15 shows the average in-cylinder pressure and heat release rate for different EGR rates at 8bar Imep. Similar pressure and heat release trends can be seen as discussed before. Combustion is not sustainable for EGR > 30% in the case of 8 bar Imep.

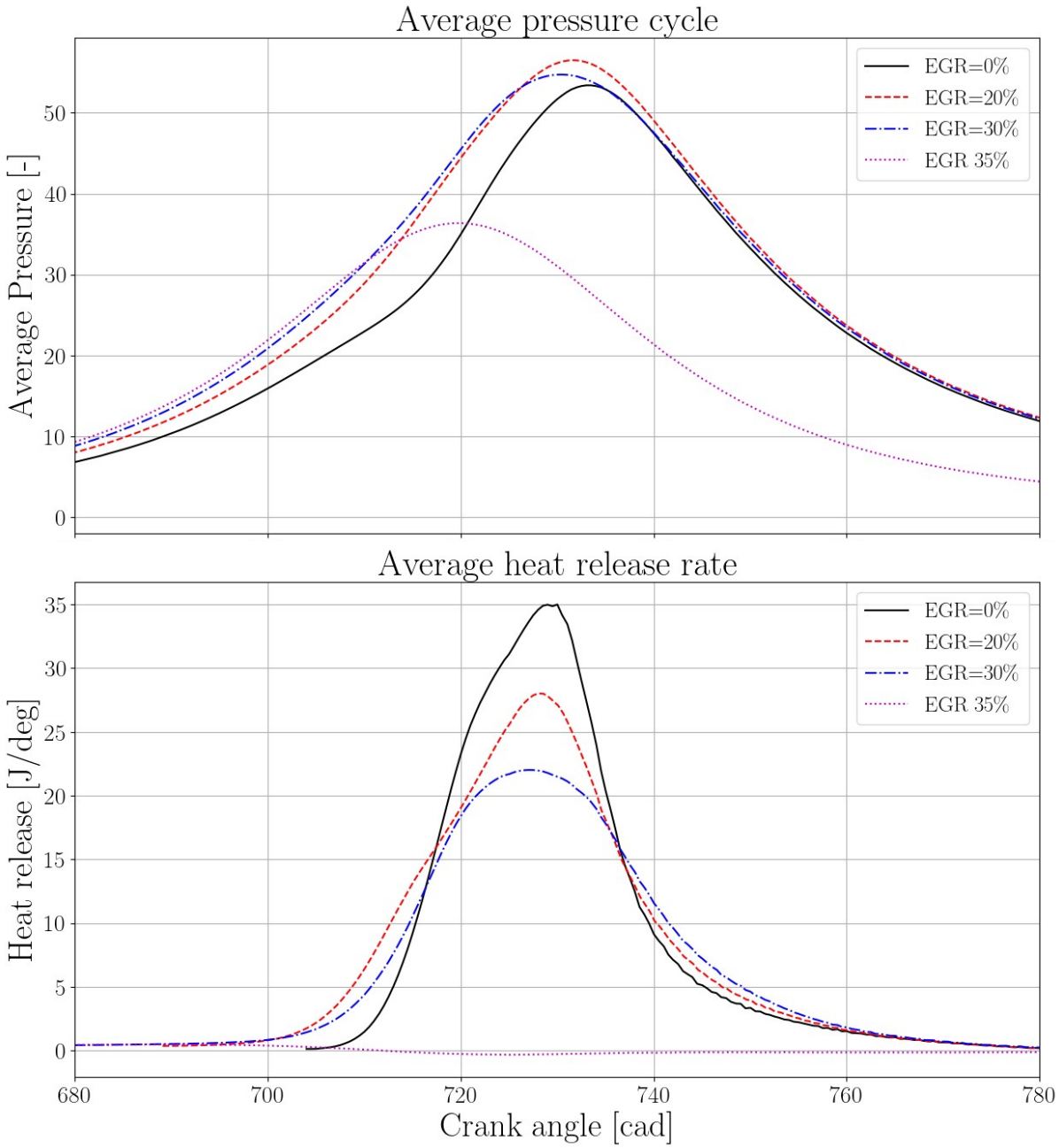

Figure 4.15: 2000 rpm / 3 bar - Average in-cylinder pressure and heat release rates at different EGR rates

Figure 4.16 shows the effect of cooled EGR on combustion duration for 2000 rpm / 3bar Imep. The addition of EGR has a significant effect on the combustion process and combustion stability. EGR slows down the combustion process by reducing the reaction rates which leads to longer combustion time. As can be seen in the figures, the major impact of high EGR is on the combustion initiation phase. The addition of 20% external EGR has increased the combustion duration by 15deg CA of which 8deg CA is in the theta0-10 phase of combustion.

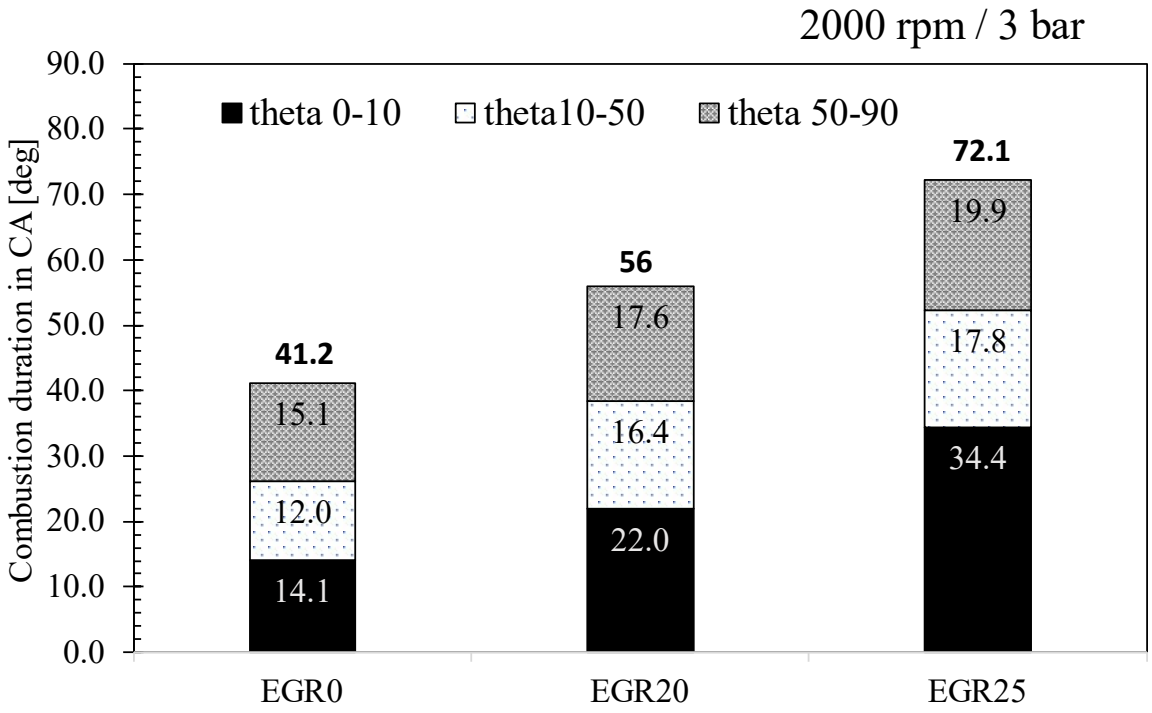

Figure 4.16: 2000 rpm / 3 bar Imep: Combustion duration comparison at different EGR rates

In 8 bar Imep (figure 4.17), increasing 20% EGR in the mixture almost doubles the MFB 0-10 phase of the combustion with respect to no EGR case whereas the MFB 10-50 phasing has a 36% (or 3.6 CA deg) increase. MFB 50-90 phase shows the least amount of change (~13%) which in terms of crank angle corresponds to 1.8 deg. Similar results were found in literature where the addition of 20% EGR increased the initial flame development angle by 50% [122].

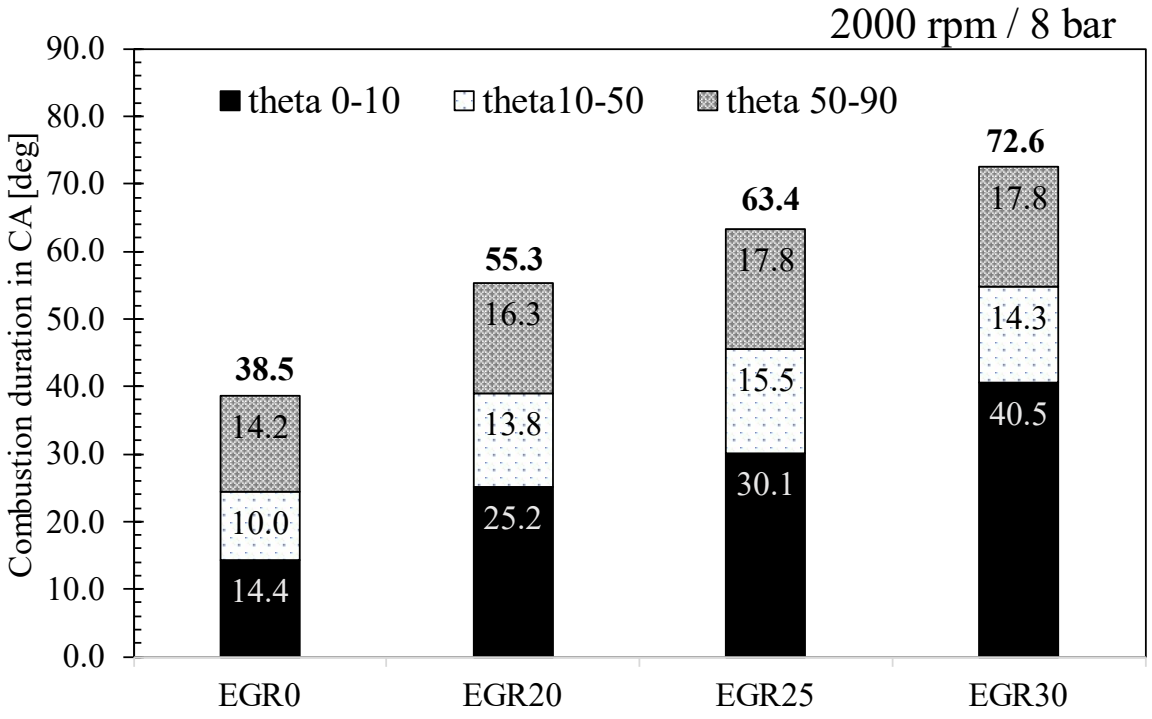

Figure 4.17: 2000 rpm / 8 bar Imep: Combustion duration comparison at different EGR rates

4.4 EGR dilution tolerance at full load

As discussed in the last section, for the full load case (30 bar Imep), the trapped mass of CH4 is within ± 1 % at different EGR rates (Figure 4.18). Figure 4.19 shows spark advance and turbulent intensity at spark advance for part loads as a function of EGR. Spark timing was advanced as EGR rates were increased to accommodate slower combustions with EGR rates. As a function of advance in spark timing, turbulent intensity (u') value at spark timing was also increased. The increase in u' at spark advance with increased EGR will help in the flame development phase.

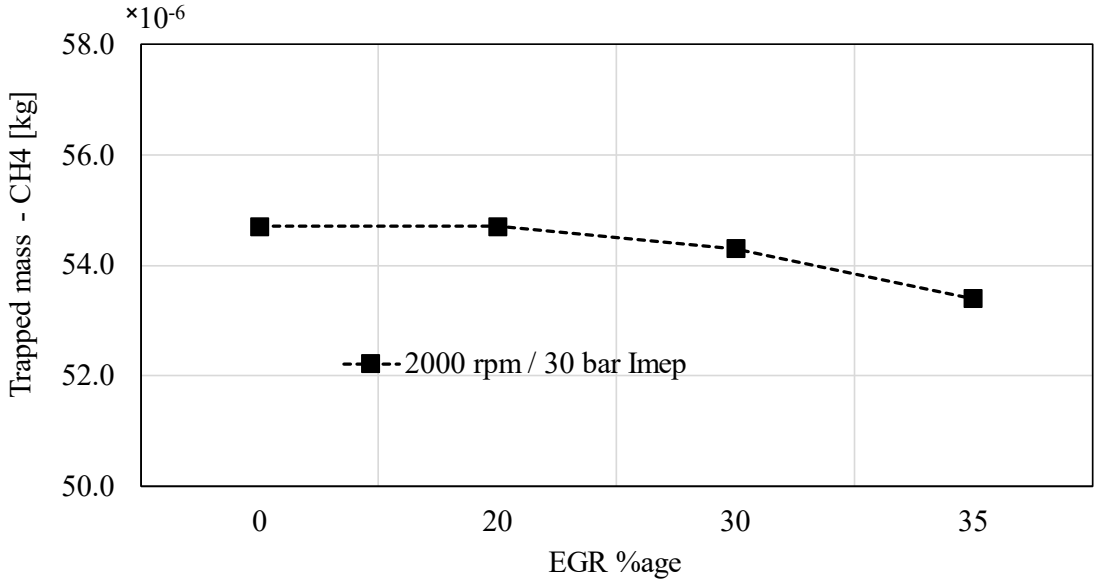

Figure 4.18: Trapped mass at full load as a function of EGR

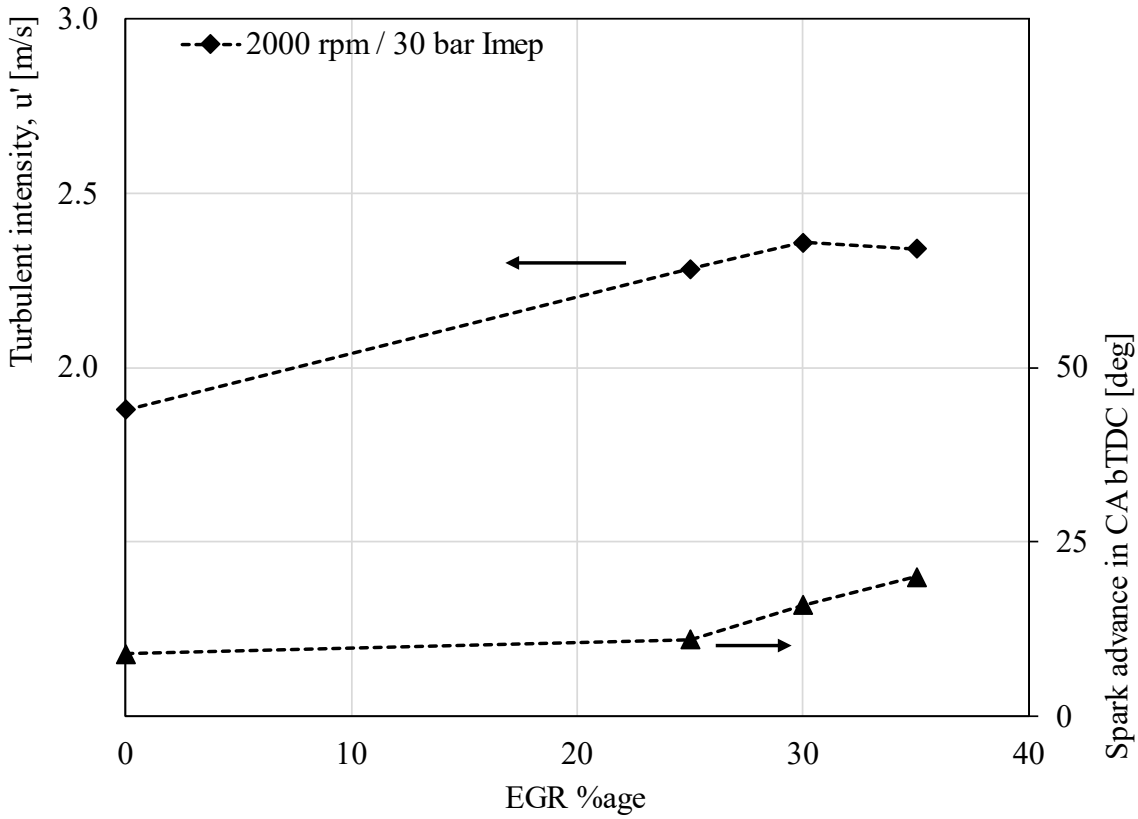

Figure 4.19: Spark advance and Turbulent intensity (u') for part load cases as a function of EGR

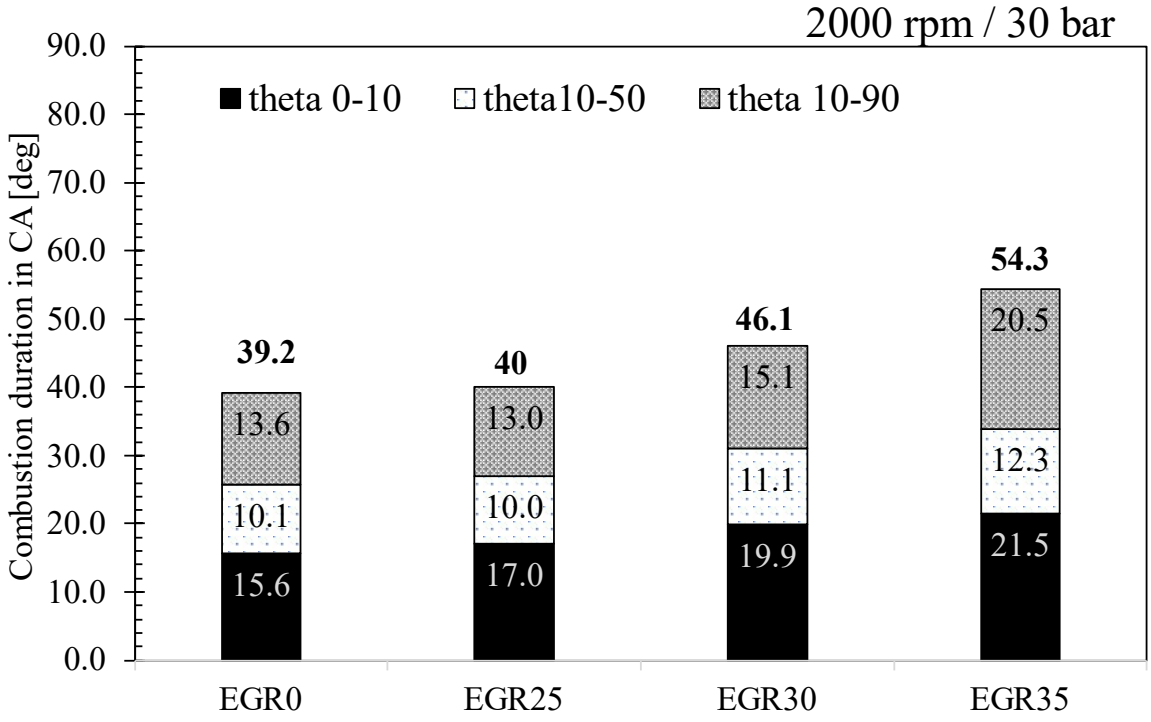

Figure 4.20: 2000 rpm / 30 bar Imep: Combustion duration comparison at different EGR rates

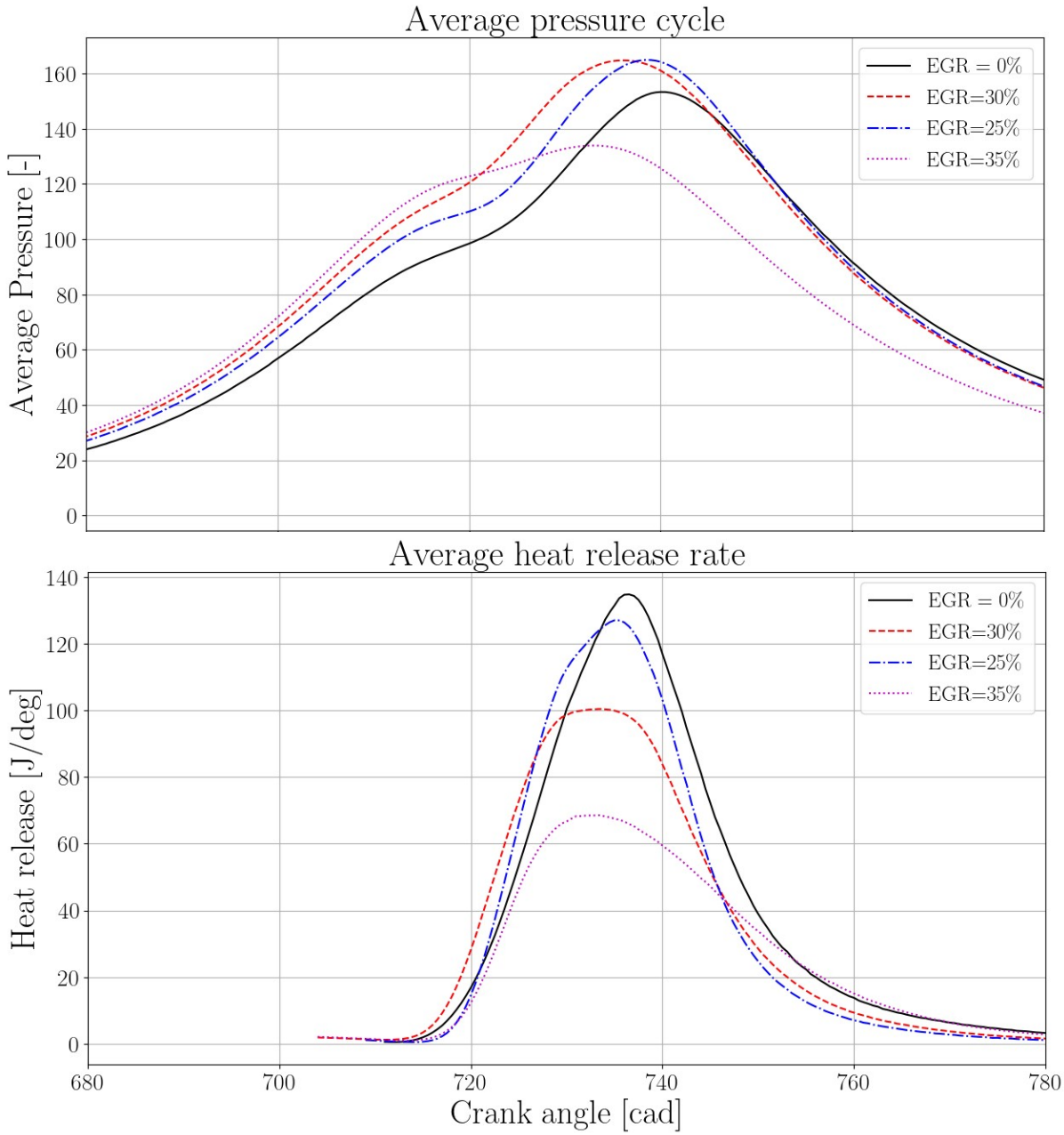

Figure 4.21: 2000 rpm / 30 bar - Average in-cylinder pressure and heat release rates at different EGR rates

Figure 4.21 shows the average in-cylinder pressure and heat release rate for different EGR rates at full load case. The higher intake pressure with increasing EGR rates had resulted in higher trapped mass inside the cylinder and a thus higher-pressure during compression. It can be noticed from the figure that with the addition of EGR, peak cylinder pressure increased (till 30% EGR). Above EGR >30% combustion is not sustainable for 30 bar Imep.

At full load case, increasing 30% EGR in the mixture increases theta0-10 by 4.3deg CA and overall combustion duration by 3.9deg CA (figure 4.20).

4.5 Summary of EGR tolerance

Table 4.1 shows the comparison of overall EGR for 2000 rpm at part load and full load cases. 'External EGR' labelled is the cooled LP-EGR mixed with incoming air. 'Overall EGR' indicates the sum of external EGR and residual gases which remains in the cylinder at EVC. It is worth noting that, with the increase in EGR, higher in-cylinder pressures were observed during combustion which leads to lower in-cylinder residual gas percentage due to the intense blowdown phase.

Figure 4.22 shows lengthscale to velocityscale ratio at MFB50 location for different EGR rates on Premixed turbulent combustion regime diagram. As described in section 3.2, high EGR rates (at EGR tolerance limits) can cause the flame to thermally quench and would result in higher numerical cyclic variations including misfire. For 3 bar Imep, EGR $\geq$ 25% are matching the criteria where combustion at MFB50 is over flamelet limit which would result in in-efficient combustion riddled with cyclic variations and misfire. This can be confirmed from Figure 4.23 which shows average fuel conversion efficiency for different loads as a function of EGR. At EGR = 25%, average fuel conversion efficiency drops to 17% when compared with 23.5% at 20% EGR. This shows that for 3 bar Imep, external EGR limits are around 20%.

For 8 bar Imep, combustion with an EGR rate between 25 and 30 % will be over the flamelet limit (figure 4.22). It can also be noticed in figure 4.23 that fuel conversion efficiency dropped from 41% to 35% between this range. This shows that for 8 bar Imep, external EGR tolerance limits are between 25-30% external EGR. Similarly for the full load case of 30 bar Imep, external EGR limits are around 30%.

As discussed above, with increasing engine load at constant speed, external EGR tolerance limits are increasing while overall EGR remains between 30-31% (Table 4.1). This can be helpful during the engine calibration phase where high load points are difficult to optimize due to high exhaust gas temperatures which can cause damage to the turbine housings. High EGR rates can help in reducing peak burned gas temperatures (figure 4.24) and can allow adjusting the spark timing for optimal torque output while keeping the exhaust gas temperatures within limits. This is especially significant with NG combustion as mixture enrichment to reduce peak temperatures does not work with gaseous fuels. The use of high EGR could be effectively beneficial in maintaining stoichiometric ratio while keeping peak temperatures under component protection limits.

Table 4.1: EGR simulation summary

Engine load IMEP [bar]	External EGR [%]	Overall EGR (Internal+External) [%]
3	0	17
	20	30
	25	32
	30	36
8	0	8.7
	20	25
	25	28
	30	32
	35	36
30	0	2.6
	25	26.2
	30	31
	35	35.6

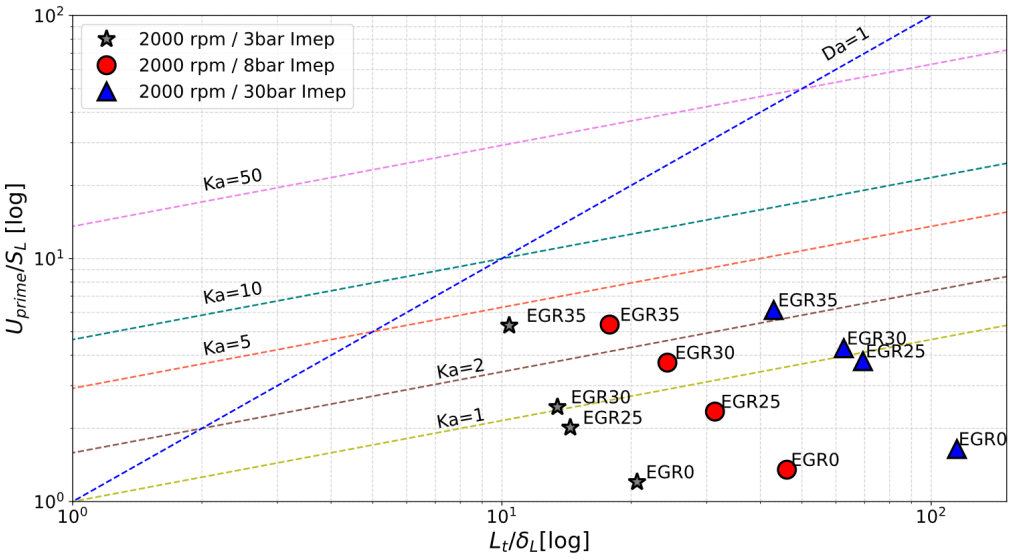

Figure 4.22: Premixed turbulent combustion regime: Lengthscale to velocityscale ratio at MFB50 for different EGR. Load points: 2000 rpm /3 bar, 8 bar and 30 bar Imep

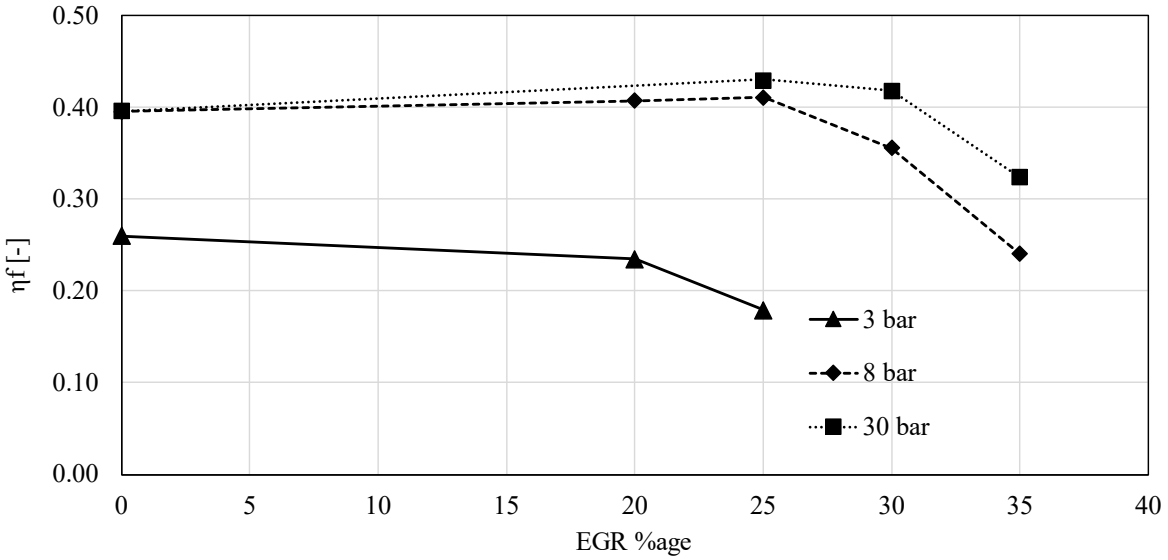

Figure 4.23: Fuel conversion efficiency for part load and full load cases as a function of EGR

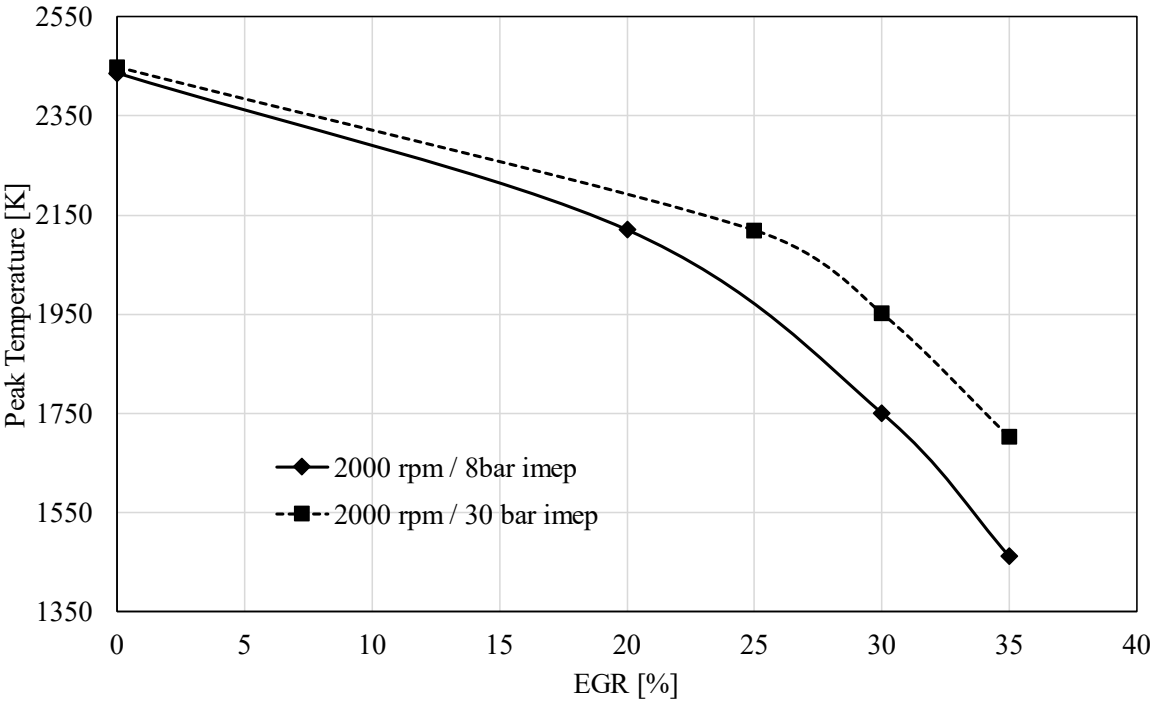

Figure 4.24: Peak combustion temperatures at 8 bar and 30 bar Imep as a function of EGR

Further improvement in combustion stability with high EGR dilution can be achieved by the addition of hydrogen in the fuel. In the next section, the impact of hydrogen addition on EGR tolerance will be discussed in detail.

Chapter 5

Impact of Hydrogen addition on EGR tolerance

As seen in the last section, high EGR rates can increase combustion duration and increase combustion instability due to reduced burning speeds of dilution mixtures. Hydrogen addition in fuel has attracted a lot of attention from the research community due to its wide flammability limits and high laminar flame speeds. This can help in the improvement of combustion stability when diluted with EGR, in NG engines.

It is worth pointing out that hydrogen has been recently identified as a potential key enabler for the energy transition towards a carbon-neutral system. Its blending with NG represents the first step towards its effective introduction into production-ready solutions. Furthermore, hydrogen has the advantage to extend EGR tolerances in the engine. In this section, the impact of hydrogen addition on EGR dilution limits has been presented using the developed numerical model.

First, the 'Low turbulence engine' [section 2.2] was experimentally tested with different amount of hydrogen added to NG [0%, 15% and 25% by volume]. Tests were performed at different engine speed and load conditions under MBT timing, stoichiometric conditions and without EGR [125,126]. The numerical model was first calibrated and validated against these experiments for all three fuel blends at two working points. Then, the numerical model was used to find EGR dilution limits for each fuel blend by mixing EGR in air/fuel mixture in homogenous condition.

This section is divided into four parts where model validation with experiments is discussed in the first part followed by EGR dilution limits for each fuel blends are evaluated. The third part describes the impact of Hydrogen doping on combustion with EGR rates. While last part summarizes the results.

5.1 Model validation

The numerical model was developed for 'Low turbulence engine' [section 3] and was inspired from the model developed in chapter 4 in terms of numerical and mesh settings. The model was first calibrated and validated against experiments for all three fuel blends at two working points. (2000 rpm /6 bar Imep and 3000 rpm / 8bar Imep). The procedure used during simulations is as follows:

- Pressure boundary conditions were taken from experiments (three fuel blends, stoichiometric and with no EGR). A GT-power model of this engine was utilized to derive wall temperature boundary conditions.
- Combustion parameters (α and C_{surf}) were first calibrated for CNG fuel at each working point. The same combustion parameters were used for HCNG15 and HCNG25 blends.
- Same mesh settings were used throughout the simulation campaign.
- LFS calculations with each fuel blends were performed with ARAMCO 2.0 chemical kinetic mechanism in various pressure, temperature, equivalence ratio and EGR conditions, by using LOGE-research software. The results were used as input in the 3D numerical model.
- Validation simulations were performed at 2 load points: 2000rpm / 6bar Imep & 3000rpm / 8bar Imep at stoichiometric conditions (λ=1) and without EGR.
- The model was then used to evaluate EGR tolerance for each fuel blend. Simulations with EGR were performed considering ideally cooled LP-EGR and premixed before entering the cylinder. Laminar flame speeds tables of different fuel blends were used to accurately model combustion behaviour with EGR and H2 blends. Spark timing was optimized for each case to match the target MFB50 obtained during experiments.

Nomenclature used for three different fuels (%vol) in this work:

- NG = 100% + H2 = 0% (CNG)
- NG = 85% + H2 = 15% (HCNG15)
- NG = 75% + H2 = 25% (HCNG25)

Figure 5.1 shows the comparison between experimental measurements and numerical model prediction at 2000 rpm / 6bar Imep with CNG. 'Experimental cycles' are 100 consecutive experimental measurements acquired during experiments while their ensemble average is labelled as 'Avg. experimental cycle'. 'Avg. Numerical cycle' is the ensemble average of 7 consecutive numerical cycles (excluding the first cycle). As can be seen, the numerical model has captured the compression phase with good accuracy. The pressure trace during combustion is also well captured with a peak pressure close to the average experimental curve. The combustion duration (theta0-10 and theta10-90) are shown in figure 5.2 as a function of hydrogen blend percentage (%vol) in fuel. It can be noticed that for CNG (which corresponds to H2=0%, on x-axis), Numerical prediction of theta0-10 and theta10-90 (in red square) are well-matched with experiments (black triangle) and are within ±0.5deg CA. Peak firing pressure (PFP) and its location with respect to the crank position (θ_{PFP}) are incoherent. 50% mass burned (MFB50) location is within ± 2CA deg and is comparable with experiments. The simulated trapped mass has been overpredicted for about 4% on average.

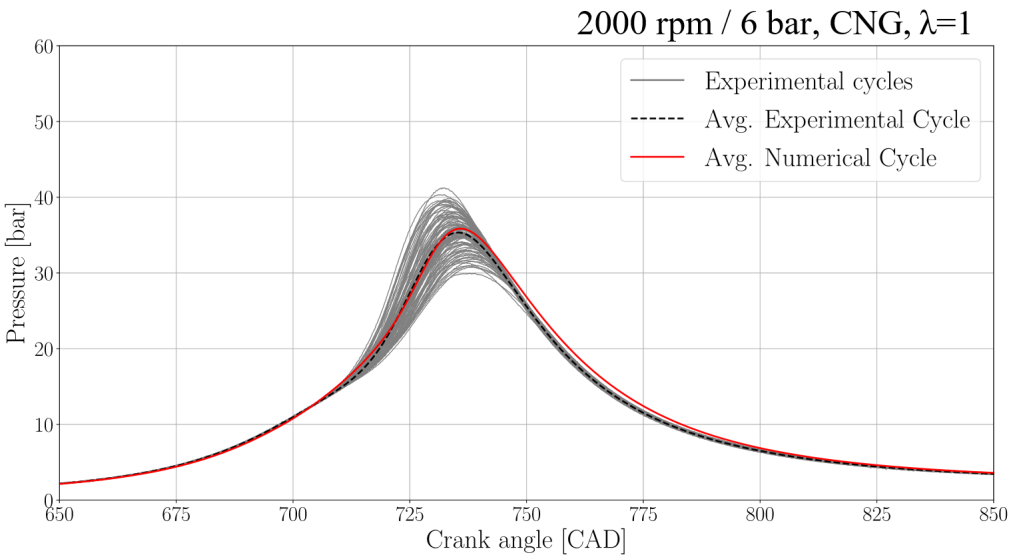

Figure 5.1: 2000 rpm / 6 bar, H_2=0% (CNG) – Model validation

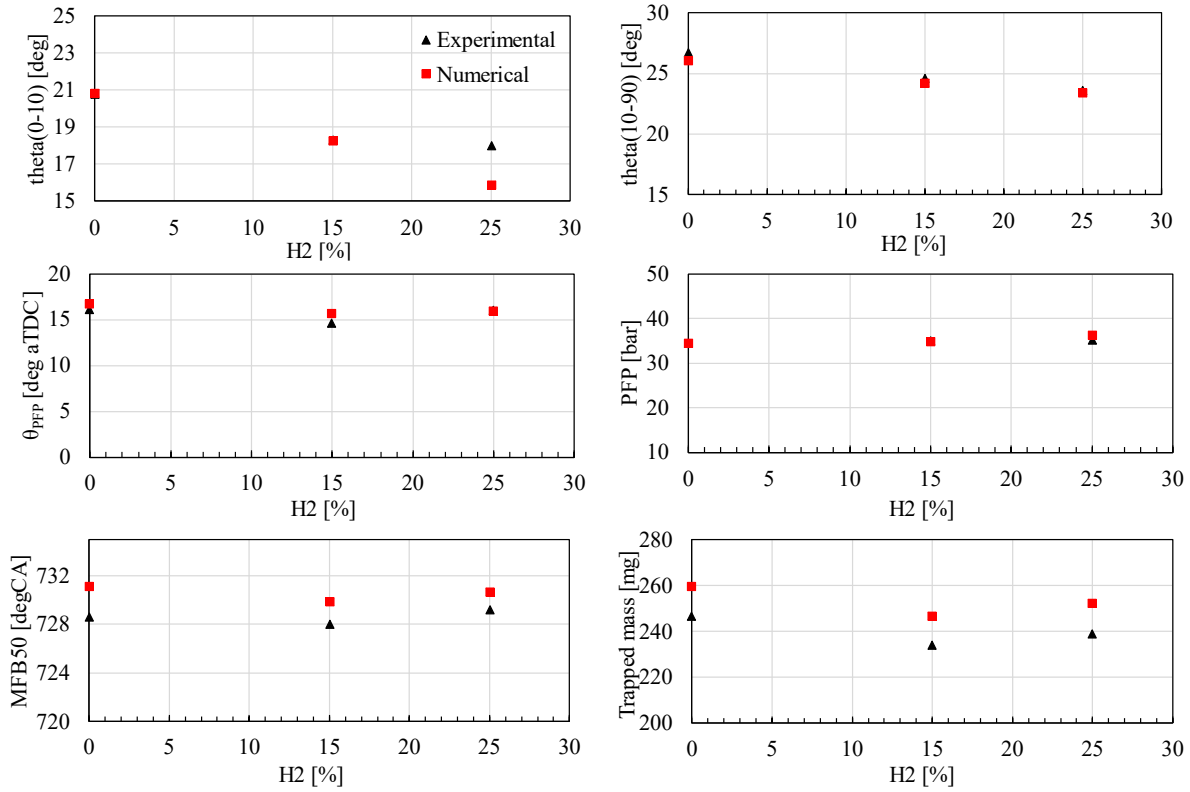

Figure 5.2: 2000 rpm / 6 bar, λ=1 – Experimental and numerical combustion related parameters and trapped as a function of H2 (vol%) blend in fuel

Figure 5.3 shows the pressure trace comparison between experiments and simulations for HCNG15 at 2000 rpm / 6bar Imep. From figure 5.2 & figure 5.3, it can be concluded that the numerical model is able to capture the experimental pressures as well as combustion-related parameters quite accurately for HCNG15. Combustion model parameters for flame stretch (α) and C_{surf} are dependent on in-cylinder turbulence and are kept constant with changing fuel. Results show that with change in fuel from CNG to HCNG15, combustion initiation (theta0-10) and rapid growth (theta10-90) are well predicted. It can be observed that with the addition of H2, theta0-10 duration has reduced indicating the effect of high flame speed of hydrogen. The numerical model is able to capture this phenomenon for HCNG15 fuel.

For HCNG25 (figure 5.4), the numerical model has captured the compression phase quite well thanks to the correct trapped mass. The combustion phase of numerical average cycle is overestimated when compared to the average experimental cycle. Numerical theta0-10 duration is overpredicted by 2deg CA compared to experiments (figure 5.2, H2=25%) which resulted in faster pressure rise after SA. Overall, the average numerical trace is within experimental pressure variation. In all three simulations, in-cylinder pressure during the

expansion phase is slightly overpredicted. It is most likely due to the underestimation of heat transfer to the walls. Peak firing pressure and its phasing were kept constant during experiments for all three fuel blends (figure 5.2). This was achieved by careful optimization of spark timing and engine throttling to keep engine load constant. Similar results were also reproduced by the numerical model as well. The numerical model has captured MFB50 target within 2-3deg CA compared to experiments.

As mentioned before, that the effect of hydrogen addition on combustion is significant during initial flame development. Theta0-10 has reduced by 5CA deg with 25% H2 in fuel. This is due to the high laminar flame speed of hydrogen which impacts the initial kernel development. As combustion progresses, the flame surface area increases due to turbulence which takes over flame propagation. The influence of hydrogen flame speed still has an impact on theta10-90 which is reduced by 2.7CA deg with 25% H2 in fuel. Wang et al. experimentally investigated the impact of hydrogen addition in methane-air mixtures in a constant volume bomb. It was concluded that increasing hydrogen fraction reduced the initial burn rates significantly [127] with a monotonic correlation between reduced burn rates and an increase in OH mole fractions. Ma et al. experimentally found that the addition of 20% H2 (by vol) reduced theta10-90 by 2.5degCA at medium load working point [128].

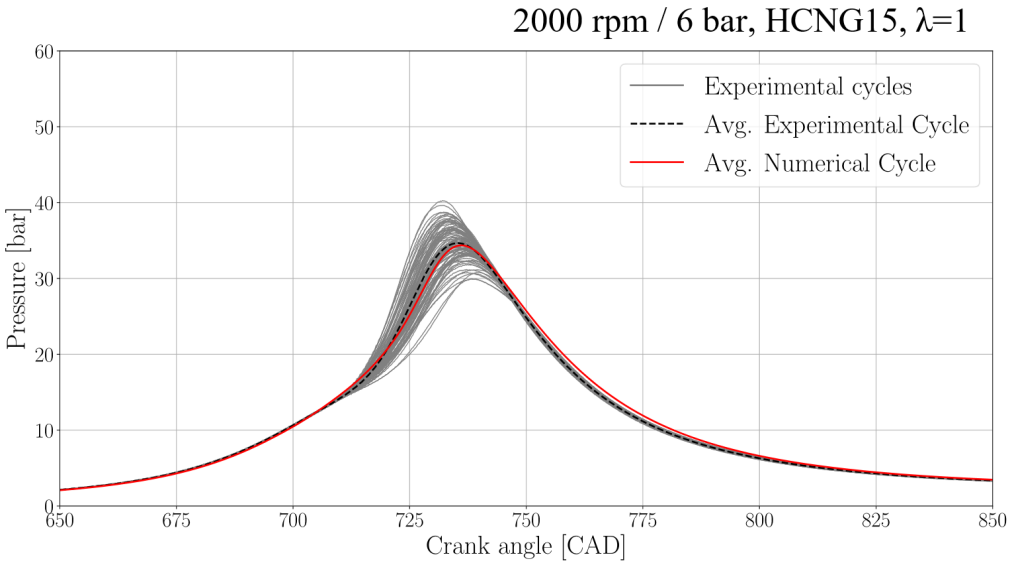

Figure 5.3: 2000 rpm / 6 bar, H_2=15% (HCNG15) – Model validation

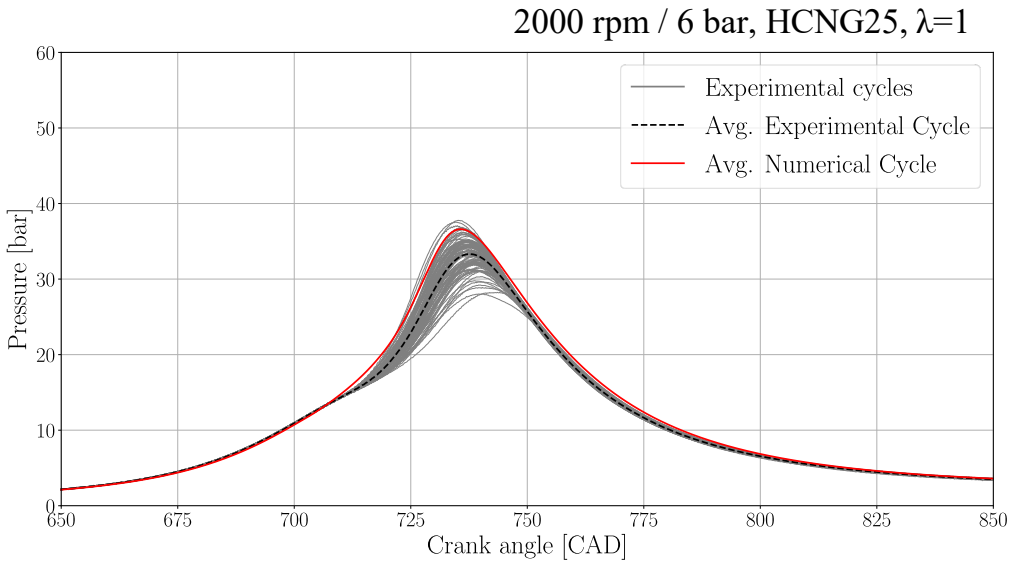

Figure 5.4: 2000 rpm / 6 bar, H_2=25% (HCNG25) – Model validation

For the second working point (3000 /8bar imep), results are shown in figure 5.5-5.8. Figure 5.5-5.7 compares average experimental and average numerical pressure trace while figure 5.8 compares combustion related parameters for all three fuel blends. For this working point, calibration parameters from 2000 rpm / 6bar were carry forwarded to check scalability. The compression phase with all three fuels is well captured whereas the combustion phase is within experimental cycle variation. However, the reason for variation can be linked to overprediction of theta0-10 & underprediction of theta10-90 phase by 1-2deg CA. As the working point was changed, combustion calibration parameters also demand recalibration. For this reason, simulations with EGR were performed with 2000 rpm / 6 bar only.

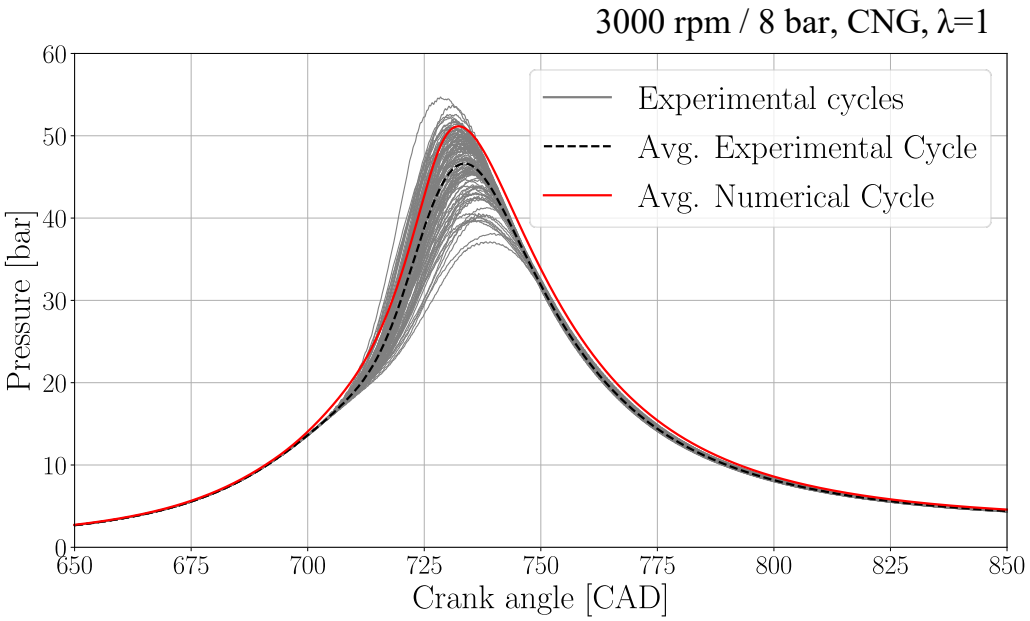

Figure 5.5: 3000 rpm / 8 bar, H_2=0% (CNG) – Model validation

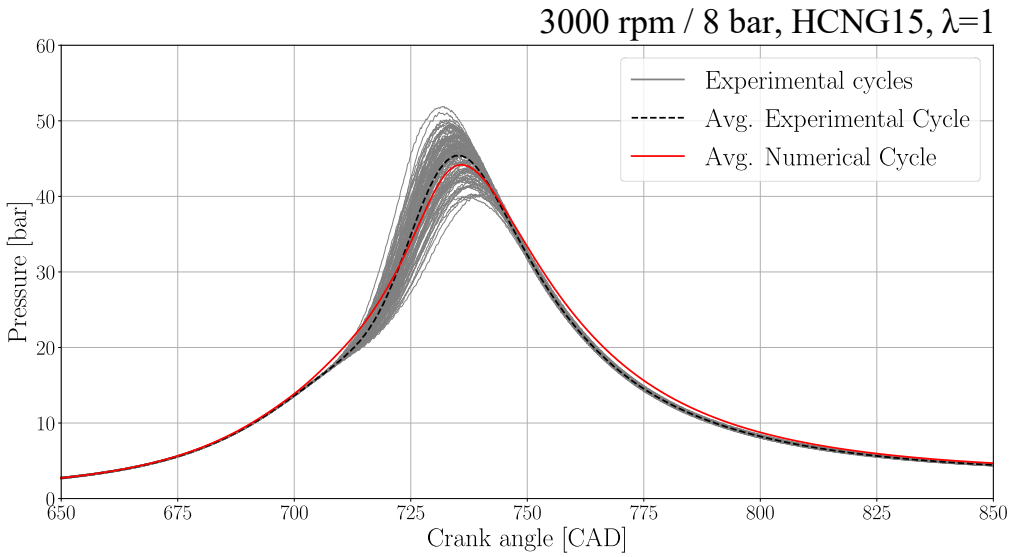

Figure 5.6: 3000 rpm / 8 bar, H_2=15% (HCNG15) – Model validation

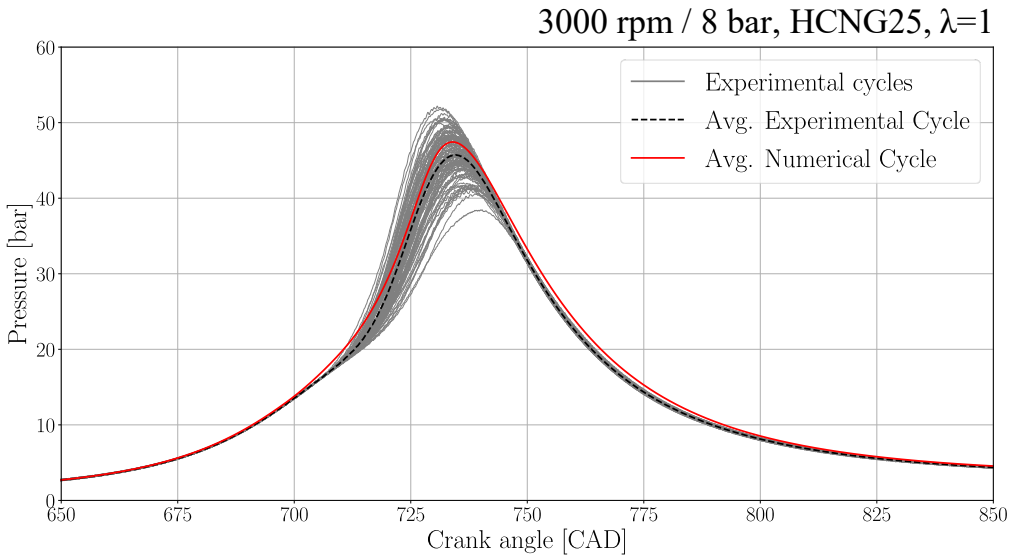

Figure 5.7: 3000 rpm / 8 bar, H_2=25% (HCNG25) – Model validation

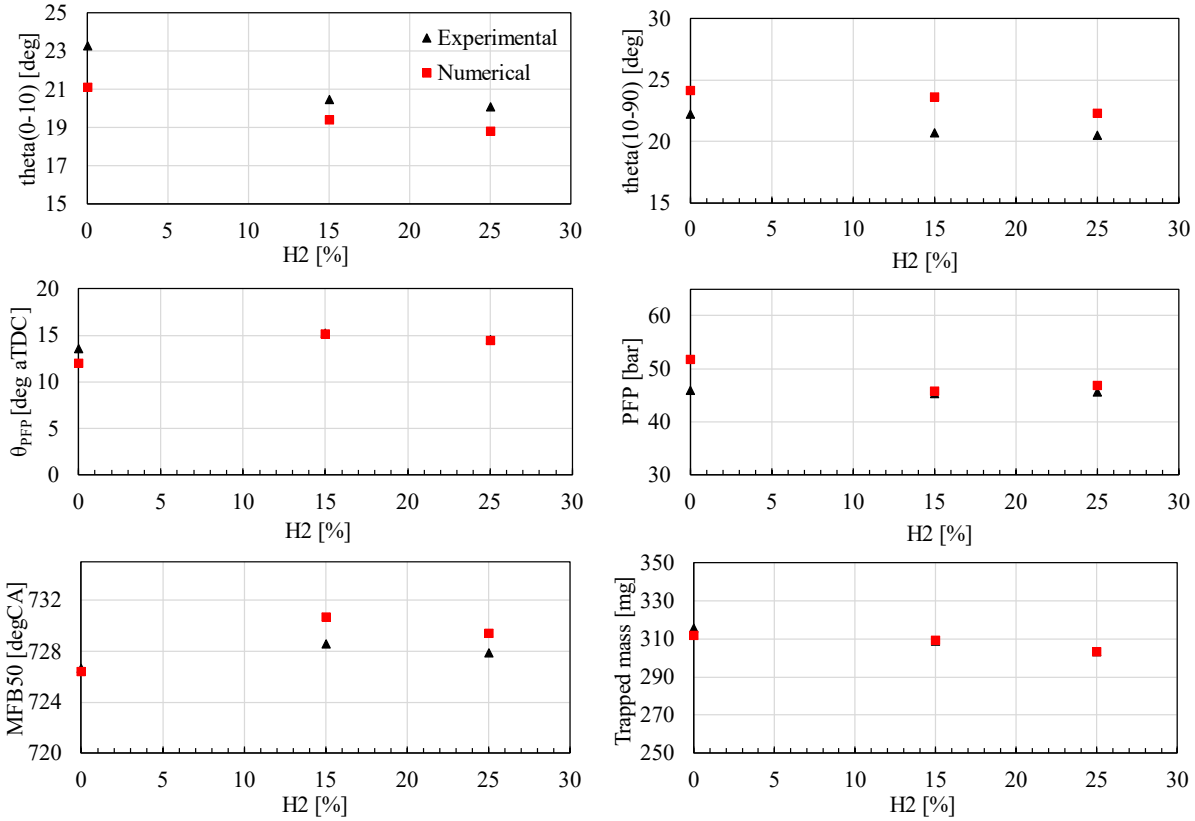

Figure 5.8: 3000 rpm / 8 bar, λ=1 – Experimental and numerical combustion related parameters and trapped as a function of H2 (vol%) blend in fuel

5.2 Influence of Hydrogen addition on EGR tolerance

The validated numerical model was used as a predictive tool to quantify the EGR tolerance of this engine with H2 enrichment. Following parameters were taken into consideration for each simulation:

- Boundary conditions for EGR sweep were derived from an experimentally calibrated GT-power model. Inlet air pressure was calibrated to achieve target Imep.
- Spark advance was calibrated to keep MFB50 within target value of 730 ±2CA deg which represents optimum combustion phasing for 2000 rpm / 6 bar.
- EGR tolerance was detected when heat release was low to achieve target Imep

Figure 5.9 shows the target Imep achieved as a function of EGR rates for three different fuel blends. It can be observed that for CNG, EGR > 10 % was unable to achieve target Imep. However, it was found that the addition of H2 in fuel increased the EGR tolerance rates. EGR rate = 15% was found to be the limit for HCNG15 while EGR=20% was the limit for HCNG25. This indicated that higher flame speeds of H2 increase the EGR tolerance limits of the engine at this working point. Similar results were found in Serrano et al. in which experiments were performed on an engine with similar dimensions and CR as 'Low turbulence engine'. It was seen that the addition of 10 % (by vol.) hydrogen in methane increased the EGR tolerance limits by 5% at low engine load [132].

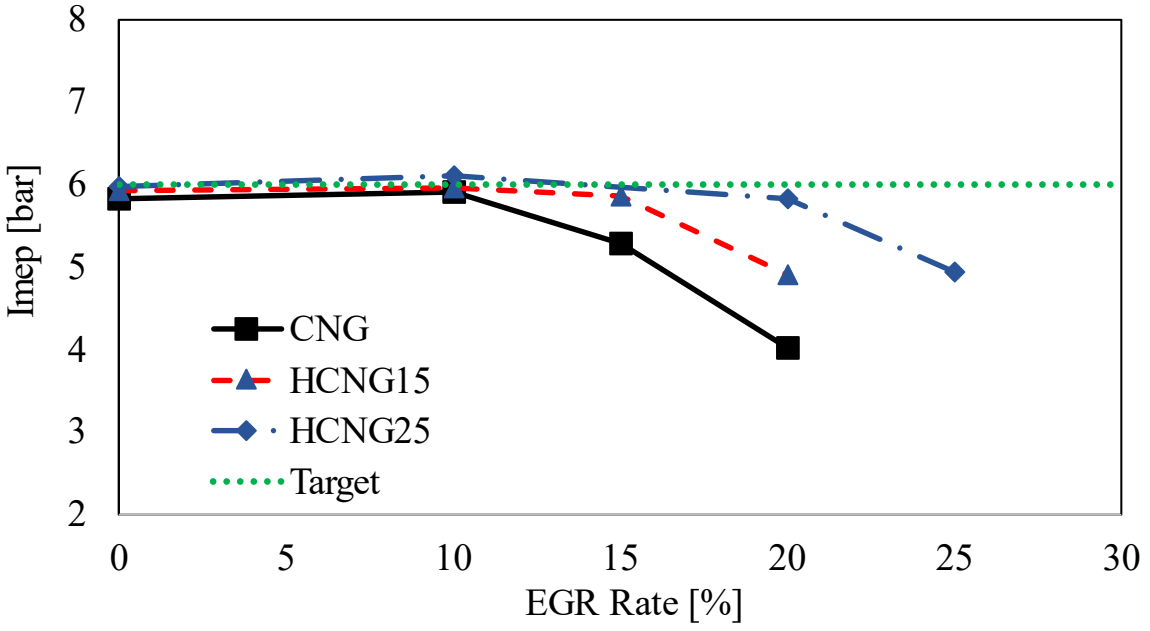

Figure 5.9: Comparison of Imep achieved with three fuel blends in EGR dilution conditions. Target Imep = 6 bar

5.3 Impact of EGR addition on combustion with three fuel blends

Figure 5.10 shows the theta0-10 and theta10-90 comparison between three fuel blends as a function of EGR rates. It can be seen that at the same EGR rate, the combustion duration decreased as hydrogen fraction increased which illustrates that hydrogen addition can increase flame propagation speeds and lead to shorter combustion duration. At EGR=10% (only common EGR tolerable by 3 fuels at this working point), the addition of 15% hydrogen reduced theta0-10 by around 4.2deg CA and theta10-90 by 0.6deg CA. Further increase of hydrogen percentage from 15% to 25% further decreased theta0-10 by 1.8CA deg and theta10-90 by 2.6 deg. Similar trends were found in literature where increasing H2 percentage impacted theta0-10 more than theta10-90 [130,131].

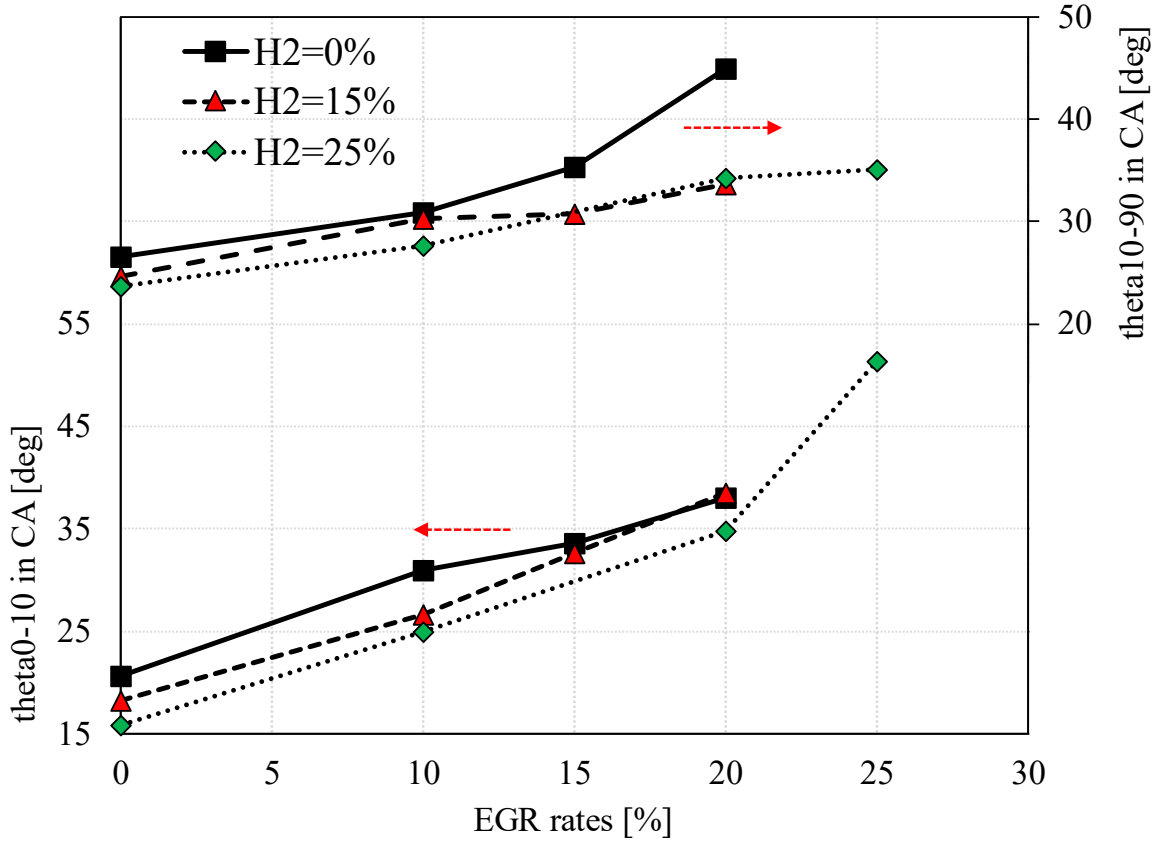

Figure 5.10: Combustion duration phases - theta0-10 on left axis, theta10-90 on right axis for three fuel blends as a function of EGR rates

To estimate the influence of H2 on combustion stability, lengthscale to velocityscale at MFB50 are plotted on a premixed turbulent combustion diagram. Figure 5.11 shows combustion/turbulence interaction at EGR=0% for all three fuel conditions. Recalling the discussion from section 3.2 and section 4.5, combustion with all three fuels are within flamelet regime. Addition of H2 in fuel impacts laminar flame speed (S_L) and flame thickness (δ_L). As the working point is same, u'(U_{prime}) and turbulent lengthscale, L_t have no change from 1 fuel case to another. With increasing H2, we can observe that velocityscale ratio (u'/S_L) is decreasing due to increasing S_L whereas lengthscale ratio (L_t/δ_L) increases as flame thickness is reduced with increasing H2. Decrease in flame thickness with the addition of hydrogen has been experimentally tested in literature where H2 addition of 10% (%vol) in NG resulted in the decrease of flame thickness from 39.6mm to 34mm whereas further H2 addition to 20% (%vol.) led to further reduction of flame thickness to 26.4mm [129].

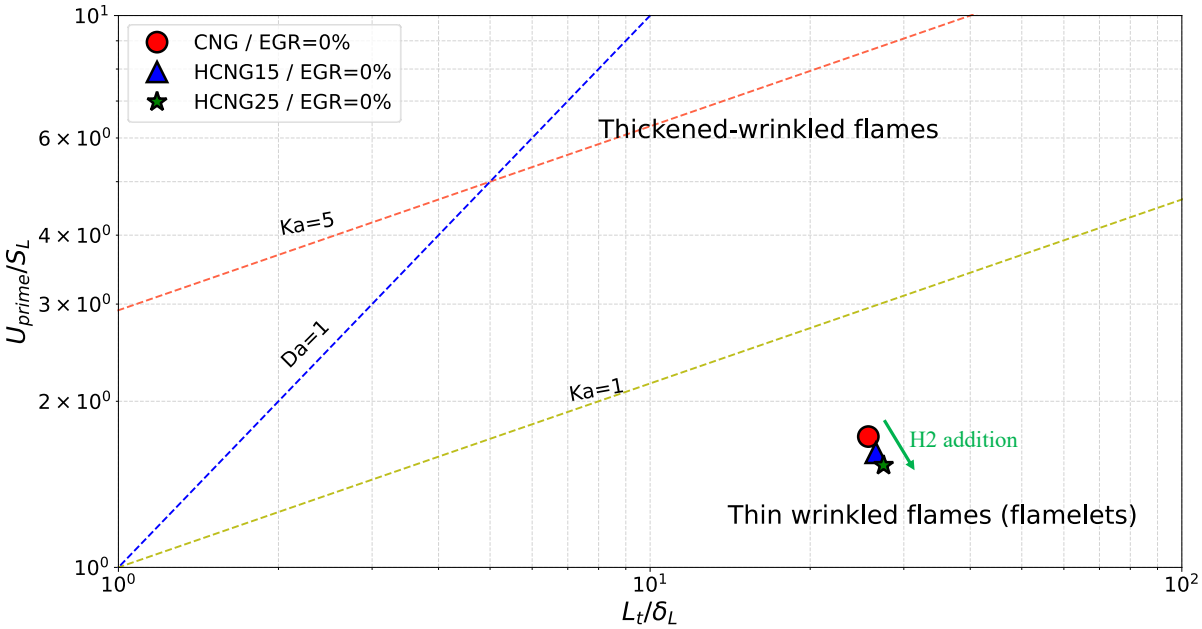

Figure 5.11: 2000 rpm / 6 bar Imep, EGR=0% - Premixed turbulent combustion regime: Lengthscale to velocityscale ratio at MFB50 for three fuel blends

Figure 5.12 shows lengthscale and velocityscale ratios at MFB50 for EGR limit cases with three fuel blends. It can be noticed that all three points are near the Ka=1 limit while still maintaining stable combustion and achieving target Imep (figure 5.9). It can be noticed that with the increase in 15% hydrogen in fuel, EGR tolerance of the engine has increased from 10% to 15%. Further addition of hydrogen from 15% to 25% further increased the EGR tolerance limit by 5%.

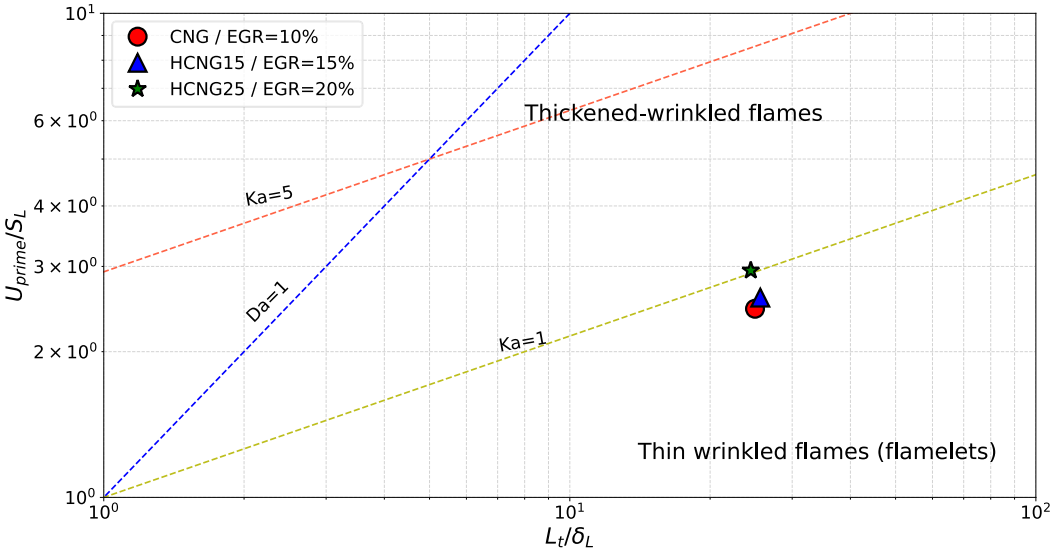

Figure 5.12: 2000 rpm / 6 bar Imep - Premixed turbulent combustion regime: Lengthscale to velocityscale ratio at MFB50 for three fuel blends at EGR limits

5.4 Summary

The numerical simulations on this section were performed to account for the impact of EGR on combustion when H2 is added to NG fuel [0%, 15% & 25% by vol].

- Numerical model developed in this work for 'Low turbulence engine' was validated against experimental data on two working points at 2000 rpm / 6 bar & 8 bar Imep.
- Simulations with increasing EGR rates were performed to predict engine tolerance limits with three different fuel blends.
- It was shown that increasing H2% in fuel increasing the EGR tolerance at a working point. With 15% H2 addition in NG, EGR tolerance increased from 10% to 15%. Further increase of H2 in fuel to 25% increased the EGR tolerance to 20%.
- It was also shown that H2 addition improves the combustion stability.

Chapter 6:

Impact of injection timing with centrally mounted injector on mixture formation and combustion

In a DI system, injection timing plays an important role in mixture formation, volumetric efficiency, and its impact on combustion performance. Early injection, i.e., injection during the intake stroke, is helpful for better mixture formation due to available time and increased in-cylinder turbulence. Though it negatively impacts the volumetric efficiency of the engine which has a direct influence on the low-end torque performance of the engine. Late injection i.e., injection after intake valve closure, can overcome the issue with volumetric efficiency. However, at high speeds and full load condition, the late injection can negatively impact combustion behaviour due to an increase in mixture heterogeneity.

In this section, the impact of direct injection timings with centrally mounted injector on mixture formation, volumetric efficiency and combustion performance has been numerically investigated on 'new engine design'. This section is divided into four sub-sections. In the first part, the impact of injection timing (early and late injection) at 1500 rpm and full loads has been discussed. The working point of 1500 rpm/full load was chosen as at this rpm, the torque curve reaches its peak and thus has high fuel demand at low loads [Figure 6.1]. Next sub-section deals with the impact of late injection on mixture formation and combustion at high engine speeds (4500-6500 rpm). In the third sub-section, the impact of injection timing on low-end torque (1500 rpm / 3bar Imep) has been investigated and the last part summarizes the results obtained in this study.

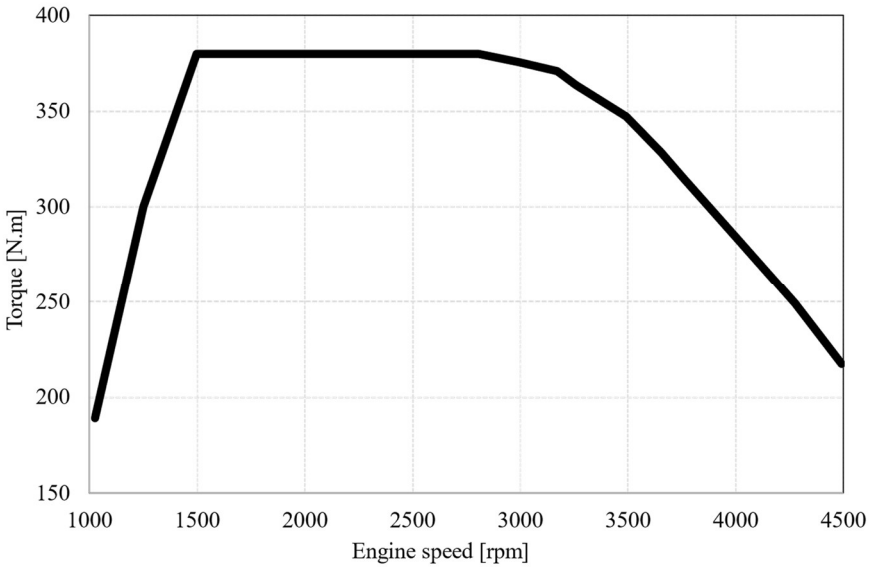

Figure 6.1: Full load torque curve obtain from single cylinder experiments performed by IFPEN

For this, the numerical model discussed in chapter 3 and 4 for ‘new engine design’ was first validated with experimental data in PFI mode. The mixture was considered homogeneous as it enters the cylinder. This step was necessary to quantify the impact of injection timings on volumetric efficiency and combustion behaviour with respect to the PFI engine. The validation results will be discussed in respective sub-sections. Engine geometry was modified to accommodate the injection valve in a centrally mounted location. The injector valve used was an outward opening poppet valve, inclined 22deg from Z-axis (Figure 6.2).

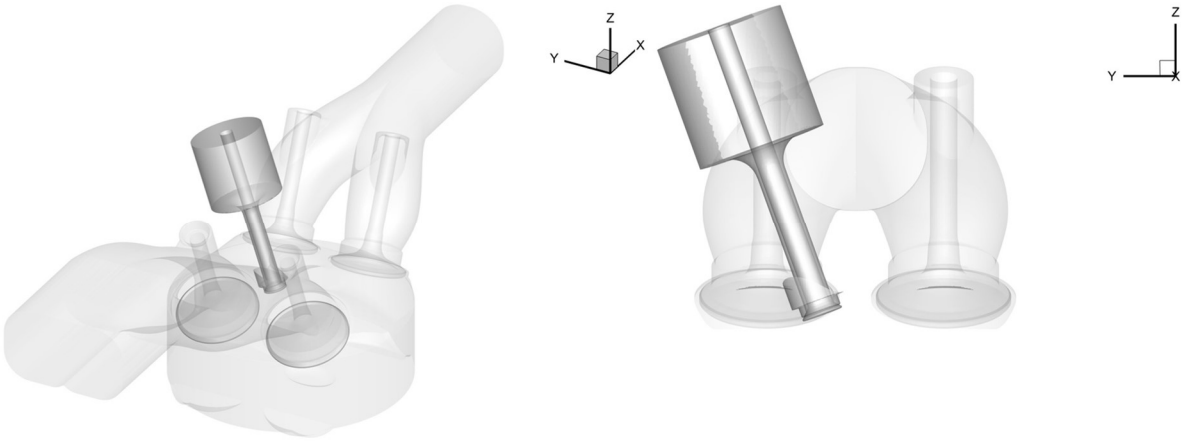

Figure 6.2: Injector location and its inclination

6.1 Impact of injection timing on mixture formation and combustion at 1500 rpm-full load

6.1.1 Model validation - homogeneous conditions

Pressure boundary conditions were taken from experimental measurements whereas temperature boundary conditions were derived from the GT-power model. As discussed in section 3.2, the surface wrinkling parameter (C_{surf}) is dependent on in-cylinder turbulence whereas flame stretch (α) varies with engine load. To keep it consistent with low speeds high load case, $C_{surf} = 2$ and α=0.8 was used. Figure 6.3 shows in-cylinder pressure and heat release rate comparison between experimental measurements and numerical prediction at homogeneous conditions. Experimental data are plotted with solid black line whereas numerical data are plotted with the blue dashed line. The numerical model has well captured the compression phase. Results show that the numerical model has a delay in flame initiation phase by around 2deg CA compared with experiments. This could be due to numerical

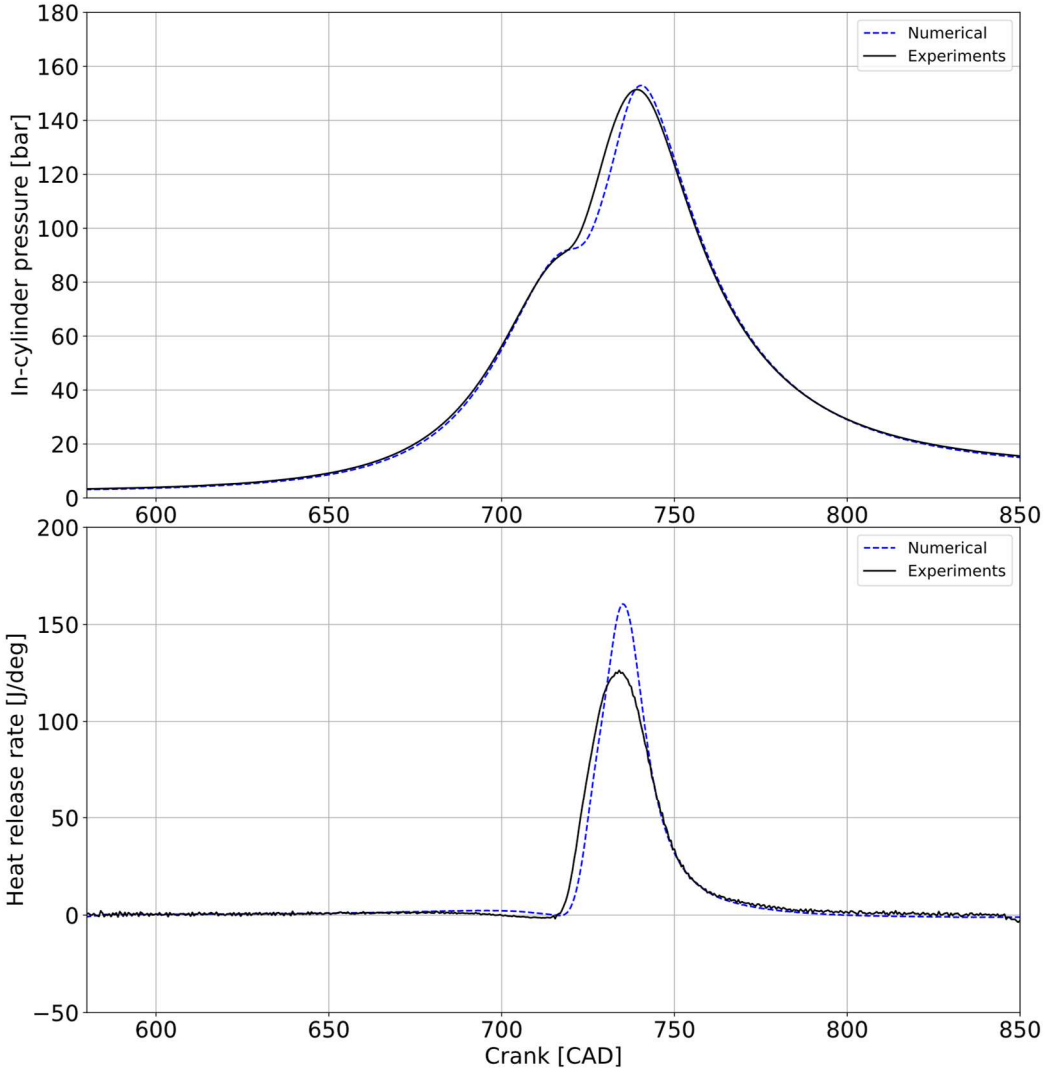

Figure 6.3: 1500 rpm / 32 bar Imep – Model validation in homogeneous conditions

underprediction of initial kernel wrinkling. However, pressure gradients and combustion phasing of MFB50 is well captured by the numerical model.

To understand the influence of injection timing on combustion and mixture formation, simulations were performed with 2 injection timings with the same boundary conditions and numerical settings as the PFI case. Injection timings were calibrated to achieve a stoichiometric air-fuel ratio. First injection timing, henceforth called 'Early Injection', starts at 285CA deg bTDC i.e., during intake stroke (Figure 6.4). Second injection timing, henceforth called 'Late Injection', with SOI 155CA deg bTDC.

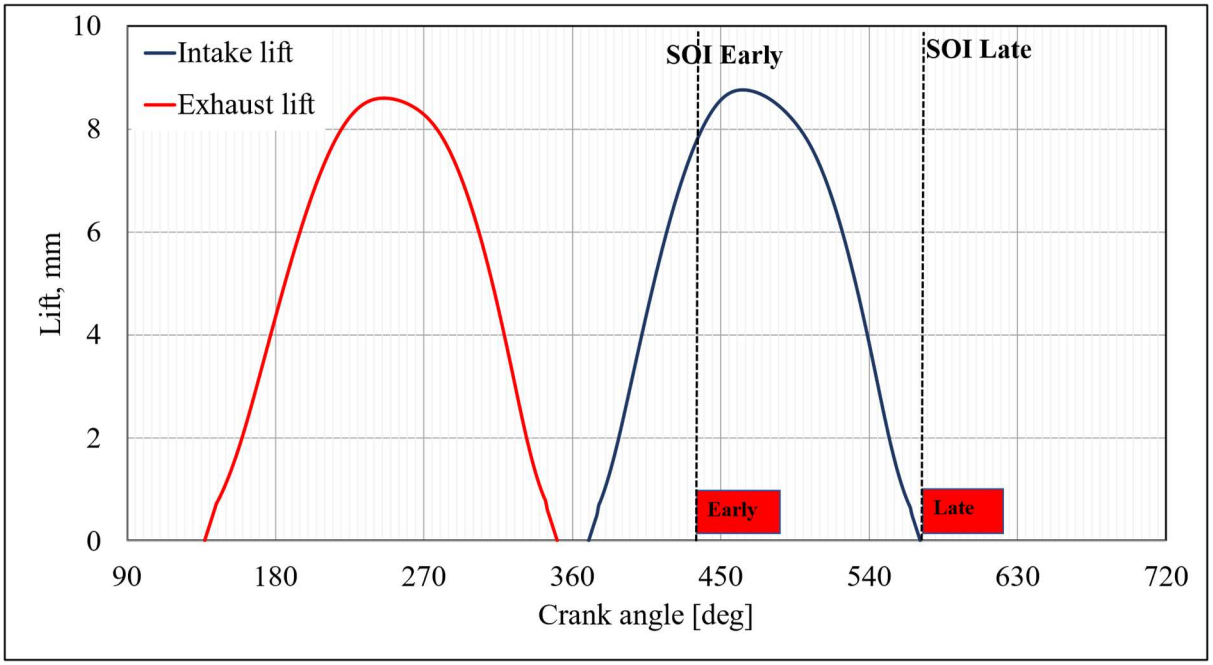

Figure 6.4: Valve lift profile as a function of crank angle. Early and late injection SOI are indicated

Simulations were performed with early and late injection timings and compared with PFI mode.

The impact of injection timing will be discussed in the following order:

- Impact on mixture homogeneity and fuel mass distribution at spark advance
- Influence on combustion speed
- Influence on in-cylinder turbulence

6.1.2 Impact of Injection timing on Mixture formation

In SI engines, tumble motion plays an important role in mixture formation. In the case of DI with a centrally mounted injector, interactions between tumble and incoming injector jet negatively impact the tumble motion. Figure 6.5 shows the tumble ratio along Y-axis for early injection (in red dash-dot), late injection (solid black) and is compared with the PFI case (blue dashed) as the base case. Early injection destroys the rotating structures inside the cylinder formed during intake due to interaction between injector jet and tumble. This can also be confirmed from Figure 6.6 which shows the iso-surface contour of equivalence ratio (value=2), representing injection jet core. Figure 6.6 is in YZ-plane with intake valve towards readers side. The injector jet is almost perpendicular to the tumble motion along Y-axis.

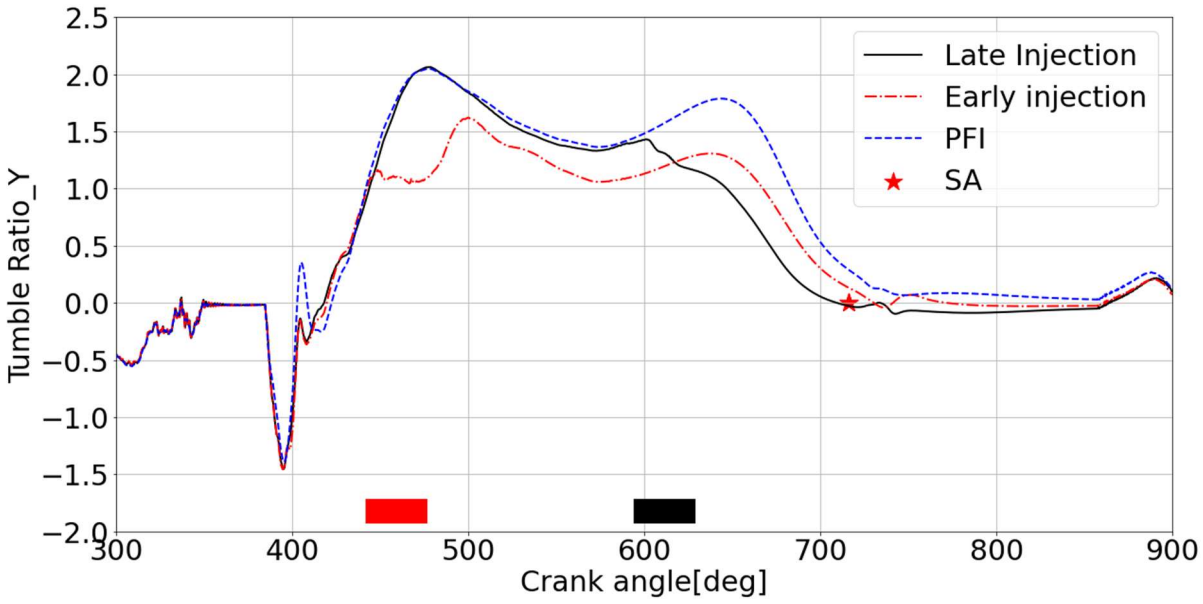

Figure 6.5: In cylinder Tumble motion for early and late injection compared with PFI mode. Bar represents injection timing

a) SOI b) 25degCA aSOI c) 40deg CA aSOI

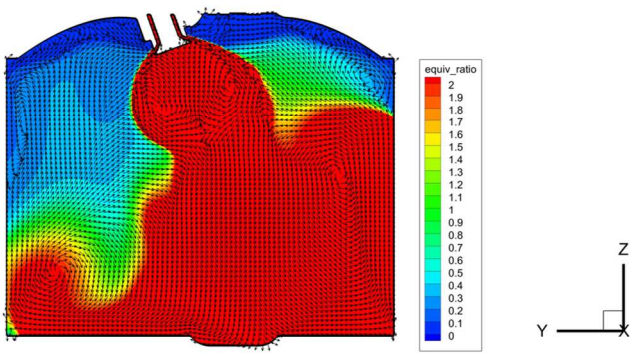

d) 40deg CA aSOI
Contour plot

Figure 6.6: Early injection jet: Iso-surface of equivalence ratio = 2 at a) SOI; b) 25degCA aSOI; c) 40degCA aSOI d) 40degCA (contour plot)

Fig6. a)-d) are at SOI, 25degCA aSOI and 40degCA aSOI respectively. Mixture formation in the case of the centrally mounted injector is due to injector jet and piston interaction as the tumble has already been dissipated. Jet reaches piston surface and starts to spread outwards towards cylinder walls. The spread of jet plumes also is affected due to incoming air. After reaching the walls, jet creates recirculating vortices (Fig6-d)). These vortices will help in initial mixture formation.

At the end of injection, the tumble slightly recovers again as the intake valve is still open which is noticeable in Figure 6.5 at 500degCA, tumble has started to recover but still has not reached the same level as the PFI case. Figure 6.7-a) shows that the additional incoming air from the intake valve after EOI that remains attached to the cylinder head and starts to form tumble motion, pushing fuel to the left and towards the intake valve. This will lead to some fuel leaving the chamber and enter the intake port (figure 6.7-b).

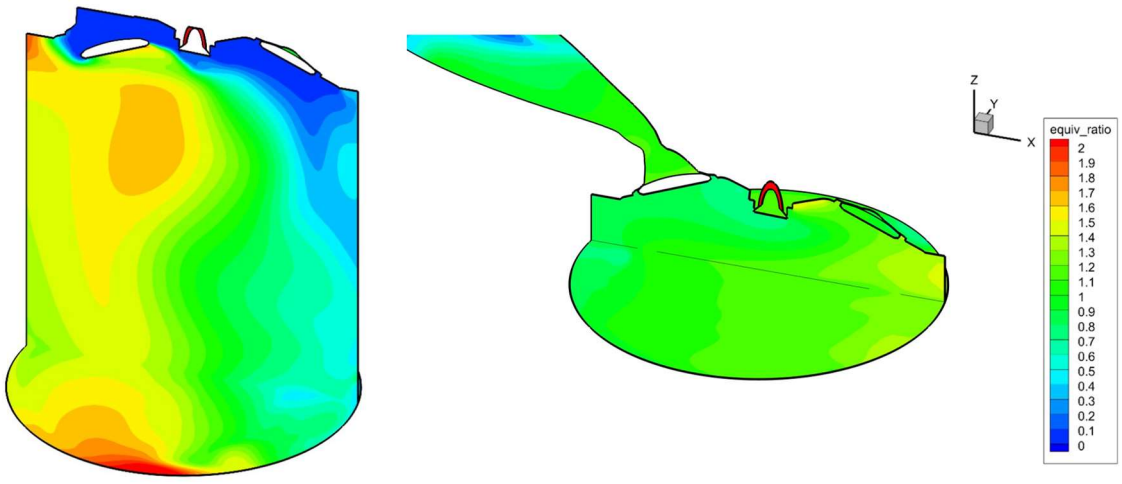

a) 70deg CA aEOI

b) 210deg CA aEOI

Figure 6.7: Early injection jet: Tumble recovery after EOI a) 70degCA aEOI; b) 210degCA aEOI. Slices shown are in Y & Z planes with equivalence ratio contours. Intake valve cut section can be seen on Y-plane (left side) whereas exhaust valve is on right side.

Late injection event will also destroy the tumble during the injection. Figure 6.8 shows the injector jet evolution from SOI till it interacts with cylinder walls. A similar phenomenon of jet impingement and fuel spread is seen as the early injection case. One difference that can be seen is that in the case of late injection, jet plumes are more concentrated on one side of the cylinder. If figure 6.6-c) is compared with figure 6.8-c), a clear distinction can be observed as in the case of early injection, jet plumes are spread all over the piston surface. This can be due to its interaction with incoming air.

Figure 6.9 shows the vortex structure evolution and mixture formation process for late injection. It can be seen that the vortex cores produced due to jet interaction with piston and cylinder walls are propagating towards TDC as the piston is moving upwards. These vortex structures were missing from the Early injection case which can influence the combustion progress and is discussed in 5.2.2.

Figure 6.7-b) and 6.9-c) shows the mixture homogeneity at 35degCA before firing TDC between two injection timings. It can be seen that in the early injection case, all the fuel mixture is within the flammable region (equivalence ratio between 0.7÷1.7). whereas in the case of late injection, higher heterogeneity can be observed. However, both cases will reach homogeneity at spark timing.

a) SOI b) 25degCA aSOI c) 40deg CA aSOI

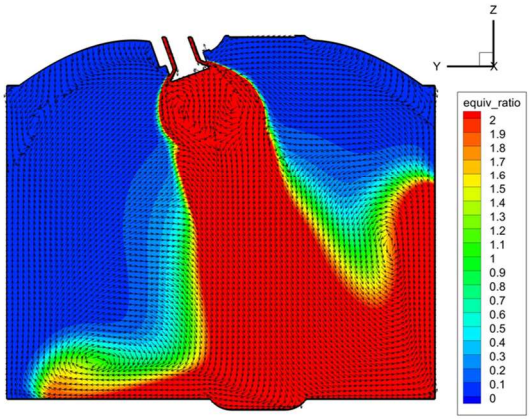

c) 40deg CA aSOI
Contour plots

Figure 6.8: Late injection jet: Iso-surface of equivalence ratio = 2 at a) SOI; b) 25degCA aSOI; c) 40degCA aSOI, d) 40degCA aSOI with contour plots

This can be confirmed from figure 6.10 which shows the coefficient of variation (CoV) (left Y-axis) of local fuel concentration inside the combustion chamber and flammable fuel fraction (FF) (right Y-axis) for two injection events. CoV gives an index of homogeneity in the computed domain and is calculated by comparing the cell-wise standard deviation of the mass of fuel over average fuel mass. Whereas FF is obtained by summing up the mass of fuel in all computational cells whose cell-wise relative air-fuel ratio is between 0.7 and 1.7 (section – nomenclature). Spark timing is marked with a red star which is at 715deg CA. The lower value of CoV means less standard deviation of fuel mass from cell to cell whereas FF = 1 means all fuel mass is within flammable range.

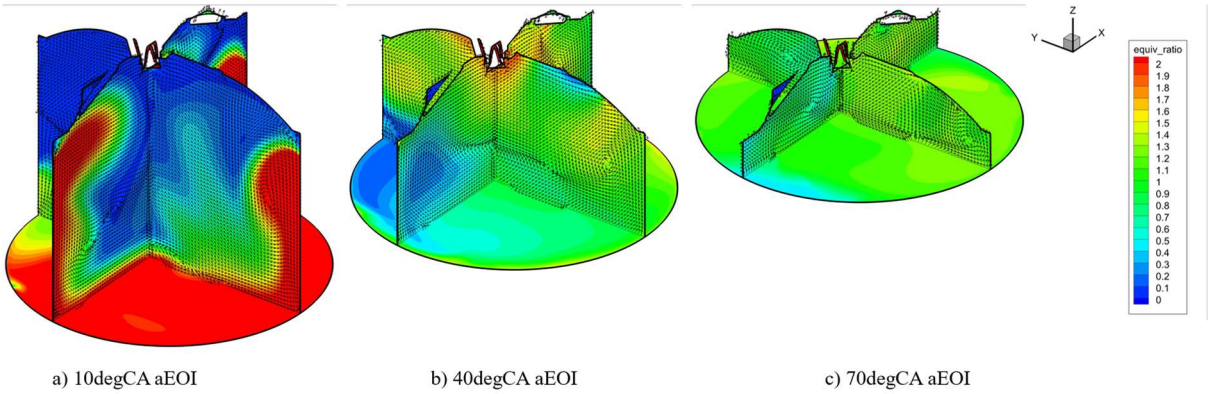

Figure 6.9: Late injection jet: In-cylinder turbulent structure and mixture formation. Slices shows are in X, Y (Tumble motion axis) & Z (Piston surface) plane. On Y-plane, intake (front side) and exhaust (back side) valve can be seen

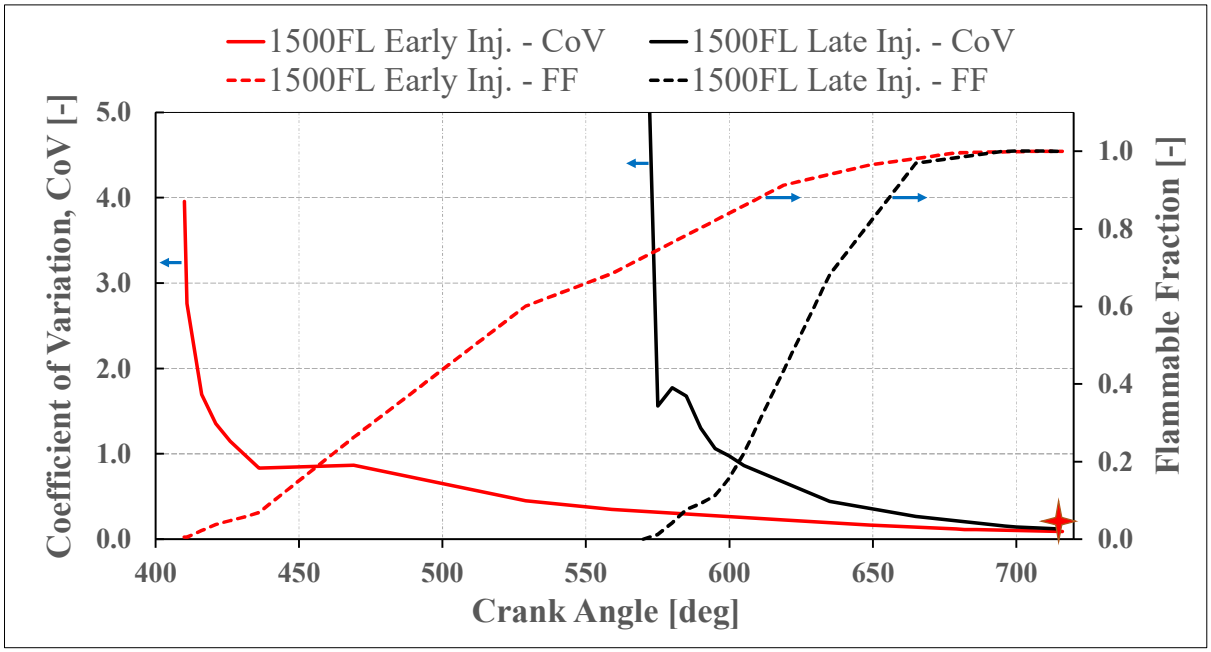

Figure 6.10: 1500 rpm, Full load: Coefficient of variation and flammable fraction as a function of Crank angle for early and late injection events

In Early injection event, there is sufficient time available for mixture formation. Though mixture formation in early injection is slow which can be observed from the slope of FF, it has reached quite a good homogeneity. This is indicative from FF =1 and with little fuel mass variation (CoV) at spark timing. In the case of Late injection, mixture formation is fast and is due to turbulence induced by the injector and piston's movement towards TDC. In this case as well mixture is within flammable limits. Figure 6.11 shows the fuel mass fraction distribution as a function of equivalence ratio at spark timing. It can be noticed that, in late injection, though

the overall CoV was quite low, there is still some variation in fuel mass distribution. In the case of early injection, ≈ 74% of fuel mass is within the range of 0.9÷1.1. While in the case of late injection, this fraction is around 52% indicating that mixture formation is more stratified.

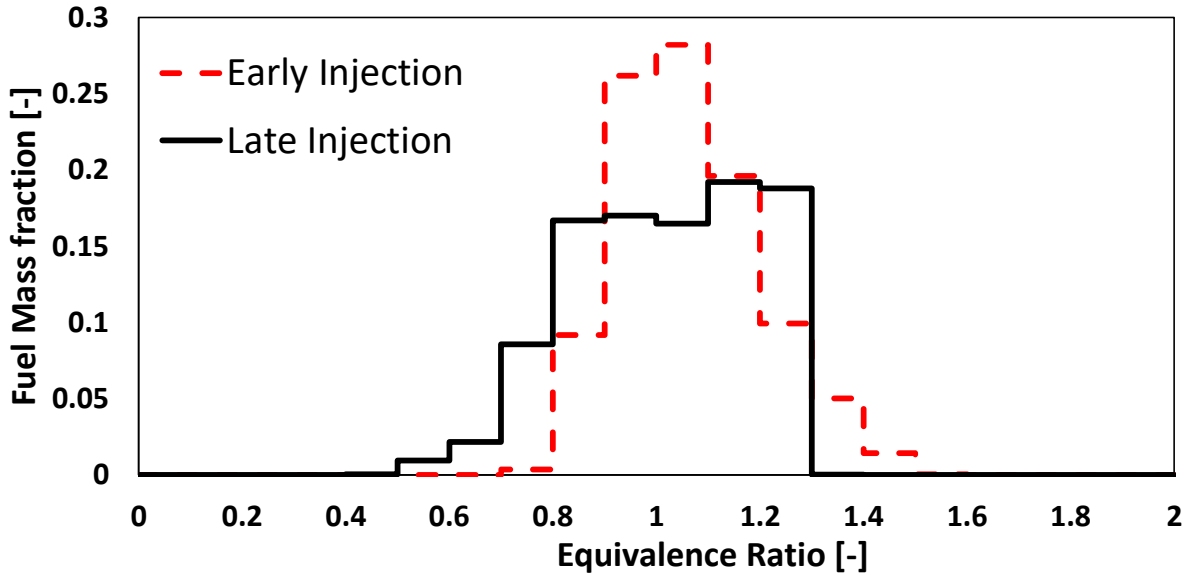

Figure 6.11: 1500 Full load, Mixture distribution at spark timing for early and late injection events.

6.1.3 Impact of injection timing on combustion

Figure 6.12 shows the combustion duration of both injection timings in comparison to PFI mode. It can be noticed that in the case of the early injection event, combustion duration has noticeably increased with respect to PFI mode. This indicates that in the case of early injection, the interaction of injector jet with in-cylinder air has created an unfavourable condition that impacted the combustion duration adversely. There is an 11 CA deg difference between the combustion duration of early injection and late injection. It can also be seen that TKE at spark timing in early injection case is lowest among all 3 cases (figure 6.13). This affected theta0-10 and theta10-50 duration as turbulence are not enough to increase turbulent diffusivity between the flame and unburned mixture. Further investigation of TKE at spark location (figure 6.14) shows that the local TKE near spark location in case of Early injection is much lower compared to both PFI and Late injection. Also, the vortex structure present in the PFI case is missing for the early injection case. These structures would help spread the flame in PFI combustion. This explains the slower flame initiation in Early injection case.

Comparing the PFI case with late injection, it can be noticed that both cases have similar combustion speed in theta0-50 duration. TKE in both cases is similar with only 0.6 m2/s2 difference (figure 6.13). Also, the late injection has 2 circulation motions present (figure 6.14). The main difference between the two is in the theta50-90 phase. This difference could be due to higher turbulence in late injection case, arising due to injector jet which can lead to reduced wall quenching. This was seen in figure 6.9-c) where vortices formed due to injector, piston and cylinder wall interaction were still visible 35degCA bTDC and are also seen at spark timing (figure 6.14). Literature has shown that the NG DI injection event increases the mixture flame speeds [39]. Singa et al. also showed that the DI induced higher turbulence in the chamber and can reduce the combustion duration from half to one-tenth compared with homogeneous combustion which is accompanied by a rise in in-cylinder pressure. In this work, similar results were noticed with Late injection timings (figure 6.12 & 6.15).

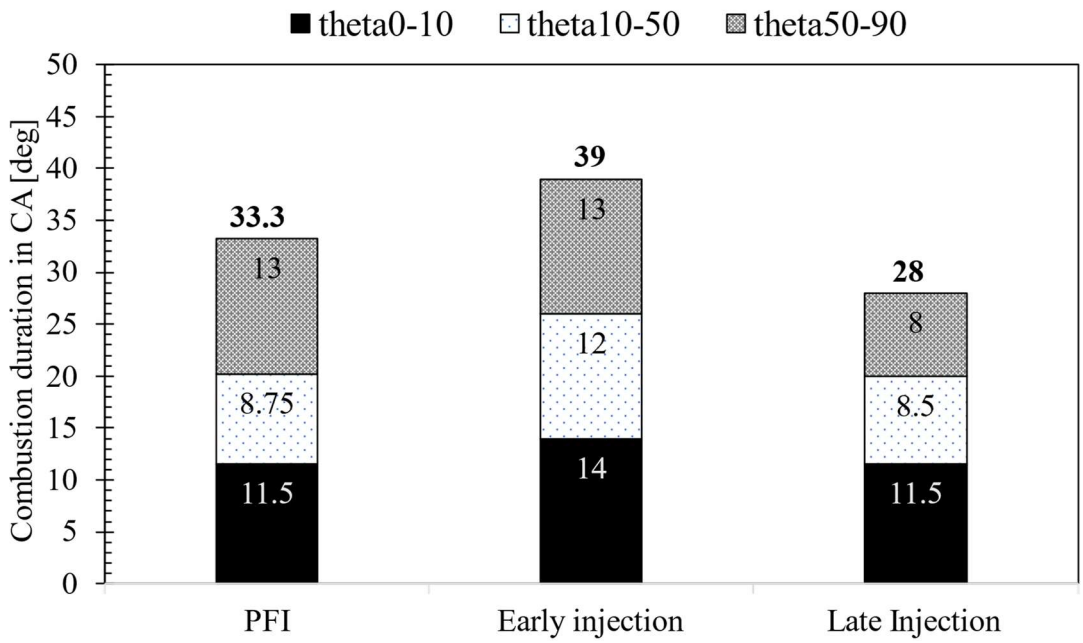

Figure 6.12: 1500 Full load- Combustion parameters

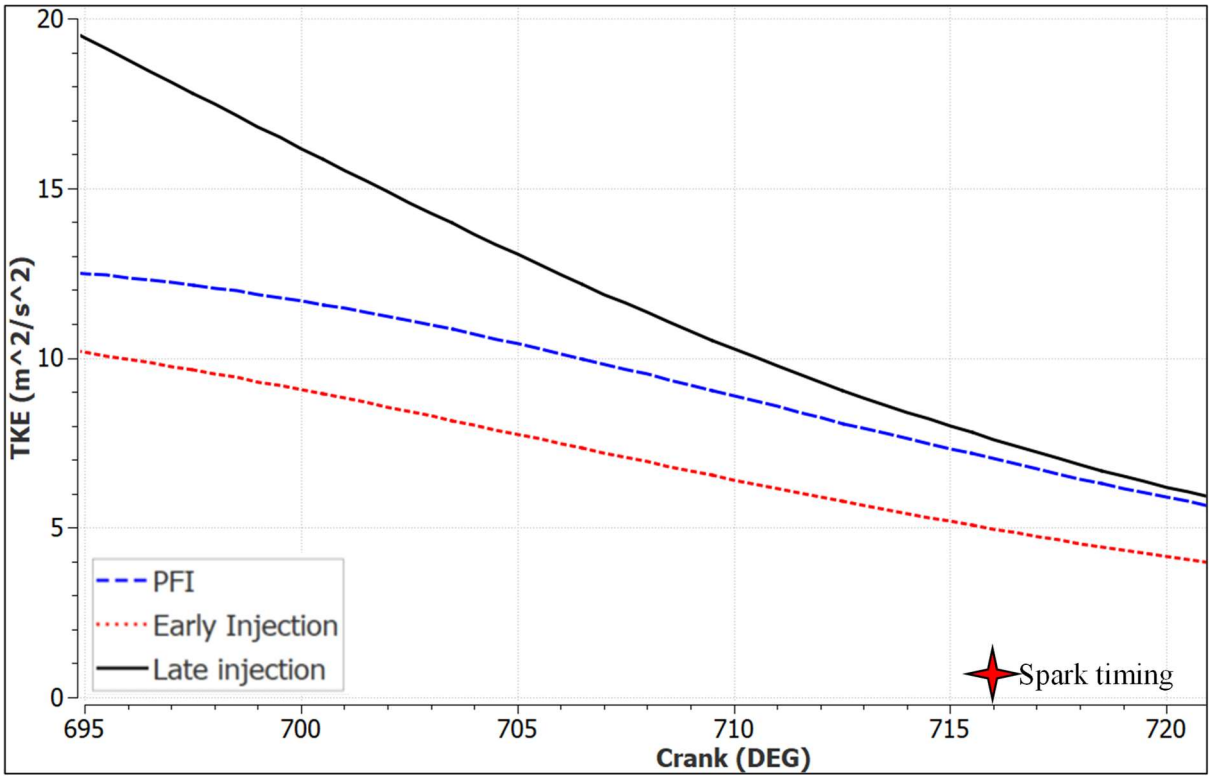

Figure 6.13: 1500 full load- Global Turbulent kinetic energy for PFI, Early and late injection events.

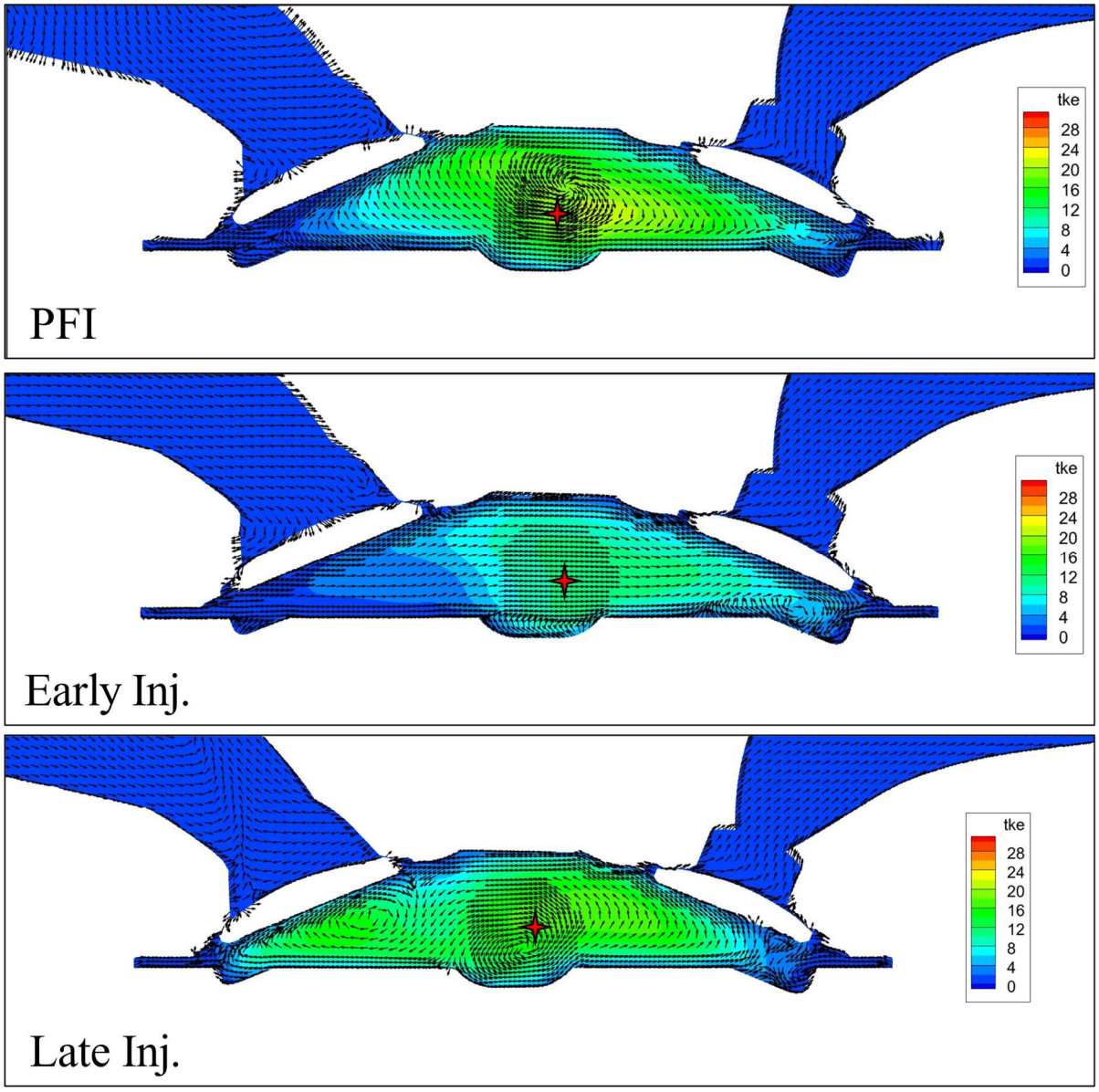

Figure 6.14: 1500 Full load: Turbulent kinetic energy distribution (in contour plots) and velocity vectors near spark location (indicated with star) for Early and Late injection in comparison with PFI case.

The impact of faster combustion can be noticed in figure 6.15 which shows in-cylinder pressure and heat release rate for all three cases. First, it can be noticed that Late injection has higher compression pressure in comparison to other cases which is due to volumetric efficiency achieved. The late injection has ≈10% more air inside the chamber compared to the other 2 cases. Whereas early injection and PFI achieved the same volumetric efficiency. These results are consistent with the literature [26], where experiments showed that injection during intake stroke restricts air to enter the combustion chamber in the same way as in the PFI case. Early

injection event has caused unfavourable condition for the combustion to progress resulting in lower pressure and much-delayed heat release compared to other 2 cases.

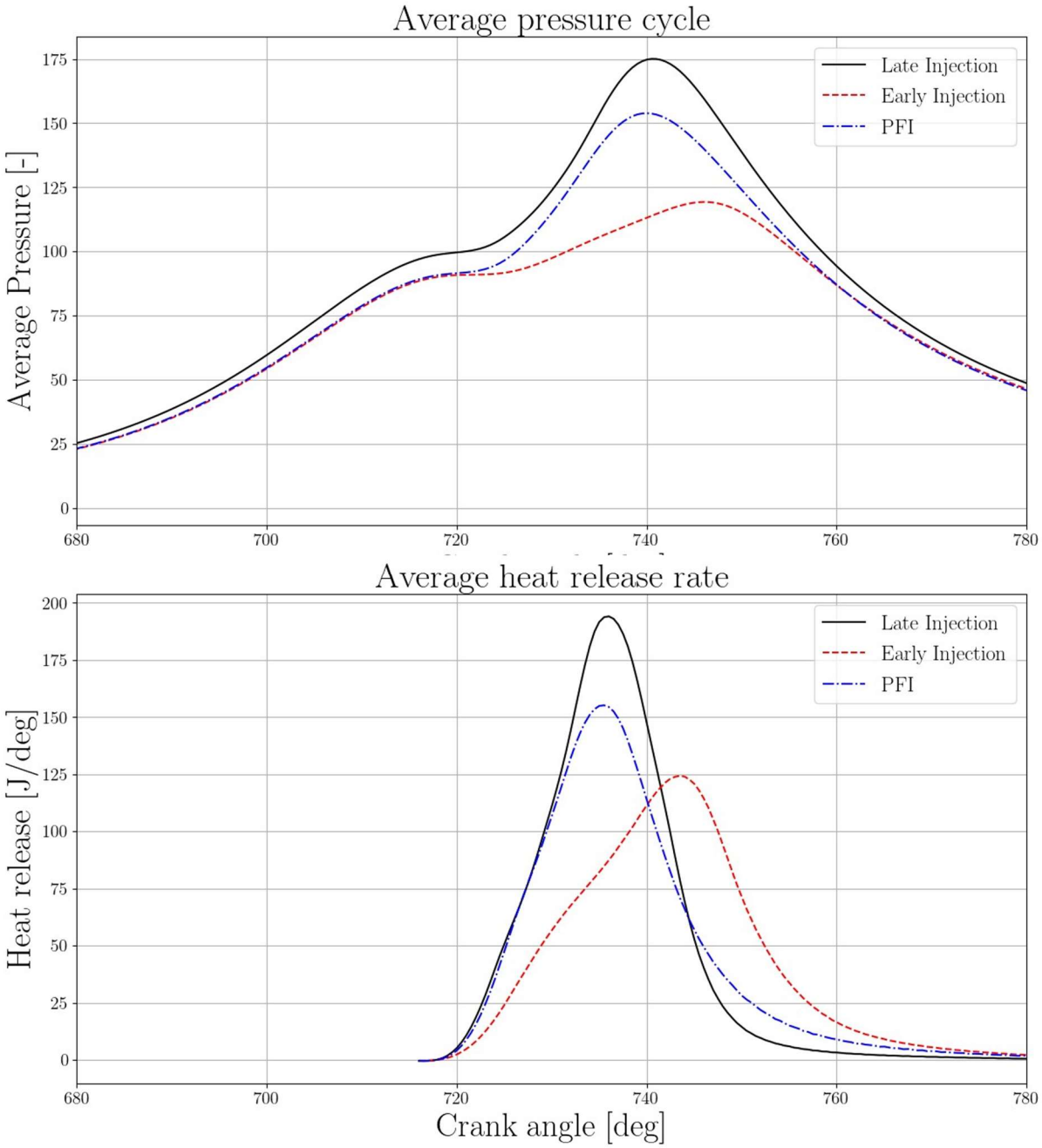

Figure 6.15: 1500 Full load: In-cylinder pressure and heat release rate for Early, Late injection in comparison to PFI case.

6.2. Impact of Late injection at high engine speeds- full load

The objective of this study was to determine the 'mixing breakdown' condition with Late injection at full load, that is, the engine speed at which there is a significant departure from mixture homogeneity due to lack of physical time available for mixing at full load conditions. The inhomogeneity in the mixture can cause instability in the combustion process and will lead to higher cyclic variations or misfiring. The procedure of the simulation campaign follows as:

1. The numerical model was calibrated against experiments available at 4500 rpm- 14 bar Imep at homogeneous conditions. The constant for flame stretch factor was adjusted due to full load conditions.
2. Late injection simulation was performed with new calibration at 4500 rpm.
3. The simulation campaign was extended with a new calibration setting to adjust for increasing engine speed for 5500-6500 rpm.

6.2.1 Model validation – 4500 rpm – 14 bar Imep

Figure 6.16 shows the average In-cylinder pressure and heat release rate comparison between experiments and numerical model. The average pressure curve between experiments and numerical are quite well matched.

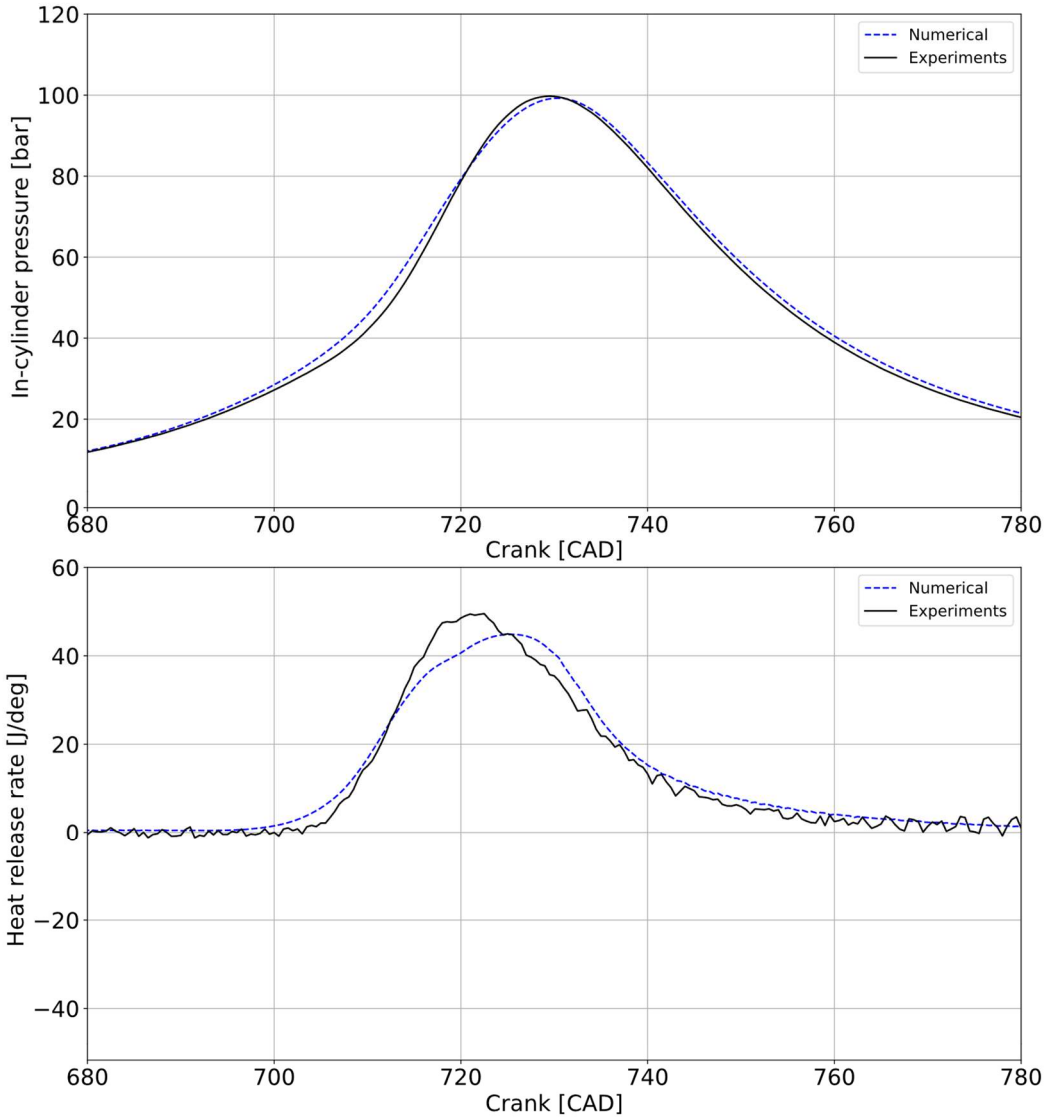

Figure 6.16: 4500 full load- Model validation - In-cylinder pressure and heat release rate comparison between experimental measurements and numerical prediction

6.2.2 Impact of Late injection on combustion at 4500 rpm-14 bar Imep (full load)

Simulations were performed with Late injection using the same numeric settings. Due to higher volumetric efficiency achieved with late injection, spark timing was optimized to keep MFB50 location within 728±2degCA. Figure 6.17 shows the combustion duration comparison between experiments performed in PFI mode (called Experiments), numerical at homogeneous conditions (called PFI) and numerical with Late injection (called Late injection). It can be noticed that with Late injection, faster combustion has been achieved. The difference of 8.8CA deg in combustion duration is significant and indicates similar behaviour noticed with 1500 full load case with Late injection. The main difference in combustion is in the theta50-90 phase, indicating an impact on flame quenching due to higher turbulence. It can be noticed that the heat release rate for Late injection has a peculiar phase (Figure 6.18 red curve detaches from PFI curve at TDC) where combustion is accelerated compared with PFI. The advantage of late injection in volumetric efficiency can be noticed with slightly higher pressure during the compression stroke. The injection jet significantly increased the turbulence level inside the combustion chamber noticeable in figure 6.19 which compares the global TKE between PFI and Late injection.

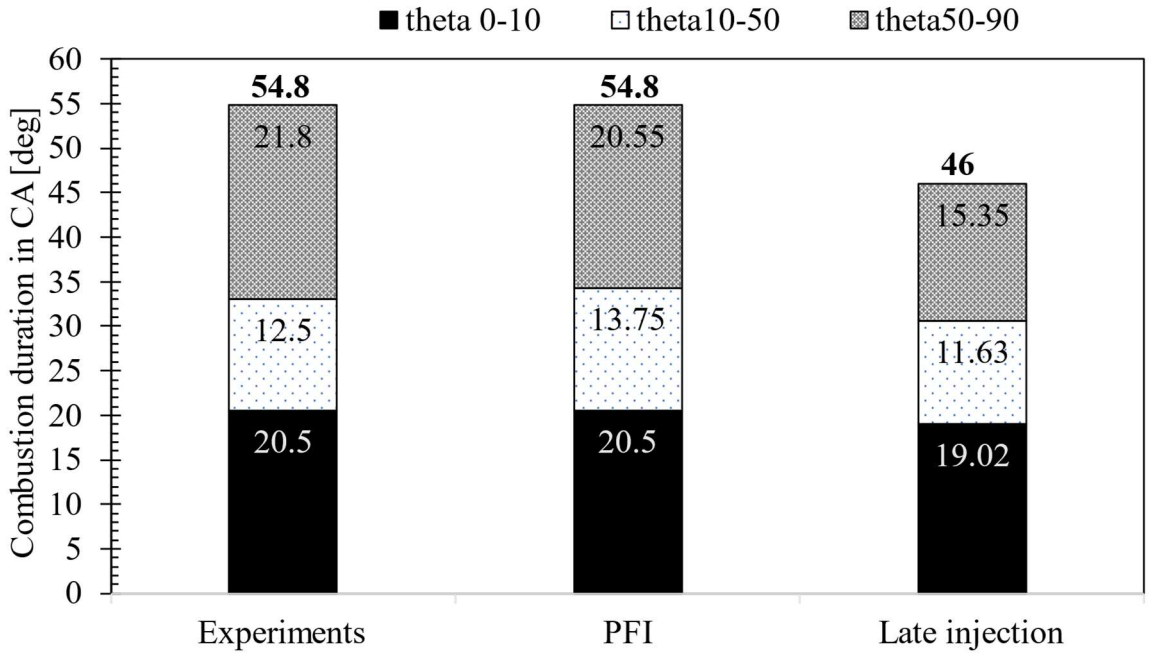

Figure 6.17: 4500 rpm – full load - Combustion duration comparison between experiments, PFI case and Late injection

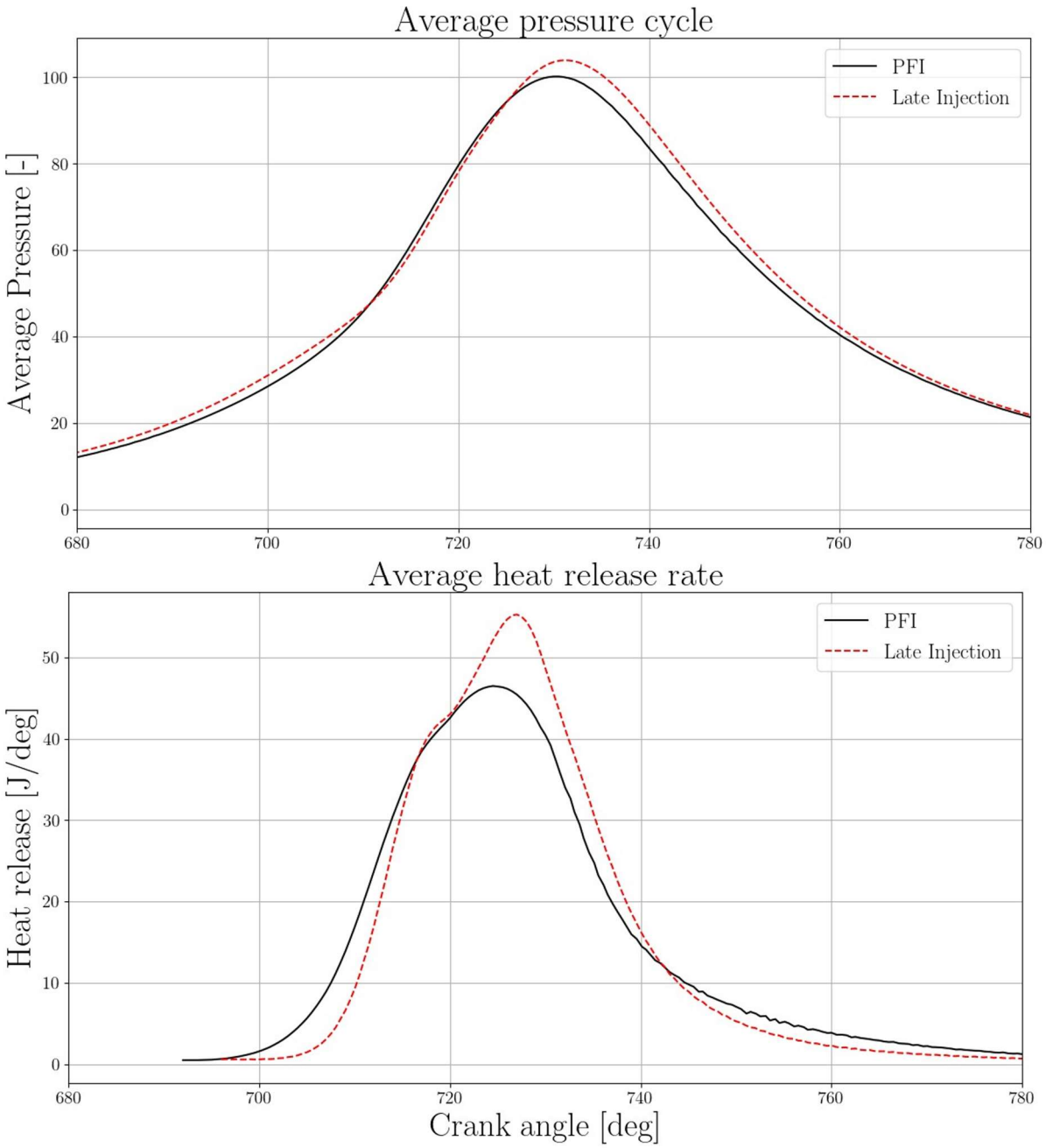

Figure 6.18: 4500 rpm – full load – In-cylinder pressure and heat release rate comparison between PFI and Late injection

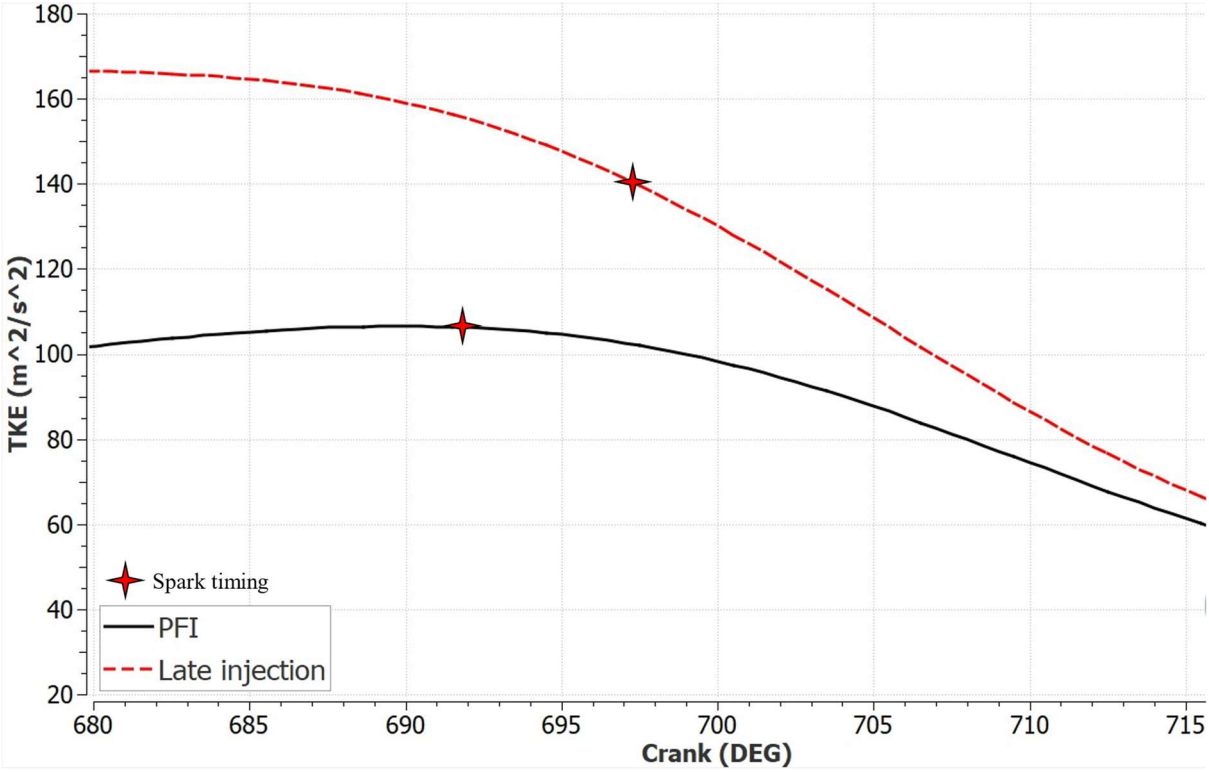

Figure 6.19: 4500 full load – Global turbulent kinetic energy

6.2.3 Impact of Late injection on mixture breakdown at high speeds- full loads

Starting from the numerical model validated in the last sub-section for 4500 engine rpm, simulations were extended for 5500 and 6500 rpm. Figure 6.20 shows the injection timings of late injection at different engine speeds. Injection timings were selected to maintain a global equivalence ratio equal to 1 and to keep the EOI before 90 CAD bTDC to give sufficient time for mixing. Spark timing was optimized to match the optimized combustion target of 728±2degCA.

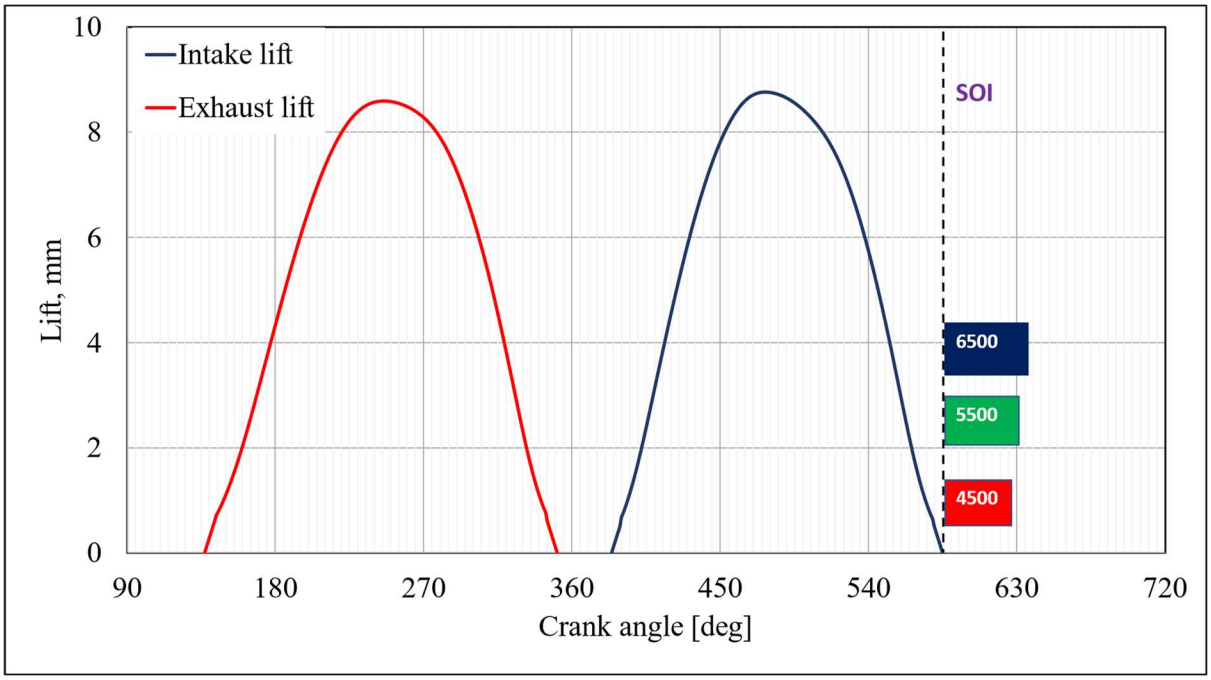

Figure 6.20: Valve lift profile as a function of crank angle. Late injection timings for three rpm's are indicated

Figure 6.21 shows non-dimensional parameters, CoV and FF for different engine speeds with squares representing spark timing for each case. It can be noticed that inhomogeneity in the mixture increases with increasing engine speed. For 1500 rpm, the flammable fraction reaches a value of 1 with a very low value of CoV (0.16) at spark timing. This means all the fuel inside the computational domain is within flammable limits (equivalence ratio = 0.7-1.7 for methane) with little to no cell-to-cell variation in fuel quantity. In the engine range of 4500-5500 rpm, 5500 rpm has slightly higher CoV compared to 4500 rpm suggesting that mixture heterogeneity is higher for 5500 rpm compared to 4500 rpm. Also, the flammable fraction reduced from 0.70 for 4500 rpm to 0.55 for 5500 rpm indicating a more stratified charge at 5500 rpm. In the case of 6500 rpm, the flammable fraction is below 0.4 with a CoV value close to 0.9. This helps to reach an understanding that mixture formation at high engine speeds is highly dependent on the physical time available for mixture formation.

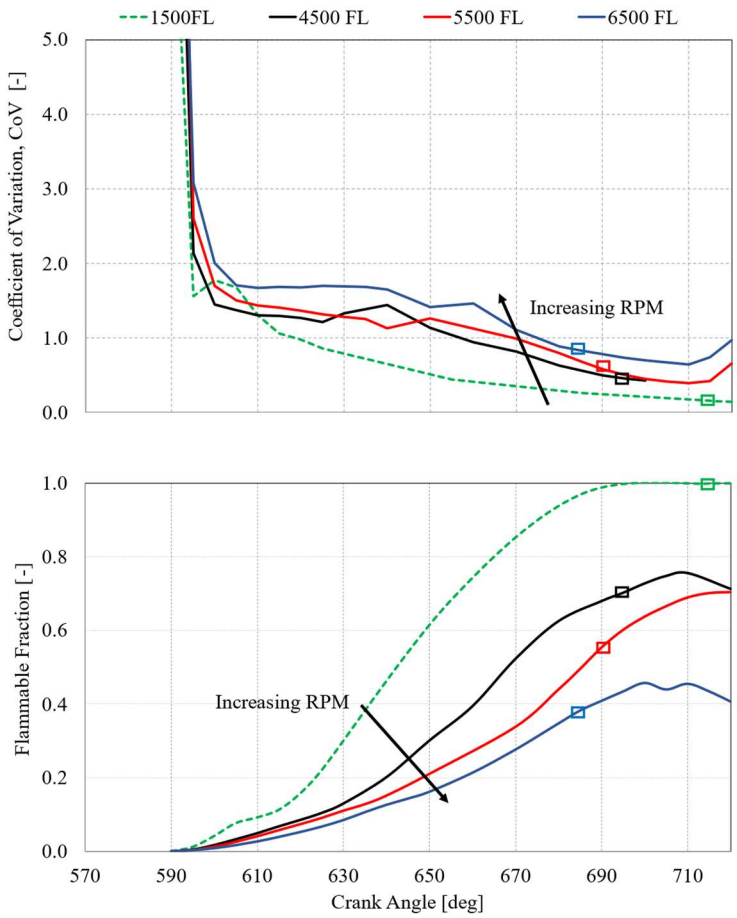

Figure 6.21: Coefficient of variation, CoV (top) and Flammable fraction (bottom) for different engine speeds at full load – as a function of crank angle [deg]

This can also be noticed from fuel mass distribution at spark advance location in Figure 6.22. At 4500 rpm, 31% of the fuel mass is within 0.9-1.1 equivalence ratio whereas this fraction reduces to 20% for 5500 and 14% for 6500 rpm. It can be noticed that for 4500 rpm, most fuel is still within flammable limits. For 6500 rpm, high fuel stratification can be observed as some fuel is in the rich zone (peak at equivalence ratio=1) while some in the lean zone (another peak around 0.1-0.4).

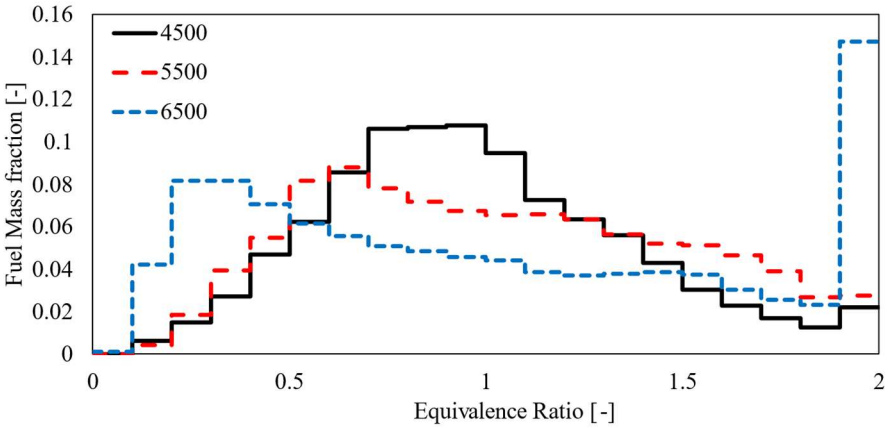

Figure 6.22: Mixture breakdown – fuel mass fraction distribution at spark timing for early and late injection events.

6.2.4 Impact of Mixture breakdown on combustion

Figure 6.23 shows the impact of mixture breakdown on heat release rate for three engine speeds. For 4500 and 5500 rpm, the heat release rate is quite similar with some distinction due to earlier spark timing. In both cases, combustion has accelerated around TDC which leads to an equivalent theta10-50 burn duration (presented in figure 6.24). Whereas for 6500 rpm, the heat release rate has a trough. This could be due to high mixture stratification in the chamber. Combustion starts in the flammable region near the spark plug but is slowed down as it encounters an either too rich or too lean region of the mixture. It can be noticed that the flame development phase (theta 0-10) has the most impact due to high mixture inhomogeneity which increased by 9.5deg CA from 4500 to 6500 rpm. This gives evidence that combustion above 5500 rpm would be highly inconsistent and would lead to higher cyclic variations. This result has been confirmed by experimental tests where higher combustion irregularity was detected at speeds above 4500 rpm [133].

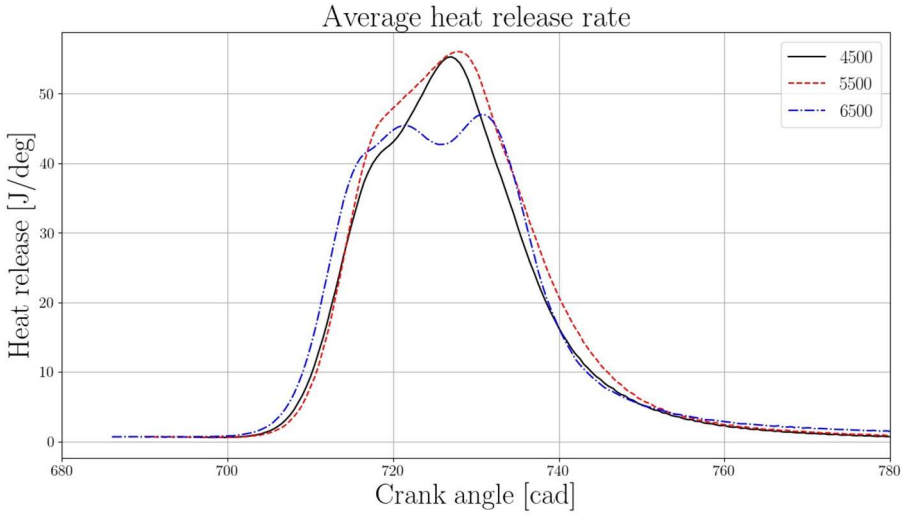

Figure 6.23: Heat release rate at high engine speeds.

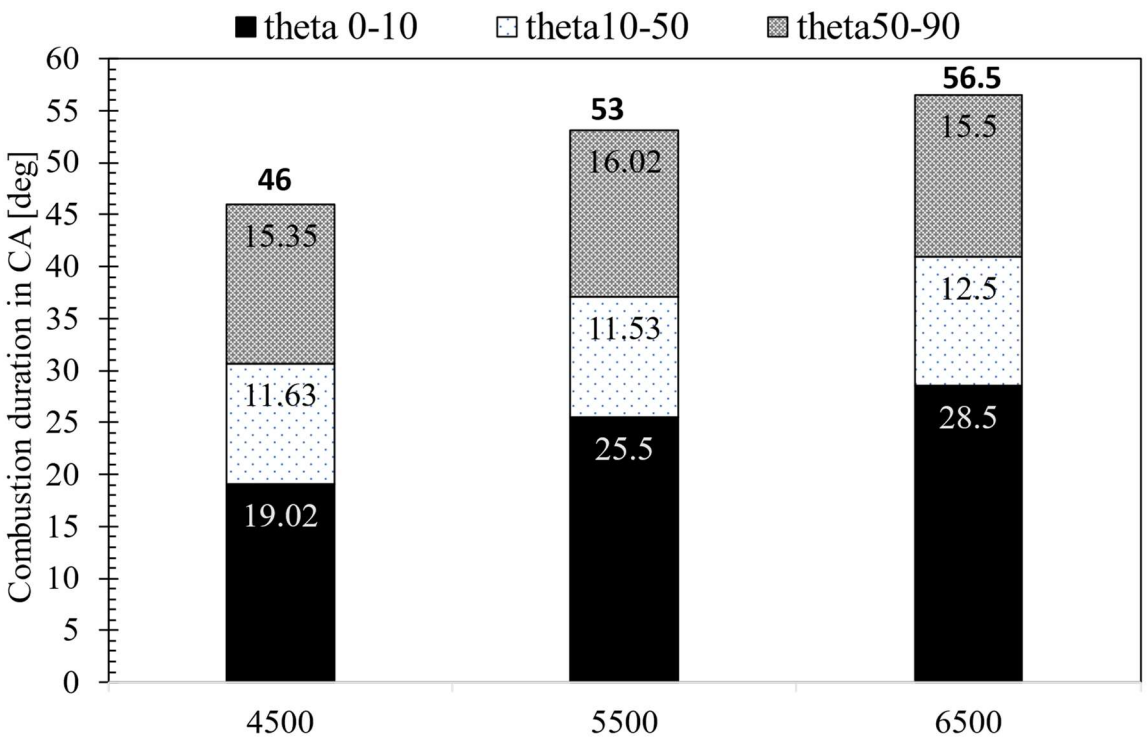

Figure 6.24: Combustion duration comparison between engine speed range 4500-6500 with late injection timing

6.3. Impact of injection timing at low-speed, low load (1500 rpm – 3bar Imep)

To verify the trade-off between mixing degree and turbulence levels with different injection timings at part load, simulations were performed with early injection timing and late injection timing and compared with the PFI case. With the early injection, the same volumetric efficiency was observed as PFI because in both cases fuel replaces some of the incoming air and thus similarly affects the volumetric efficiency. With late injection timing, 8.4 % higher volumetric efficiency has been achieved, leading to higher trapped mass inside the chamber with respect to early injection or PFI case which is consistent with results in the literature [21]. Its direct impact can be observed in in-cylinder pressure during the compression phase where

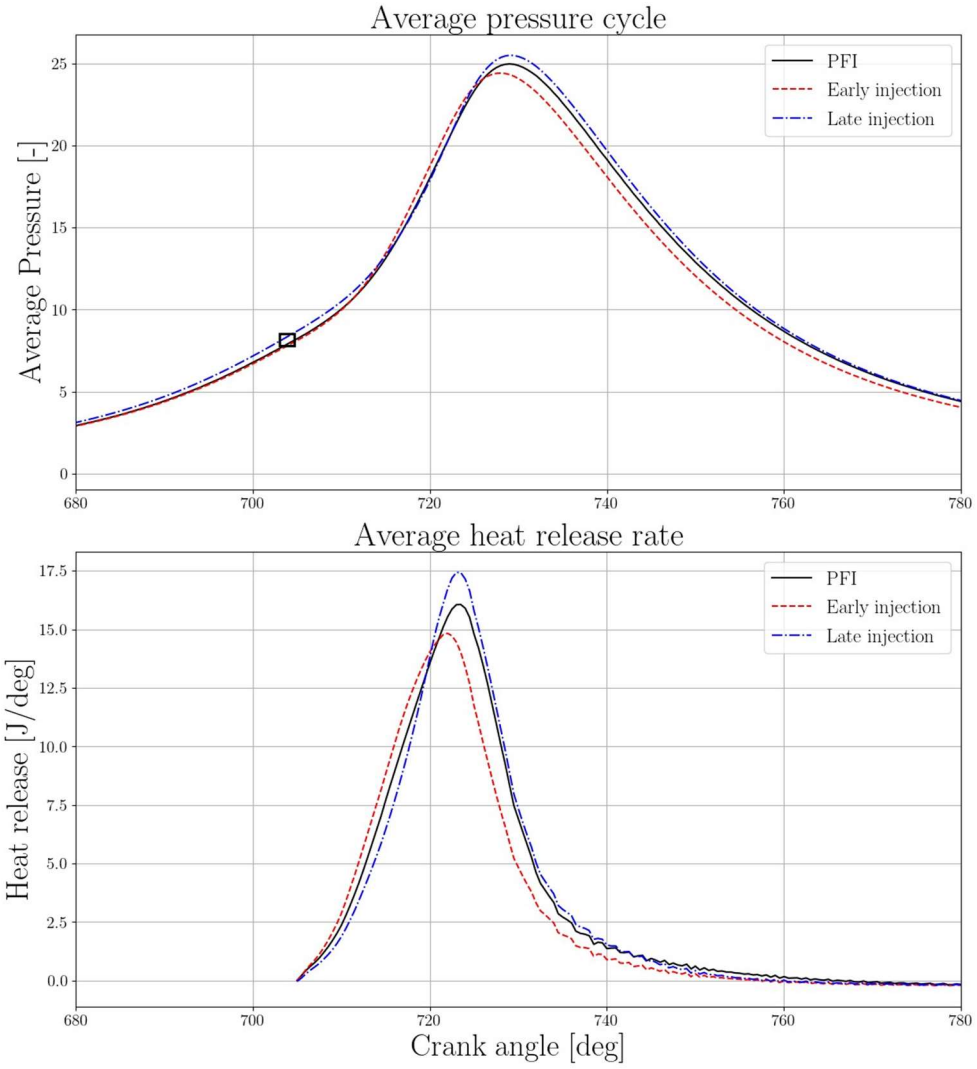

Figure 6.25: 1500 rpm / 3bar Imep - In-cylinder pressure and heat release rate of early injection, late injection compared with PFI case

late injection has slightly higher pressure compared to the other two cases (figure 6.25, black square represents spark timing).

In the case of early injection, injection jet impinges on the piston accumulating fuel on the piston. With EOI, the tumble ratio recovers quickly as more air enters the cylinder. This tumble motion moves the plumes with it, increasing mixing which can be seen in the rapid increase in flammable fraction between 470-500deg CA (figure 6.26). With piston movement towards TDC (after 540 deg CA), some fuel leaves the computational domain and enters the intake port before IVC. This can be seen as flammable fraction (FF) drops from 1.1 to 1.0. With FF= 1.1, there was more fuel in the computational domain before 560deg CA than the final trapped fuel mass.

In the case of late injection, fuel mixing is rapid is driven by piston movement. CoV in late injection is higher compared to early injection case indicating more mixture heterogeneity in the chamber at spark timing. With both injection timings, all mixture is in the flammable limits (FF=1) at spark timing (indicated by squares).

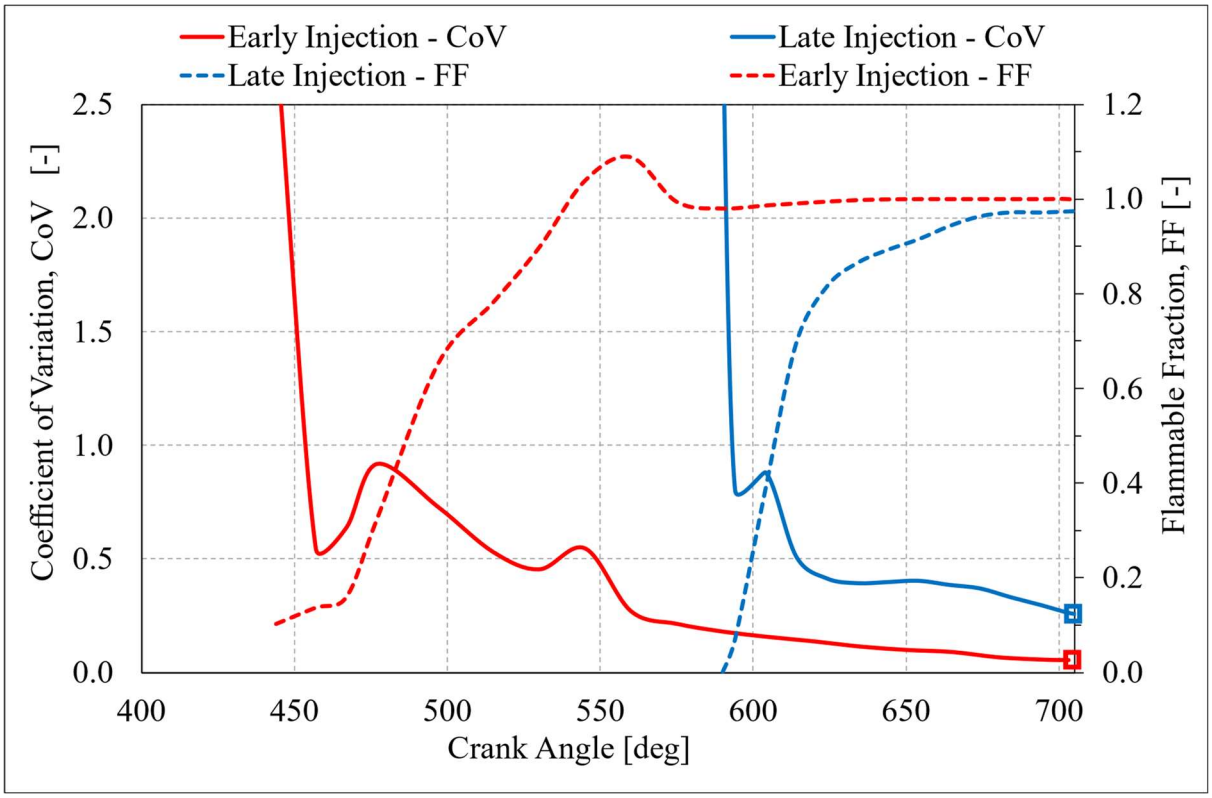

Figure 6.26: 1500 rpm / 3bar Imep – Coefficient of variation, CoV and flammable fraction, FF for early and late injection

Figure 6.27 shows the tumble ratio along Y-axis for early injection and late injection and is compared with the PFI case. It can be noticed that during both injection events, the tumble ratio is reversed due to interaction with the injector jet

CoV at spark advance in case of late injection (0.25) is higher than early injection case (0.06). This indicates that the mixture in late injection has heterogenous at spark advance. This can be confirmed from figure 6.28, showing fuel mass fraction as a function of equivalence ratio at spark timing. In the case of early injection, ≈98% of total fuel mass is within 0.9-1.1 equivalence ratio indicating good mixing whereas in the case of late injection, only 36% of total fuel mass is in between 0.9-1.1 equivalence range.

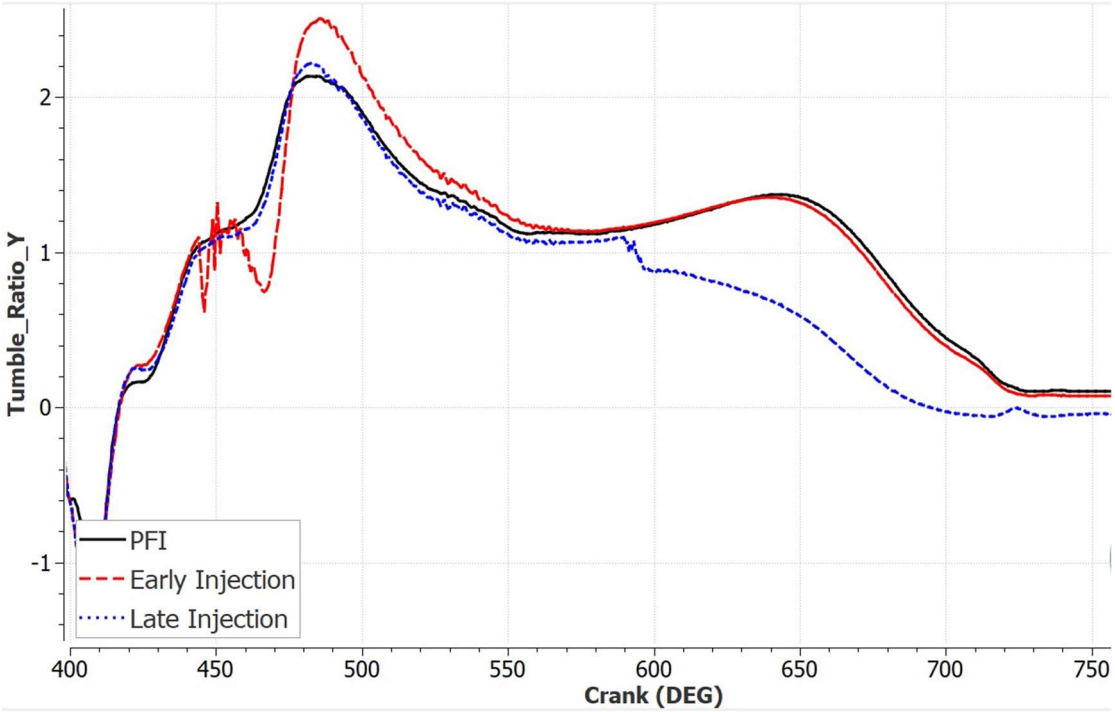

Figure 6.27: 1500 rpm / 3bar Imep – Tumble ratio of early injection and late injection compared with PFI case.

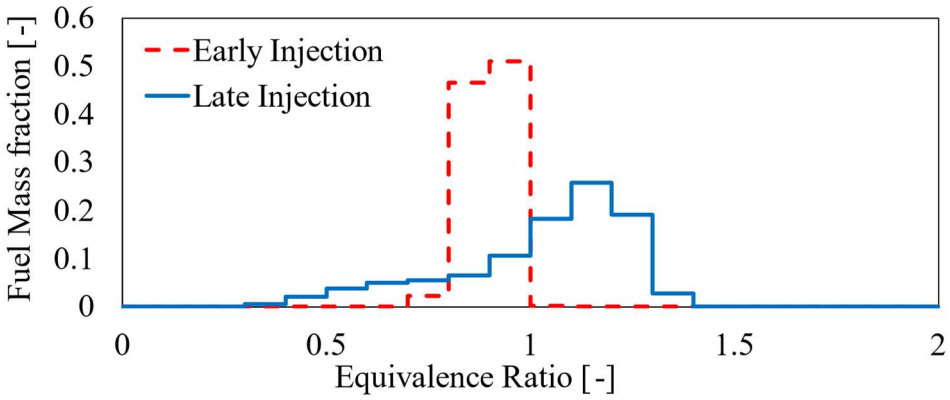

Figure 6.28: 1500 rpm / 3bar Imep – Fuel mass fraction as a function of equivalence ratio of early injection and late injection at spark timing

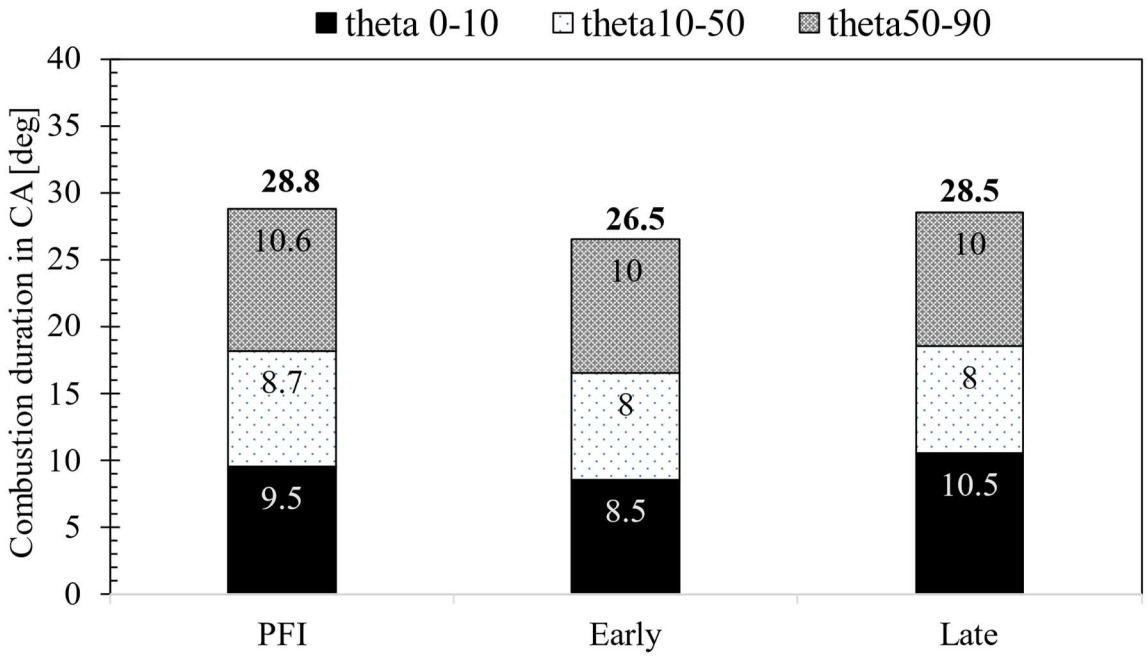

Figure 6.29: 1500 rpm / 3bar Imep – Combustion duration for PFI, early and late injection timings

Figure 6.29 shows the impact of injection timings on combustion duration. Combustion duration of late injection is similar to PFI case whereas early injection combustion is faster by 2.3deg CA. this can be explained as the early injection case has higher TKE at spark timing compared to the other two cases (figure6.29). This is contrary to what was found in the full load case. With a shorter injection duration, an early injection event gives enough time for the tumble to recover. This would result in favourable TKE at spark timing conditions and can result in faster combustion.

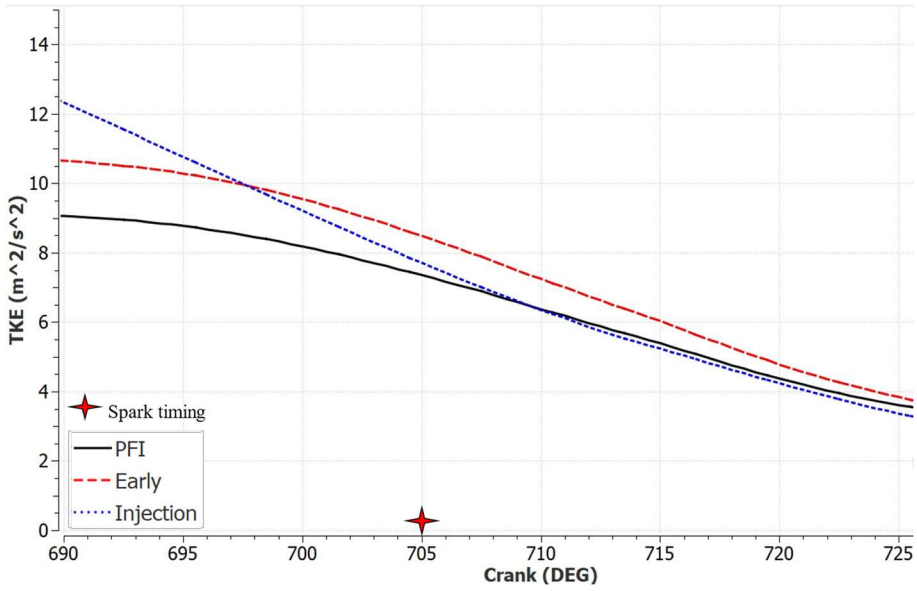

Figure 6.30: 1500 rpm / 3bar Imep – Global TKE comparison between Early injection, late injection, and PFI case.

6.4 Summary

In this section, early and late injection timings at different engine operating conditions were numerically evaluated and compared with PFI mode. The numerical model was validated with available PFI experiments. The model was used to evaluate the impact of injection timing on charge motion, volumetric efficiency, mixture formation and combustion with a centrally mounted injector.

- At 1500rpm – full load, DI impacted the tumble motion cause its decay due to the injector jet. This also had an impact on the mixture formation process. The mixture in DI is mostly driven due to the interaction of the injector jet with piston and cylinder walls. Volumetric efficiency in early injection was found to be the same as PFI whereas a 10% improvement in late injection was observed.
    - Early injection allows enough time to form a homogeneous mixture. However, in-cylinder turbulence is negatively impacted due to injector jet and tumble interaction which causes poor combustion performance in comparison to PFI.
    - The late injection has faster combustion even though high mixture heterogeneity was observed due to limited time available for mixing. This was due to favourable turbulence structure observed near spark plug location during spark timing. Higher turbulences also resulted in lower flame quenching in last part of combustion.
- At full load conditions and high engine speeds, mixture heterogeneity was confirmed with late injection timing. Even though high TKE can be achieved at high engine speeds, it doesn't help in faster mixture formation. Physical time available for mixing is still a limit. It was found that above 5500rpm, combustion was highly impacted due to mixture heterogeneity.
- At 1500 rpm / 3 bar Imep, Early injection performed better for combustion even though lower volumetric efficiency was achieved in this case. It was observed that with a short injection duration (low/part load cases), the tumble motion recovers in the last stage of intake. Turbulence from injector jet also assists in-cylinder turbulence resulting in higher TKE at spark timings. Combustion duration in late injection, however, was comparable to the PFI system. Mixture formation in both cases reached a flammable range with high heterogeneity with late injection.

Chapter 7:

Conclusions and Recommendations

Conclusions

The present work aimed at contributing to the development of high-performance natural gas engines through the evaluation of charge dilution with EGR, hydrogen doping, and evaluation of a centrally mounted direct injector system. The objectives of this work were to numerically assess:

- The impact of high intake turbulence on EGR dilution limits achieved through the optimization of the cylinder head
- Quantification of EGR dilution tolerance at low, medium, and full engine loads
- Impact of EGR dilution on combustion
- Impact of hydrogen addition on EGR dilution tolerance
- Effects of direct injection timing on mixture homogeneity and combustion at low-end engine speeds, full loads
- Quantification of mixture breakdown limits with late injection timing at high engine speeds, full loads
- Effects of injection timing on low-load case especially at low-end torque range

To achieve these objectives, a numerical model was developed and was validated for available experimental data. The model was used as a virtual test bench and allowed to draw the conclusions, which are summarized hereafter: -

- Through the analysis performed in section 4.2, it was shown that an increase in intake tumble, due to the new cylinder head design, was effective in increasing the EGR dilution limits of the engine. The high tumble breaks down during compression converting into high turbulent kinetic energy (TKE) that is available at spark timing event. It helped in increasing the combustion speeds at high EGR rates. It was found that 'new engine design' was able to effectively burn 10% more EGR than a conventional 'Low turbulence engine' design at 8bar Imep.

- In sections 4.3 & 4.4, it was found that the EGR tolerance of an engine is highly dependent on the overall (external plus internal) EGR fraction inside the cylinder and this fraction remains constant at different loads. For this engine, the overall EGR limit was found to be between 30-31% irrespective of the engine load (evaluated at a constant engine speed of 2000 rpm).

- Within EGR dilution limits, an increase in external LP-EGR would increase in-cylinder pressures which would cause intense blowdown at EVO resulting in lower internal EGR fractions. A similar gas exchange process was also observed with the increase in engine loads.

- The dilution tolerance of an NG engine can be increased by hydrogen addition into the fuel. The results showed that a 15% increase in hydrogen fraction (by vol) in fuel increased EGR tolerance limits by 5% and is consistent with the finding in the literature [132].

- The simulations also showed that hydrogen addition impacts the flame development period of the combustion. The shorter theta0-10 duration resulted in higher EGR tolerance as well and is found to have traded well with literature sources [43,122,130,131].

- In Chapter 6, it was found that early injection has similar volumetric efficiency as that of the PFI system whereas late injection helped to achieve higher volumetric efficiency and was coherent with literature sources [26].

- In section 6.1, for 1500 rpm-full load, it was also found that early injection timing was optimum for mixture homogeneity with the centrally mounted injector. Mixture formation in this type of injector is due to the interaction of the injector jet with piston and cylinder walls and is dependent on the physical time available for mixing. Other factors such as piston motion, its direction, and intake air flow also contribute to mixture formation. However, the charge motion of the gaseous injection event was better preserved for late injection that led to a faster combustion compared to early injection.

- In section 6.2, it was shown that an increase in engine speed resulted in an increase in mixture heterogeneity due to a lack of mixing time. It was found that combustion at an engine speed above 5500rpm was highly impacted due to excessive mixture stratification.

- In section 6.3, at 1500 rpm / 3bar Imep, it was found that early injection was optimum for mixture formation and combustion duration. It was observed that a shorter injection duration allowed sufficient time for mixing. Furthermore, after the end of injection, tumble motion recovery was observed that resulted in higher TKE at spark timing which reduced the combustion duration. Combustion duration in late injection, however, was comparable to the PFI system. Mixture formation in both cases reached a flammable range with high heterogeneity in the late injection event.

Recommendations

- The simulations were performed in which fuel was injected in one continuous injection event. One possible method of optimizing the mixture formation and combustion duration can be to perform multiple injection events. In this work, it was observed that early injection helped to improve mixture homogeneity and a late injection helped to improve TKE near the spark region. Similar results were also found in the literature source [15]

- The optimal injection timing with the DI injector improves the cylinder TKE. This can be helpful to further improve the EGR dilution tolerances with DI. Literature showed that optimal injection timing helped improve EGR dilution tolerance [43]

- The centrally mounted injector sits at the top of the roof. Literature has shown that this type of injector orientation is not optimal for preserving cylinder charge motion. Realigning the injector orientation such that it assists tumble motion can potentially improve the mixture formation and can complement overall tumble motion [43,136]

Possible improvements in numerical model

Numerical models used in this work performed well to achieve the project objectives. However, suggestions to improve the models are mentioned below:

- As discussed in section 3.2, description of flamelet assumption invalidates at Ka > 1. In high turbulence internal combustion engine with high EGR dilution, combustion sometimes takes place in pocket regime. Improvements in ECFM model to accommodate pocketed combustion regime can be studied further.

- It was observed that model can be improved in terms of emission prediction especially for CO and NOx. Possible integration of detailed chemistry solver with ECFM can help improve the emission prediction (in burned gas zones as well). This should be kept in mind that this integration will increase the computational cost significantly.

Appendix I

Stretch factor calibration values used in this work at different engine speeds and Imep's are reported in table below.

Imep [bar]	Engine speed [RPM]	Stretch factor [-]
3	1500 2000 3000	2.7
8	2000 3000	1.7
30	1500 2000	0.8

Bibliography

[1] https://www.metoffice.gov.uk/hadobs/hadcrut4/index.html

[2] Morice, C.P., Kennedy, J.J., Rayner, N.A. and Jones, P.D., 2012. Quantifying uncertainties in global and regional temperature change using an ensemble of observational estimates: The HadCRUT4 data set. *Journal of Geophysical Research: Atmospheres*, *117*(D8).

[3] https://ourworldindata.org/co2-and-other-greenhouse-gas-emissions

[4] Bereiter, B., Eggleston, S., Schmitt, J., Nehrbass-Ahles, C., Stocker, T.F., Fischer, H., Kipfstuhl, S. and Chappellaz, J., 2015. Revision of the EPICA Dome C CO2 record from 800 to 600 kyr before present. *Geophysical Research Letters*, *42*(2), pp.542-549.

[5] IPCC, 2014: *Climate Change 2014: Synthesis Report. Contribution of Working Groups I, II and III to the Fifth Assessment Report of the Intergovernmental Panel on Climate Change* [Core Writing Team, R.K. Pachauri and L.A. Meyer (eds.)]. IPCC, Geneva, Switzerland, 151.

[6] Jouzel, J., Masson-Delmotte, V., Cattani, O., Dreyfus, G., Falourd, S., Hoffmann, G., Minster, B., Nouet, J., Barnola, J.M., Chappellaz, J. and Fischer, H., 2007. Orbital and millennial Antarctic climate variability over the past 800,000 years. *science*, *317*(5839), pp.793-796.

[7] Lüthi, D., Le Floch, M., Bereiter, B., Blunier, T., Barnola, J.M., Siegenthaler, U., Raynaud, D., Jouzel, J., Fischer, H., Kawamura, K. and Stocker, T.F., 2008. High-resolution carbon dioxide concentration record 650,000–800,000 years before present. *nature*, *453*(7193), pp.379-382.

[8] Agreement, P., 2015, December. Paris agreement. In *Report of the Conference of the Parties to the United Nations Framework Convention on Climate Change (21st Session, 2015: Paris). Retrived December* (Vol. 4, p. 2017).

[9] European Environment Agency. *National policies and measures on climate change mitigation in Europe 2017.* 2018. ISBN 978-92-9480-002-2, doi: 10.2800/74986

[10] “fuel for thought: The First Natural Gas Vehicles” http://blog.westport.com/2012/04/first-natural-gas-vehicles.html

[11] Weber, C., Kramer, U., Klein, R., “CNG-Specific Downsizing -Potentials and Challenges”, Internationales Wiener Motorensymposium 2015.

[12] Verhelst, S., and Wallner, T., 2009 “Hydrogen-fueled internal combustion engines,” Progress in Energy and Combustion Science, vol. 35, pp. 490-527

[13] VDI, Wärmeatlas, Berlin Heidelberg New York: Springer Verlag, 2006.

[14] Edwards, R., Larive, J.F., Rickeard, D. and Weindorf, W., 2013. Well-to-Tank Version 4 JEC Well-to-Wheels Analysis. *European Commission Joint Research Center: Brussels, Belgium*, p.134.

[15] Edwards, R., Larivé, J.F. and Beziat, J.C., 2011. Well-to-wheels analysis of future automotive fuels and powertrains in the European context. *JRC, CONCAWE and Renault/EUCAR*, *74*.

[16] Wang-Helmreich, H. and Lochner, S., 2012. The potential of natural gas as a bridging technology in low-emission road transportation in Germany. *Thermal Science*, *16*(3), pp.729-746.

[17] Heywood, J.B., 2018. *Internal combustion engine fundamentals*. McGraw-Hill Education.

[18] Jahirul MI, Masjuki HH, Saidur R, Kalam MA, Jayed MH and Wazed MA. Comparative engine performance and emission analysis of CNG and gasoline in a retrofitted car engine. *Appl Therm Eng* 30(4):2219-26, 2010

[19] Kato, K., Igarashi, K., Masuda, M., Otsubo, K., Yasuda, A., Takeda, K. and Sato, T., 1999. Development of engine for natural gas vehicle. *SAE transactions*, pp.939-947.

[20] Anderson, J., Miers, S., Wallner, T., Stutenberg, K. et al., "Performance and Efficiency Assessment of a Production CNG Vehicle Compared to Its Gasoline Counterpart," SAE Technical Paper 2014-01-2694, 2014, doi:10.4271/2014-01-2694.

[21] Husted, H., Karl, G., Schilling, S. and Weber, C., 2014, October. Direct injection of CNG for driving performance with low CO2. In *23rd Aachen colloquium automobile and engine technology* (pp. 829-850).

[22] Hofmann, P., Hofherr, T., Hoffmann, G. and Preuhs, J.F., 2016. Potential of CNG direct injection for downsizing engines. *MTZ worldwide*, *77*(7), pp.28-35.

[23] Duc-Khanh Nguyen, James Szybist, Louis Sileghem, Sebastian Verhelst, Effects of molar expansion ratio of fuels on engine efficiency, Fuel, Volume 263, 2020, 116743, ISSN 0016-2361, https://doi.org/10.1016/j.fuel.2019.116743.

[24] Szybist, J.P., Chakravathy, K. and Daw, C.S., 2012. Analysis of the impact of selected fuel thermochemical properties on internal combustion engine efficiency. *Energy & Fuels*, *26*(5), pp.2798-2810.

[25] Nguyen, D.K., Sileghem, L. and Verhelst, S., 2019. Exploring the potential of reformed-exhaust gas recirculation (R-EGR) for increased efficiency of methanol fueled SI engines. *Fuel*, *236*, pp.778-791.

[26] Song, J., Choi, M. and Park, S., 2017. Comparisons of the volumetric efficiency and combustion characteristics between CNG-DI and CNG-PFI engines. *Applied Thermal Engineering*, *121*, pp.595-603.

[27] Kuroda, H., Nakajima, Y., Sugihara, K., Takagi, Y. and Muranaka, S., 1978. The fast burn with heavy EGR, new approach for low NO x and improved fuel economy. *SAE Transactions*, pp.1-15.

[28] Nakajima, Y., Sugihara, K., Takagi, Y. and Muranaka, S., 1981. Effects of exhaust gas recirculation on fuel consumption. *Proceedings of the Institution of Mechanical Engineers*, *195*(1), pp.369-376.

[29] Neame, G.R., Gardiner, D.P., Mallory, R.W., Rao, V.K., Bardon, M.F. and Battista, V., 1995. Improving the fuel economy of stoichiometrically fuelled SI engines by means of EGR and enhanced ignition-a comparison of gasoline, methanol and natural gas. *SAE transactions*, pp.1062-1076.

[30] Ryan, T. and Lestz, S., 'The Laminar Burning Velocity of Isooctane, N-Heptane, Methanol, Methane and Propane at Elevated Temperatures and Pressures in the Presence of Diluent," SAE Paper #800103, Society of Automotive Engineers, Warrendale, PA, 1980.

[31] Alger, T., Gingrich, J. and Mangold, B., 2007. *The effect of hydrogen enrichment on EGR tolerance in spark ignited engines* (No. 2007-01-0475). SAE Technical Paper.

[32] J. Wallace , A. Cattelan , Hythane and CNG fuelled engine exhaust emission compar- ison, Hydrogen Energy Prog. 3 (1994) 1761

[33] A. Gharehghani , R. Hosseini , M. Mirsalim , T.F. Yusaf , A computational study of operating range extension in a natural gas SI engine with the use of hydrogen, Int. J. Hydrogen Energy 40 (17) (2015) 5966–5975 .

[34] S.O. Akansu , Z. Dulger , N. Kahraman , T.N. Veziro ğlu , Internal combustion engines fueled by natural gas - Hydrogen mixtures, Int. J. Hydrogen Energy 29 (14) (2004) 1527–1539 .

[35] C.G. Bauer , T.W. Forest , Effect of hydrogen addition on the performance of methane–fueled vehicles. Part I: effect on S.I. engine performance, Int. J. Hydrogen Energy 26 (1) (2001) 55–70

[36] Pamminger, M., Wallner, T., Sevik, J., Scarcelli, R., Hall, C., Wooldridge, S. and Boyer, B., 2016, October. Performance, Efficiency and Emissions Evaluation of Gasoline Port-Fuel Injection, Natural Gas Direct Injection and Blended Operation. In *Internal Combustion Engine Division Fall Technical Conference* (Vol. 50503, p. V001T03A008). American Society of Mechanical Engineers.

[37] Sevik, J., Pamminger, M., Wallner, T., Scarcelli, R., Boyer, B., Wooldridge, S., Hall, C. and Miers, S., 2016. Influence of injector location on part-load performance characteristics of natural gas direct-injection in a spark ignition engine. *SAE International Journal of Engines*, *9*(4), pp.2262-2271.

[38] Lucas, G., Tallu, G. and WEIßNER, M., 2018, September. CFD-based development of an ignition chamber for a lean and high efficient CNG combustion. In *THIESEL 2018 Conf. Thermo-Fluid Dyn. Process*.

[39] SHIGA, S., ARAKI, M., OBOKATA, T., HUANG, Z., ISHII, H., Takamasa, U.E.D.A., Mitsuhiro, T.S.U.E. and Michikata, K.O.N.O., 2005. *Basic aspect of combustion of CNG incylinder direct injection with spark-ignition* (No. 2005-26-352). SAE Technical Paper.

[40] Iyer, C.O. and Yi, J., 2009. *3D CFD upfront optimization of the in-cylinder flow of the 3.5 L V6 EcoBoost engine* (No. 2009-01-1492). SAE Technical Paper.

[41] Rapetto, N. *A COMPREHENSIVE ANALYSIS OF NATURAL GAS DIRECT INJECTION AND OF MIXTURE FORMATION IN SPARK IGNITION ENGINES* (Doctoral dissertation, Ph. D. thesis, Politecnico di Torino, Politecnico di Torino).

[42] Viglione, L., 2017. Analysis of injection, mixture formation and combustion processes for innovative CNG Engines (Doctoral dissertation, Ph. D. thesis, Politecnico di Torino, Politecnico di Torino).

[43] Sevik Jr, J.M., 2017. *Impact of Natural Gas Direct Injection on Thermal Efficiency in a Spark Ignition Engine* (Doctoral dissertation, Michigan Technological University).

[44] Xu, J., 2018. Numerical and Experimental Analysis of Fuel Injection and Mixture Formation in High-Performance Natural Gas Engines: methodologies and Applications (Doctoral dissertation, Ph. D. thesis, Politecnico di Torino, Politecnico di Torino).

[45] Douailler, B., Ravet, F., Delpech, V., Soleri, D. et al., "Direct Injection of CNG on High Compression Ratio Spark Ignition Engine: Numerical and Experimental Investigation," SAE Technical Paper 2011-01-0923, 2011, doi:10.4271/2011-01-0923.

[46] http://www.gason.eu/

[47] Rouleau, L., Serrano, D., Lecointe, B., Ravet, F., Coma, G. and Christou, P., 2017, October. CNG direct injection spark-ignition engine with high turbulence and high compression ratio: numerical and experimental investigations. In *12th Conference of Gaseous-Fuel Powered Vehicles*.

[48] Wheeler, J., Polovina, D., Ramanathan, S., Roth, K., Manning, D. and Stein, J., 2013. *Increasing EGR Tolerance using High Tumble in a Modern GTDI Engine for Improved Low-Speed Performance* (No. 2013-01-1123). SAE Technical Paper.

[49] Poinsot, T., Veynante, D., "Theoretical and Numerical Combustion," Edwards, 2005.

[50] Pomraning, E., Richards, K. and Senecal, P.K., 2014. Modeling turbulent combustion using a RANS model, detailed chemistry, and adaptive mesh refinement (No. 2014-01-1116). SAE Technical Paper.

[51] Kong, S.C., Han, Z. and Reitz, R.D., 1995. The development and application of a diesel ignition and combustion model for multidimensional engine simulation. *SAE transactions*, pp.502-518.

[52] Wang, F., Reitz, R.D., Pera, C., Wang, Z. and Wang, J., 2013. Application of generalized RNG turbulence model to flow in motored single-cylinder PFI engine. *Engineering Applications of Computational Fluid Mechanics*, *7*(4), pp.486-495.

[53] Papageorgakis, G. and Assanis, D.N., 1998. Optimizing gaseous fuel-air mixing in direct injection engines using an RNG based k-ε model. *SAE transactions*, pp.82-107.

[54] J. Shu *et al.*, "Effects of injector spray angle on combustion and emissions characteristics of a natural gas (NG)-diesel dual fuel engine based on CFD coupled with reduced chemical kinetic model," *Appl. Energy*, vol. 233–234, pp. 182–195, Jan. 2019.

[55] K. Poorghasemi, R. K. Saray, E. Ansari, B. K. Irdmousa, M. Shahbakhti, and J. D. Naber, "Effect of diesel injection strategies on natural gas/diesel RCCI combustion characteristics in a light duty diesel engine," Appl. Energy, vol. 199, pp. 430–446, 2017.

[56] Yan B, Wang H, Zheng Z, Qin Y and Yao M. The effect of combustion chamber geometry on in-cylinder flow and combustion process in a stoichiometric operation natural gas engine with EGR. Appl Therm Eng 129:199-211.

[57] Yan B, Tong L, Wang H, Zheng Z, Qin Y and Yao M. Experimental and numerical investigation of the effects of combustion chamber reentrant level on combustion characteristics and thermal efficiency of stoichiometric operation natural gas engine with EGR. Appl Therm Eng 123:1473-83, 2017.

[58] Scarcelli, R., Kastengren, A.L., Powell, C.F., Wallner, T. and Matthias, N.S., 2012, July. GE2-1 CFD and X-ray Investigation of the Characteristics of Under-Expanded Gaseous Jets (GE: Gas Engine, General Session Papers). In *The Proceedings of the International symposium on diagnostics and modeling of combustion in internal combustion engines 2012.8* (pp. 368-373). The Japan Society of Mechanical Engineers.

[59] Colin, O., Benkenida, A. and Angelberger, C., 2003. 3D modeling of mixing, ignition and combustion phenomena in highly stratified gasoline engines. *Oil & gas science and technology*, *58*(1), pp.47-62.

[60] Bray, K.N.C., 1990. Studies of the turbulent burning velocity. Proceedings of the Royal Society of London. Series A: Mathematical and Physical Sciences, 431(1882), pp.315-335.

[61] Abdel-Gayed, R.G., Bradley, D. and Lawes, M., 1987. Turbulent burning velocities: a general correlation in terms of straining rates. Proceedings of the Royal Society of London. A. Mathematical and Physical Sciences, 414(1847), pp.389-413.

[62] Haworth, D.C. and Poinsot, T.J., 1992. Numerical simulations of Lewis number effects in turbulent premixed flames. Journal of fluid mechanics, 244, pp.405-436.

[63] Trouvé, A. and Poinsot, T., 1994. The evolution equation for the flame surface density in turbulent premixed combustion. Journal of Fluid Mechanics, 278, pp.1-31.

[64] Cant, R.S., Pope, S.B. and Bray, K.N.C., 1991, January. Modelling of flamelet surface-to-volume ratio in turbulent premixed combustion. In Symposium (International) on Combustion (Vol. 23, No. 1, pp. 809-815). Elsevier.

[65] Duclos, J.M., Veynante, D. and Poinsot, T., 1993. A comparison of flamelet models for premixed turbulent combustion. Combustion and flame, 95(1-2), pp.101-117.

[66] Abdel-Gayed, R.G., Bradley, D., Hamid, M.N. and Lawes, M., 1984. Lewis number effects on turbulent burning velocity. 20th Symp.(Int.) on Combustion. *The Combustion Institute, Pittsburgh*

[67] Marble, F.E. and Broadwell, J.E. (1977) The Coherent FlameModel for Turbulent Chemical Reactions. *Purdue University Technical Report TRW*.

[68] Candel, S. and Poinsot, T.(1990) Flame Stretch and the Balance Equation for the Flame Area. *Combustion Science and Technology*, **70**, 1-15.

[69] Boudier, P., Henriot, S., Poinsot, T. and Baritaud, T. (1992) A Model for Turbulent Flame Ignition and Propagation in Piston Engines. 2*4th Symposium (International) on Combustion, The Combustion Institute*.

[70] *Duclos, J.M., Bruneaux, G. and Baritaud, T. (1996) 3D Modelling of Combustion and Pollutants in a 4valve SI Engine: Effect of Fuel and Residuals Distribution and Spark Location. SAE Paper 961964.*

[71] Bray, K.N.C., 1980. Topics in Applied Physics, PA Libby and FA Williams ed.

[72] Barrère, M., 1974. Modèles de combustion turbulente. *Revue générale de thermique française*, *148*, pp.295-308.

[73] BORGHI, R., 1985. Recent Advances in the Aerospace Science. *Plenum*, pp.117-138.

[74] Peters, N., 1986. Twenty-First (International) Symposium on Combustion. *Laminar flamelet cmcepts in turbulent combustion*.

[75] Williams, F.A., 1985. Combustion Theory Benjamin. *Cummings, Menlo Park*.

[76] Abdel-Gayed, R.G. and Bradley, D., 1985. Criteria for turbulent propagation limits of premixed flames. *Combustion and Flame*, *62*(1), pp.61-68.

[77] Abdel-Gayed, R.G., Bradley, D. and Lung, F.K., 1989. Combustion regimes and the straining of turbulent premixed flames. *Combustion and Flame*, *76*(2), pp.213-218.

[78] Poinsot, T., Veynante, D. and Candel, S., 1991, January. Diagrams of premixed turbulent combustion based on direct simulation. In *Symposium (international) on combustion* (Vol. 23, No. 1, pp. 613-619). Elsevier.

[79] Peters, N., 2001. Turbulent combustion. pp. 79

[80] Veynante, D. and Vervisch, L., 2002. Turbulent combustion modeling. *Progress in energy and combustion science*, *28*(3), pp.193-266.

[81] *Gregory P. Smith, David M. Golden, Michael Frenklach, Nigel W. Moriarty, Boris Eiteneer, Mikhail Goldenberg, C. Thomas Bowman, Ronald K. Hanson, Soonho Song, William C. Gardiner, Jr., Vitali V. Lissianski, and Zhiwei Qin http://www.me.berkeley.edu/gri_mech/*

[82] Y. Li, C-W. Zhou, K.P. Somers, K. Zhang, H.J. Curran The Oxidation of 2-Butene: A High Pressure Ignition Delay, Kinetic Modeling Study and Reactivity Comparison with Isobutene and 1-Butene Proceedings of the Combustion Institute (2017) *36(1)* 403–411.

[83] C-W. Zhou, Y. Li, E. O'Connor, K.P. Somers, S. Thion, C. Keesee, O. Mathieu, E.L. Petersen, T. A. DeVerter, M.A. Oehlschlaeger, G. Kukkadapu, C-J. Sung, M. Alrefae, F. Khaled, A. Farooq, P. Dirrenberger, P-A. Glaude, F. Battin-Leclerc, J. Santner, Y. Ju, T. Held, F.M. Haas, F.L. Dryer, H.J. Curran,"A Comprehensive experimental and modeling study of isobutene oxidation", Combust. Flame (2016) 167 353–379.

[84] U. Burke, W.K. Metcalfe, S.M. Burke, K.A. Heufer, P. Dagaut, H.J. Curran, "A Detailed Chemical Kinetic Modeling, Ignition Delay time and Jet-Stirred Reactor Study of Methanol Oxidation", Combust. Flame (2016) 165 125–136.

[85] S.M. Burke, U. Burke, O. Mathieu, I. Osorio, C. Keesee, A. Morones, E. Petersen, W. Wang, T. DeVerter, M. Oehlschlaeger, B. Rhodes, R. Hanson, D. Davidson, B. Weber, C-J. Sung, J. Santner, Y. Ju, F. Haas, F. Dryer, E. Volkov, E. Nilsson, A. Konnov, M. Alrefae, F. Khaled, A. Farooq, P. Dirrenberger, P-A. Glaude, F. Battin-Leclerc, "An experimental and modeling study of propene oxidation. Part 2: Ignition delay time and flame speed measurements", Combust. Flame (2015) 162(2) 296–314.

[86] S.M. Burke, W.K. Metcalfe, O. Herbinet, F. Battin-Leclerc, F.M. Haas, J. Santner, F.L. Dryer, H.J. Curran, "An experimental and modeling study of propene oxidation. Part 1: Speciation measurements in jet-stirred and flow reactors", Combust. Flame (2014) 161(11) 2765–2784.

[87] W.K. Metcalfe, S.M. Burke, S.S. Ahmed, H.J. Curran, "A hierarchical and comparative kinetic modeling study of C_1–C_2 hydrocarbon and oxygenated fuels", Int. J. Chem. Kinet. (2013) 45(10) 638–675.

[88] A. Kéromnès, W.K. Metcalfe, K.A. Heufer, N. Donohoe, A.K. Das, C.J. Sung, J. Herzler, C. Naumann, P. Griebel, O. Mathieu, M.C. Krejci, E.L. Petersen, W.J. Pitz, H.J. Curran "An Experimental and Detailed Chemical Kinetic Modelling Study of Hydrogen and Syngas Mixtures at Elevated Pressures" *Combustion and Flame* (2013) *160* 995–1011.

[89] https://logesoft.com/loge-software/

[90] Elia, M., Ulinski, M. and Metghalchi, M., 2001. Laminar burning velocity of methane–air–diluent mixtures. *J. Eng. Gas Turbines Power*, *123*(1), pp.190-196.

[91] Dirrenberger, P., Le Gall, H., Bounaceur, R., Herbinet, O., Glaude, P.A., Konnov, A. and Battin-Leclerc, F., 2011. Measurements of laminar flame velocity for components of natural gas. *Energy & fuels*, *25*(9), pp.3875-3884.

[92] Rozenchan, G., Zhu, D.L., Law, C.K. and Tse, S.D., 2002. Outward propagation, burning velocities, and chemical effects of methane flames up to 60 atm. *Proceedings of the Combustion Institute*, *29*(2), pp.1461-1470.

[93] Lowry, W., de Vries, J., Krejci, M., Petersen, E., Serinyel, Z., Metcalfe, W., Curran, H. and Bourque, G., 2011. Laminar flame speed measurements and modeling of pure alkanes and alkane blends at elevated pressures. *Journal of Engineering for Gas Turbines and Power*, *133*(9).

[94] Park, O., Veloo, P.S., Liu, N. and Egolfopoulos, F.N., 2011. Combustion characteristics of alternative gaseous fuels. *Proceedings of the Combustion Institute*, *33*(1), pp.887-894.

[95] Hassan, M.I., Aung, K.T. and Faeth, G.M., 1998. Measured and predicted properties of laminar premixed methane/air flames at various pressures. *Combustion and flame*, *115*(4), pp.539-550.

[96] Amirante, R., Distaso, E., Tamburrano, P. and Reitz, R.D., 2017. Laminar flame speed correlations for methane, ethane, propane and their mixtures, and natural gas and gasoline for spark-ignition engine simulations. *International Journal of Engine Research*, *18*(9), pp.951-970.

[97] Colin O, Truffin K (2011) A spark ignition model for large eddy simulation based on an FSD transport equation (ISSIM-LES). Combust Inst 33:3097–3104

[98] Sai, A.J., Balamurugan, R., Servant, C., Ravet, F. and Kumar, S.A., 2019. Applying ECFM Combustion Model to Spark Ignition Engine, Comparison with Experimental Data. In *Advances in Fluid and Thermal Engineering* (pp. 729-741). Springer, Singapore.

[99] Gicquel, L.Y., Staffelbach, G. and Poinsot, T., 2012. Large eddy simulations of gaseous flames in gas turbine combustion chambers. *Progress in energy and combustion science*, *38*(6), pp.782-817.

[100] Granet, V., Vermorel, O., Lacour, C., Enaux, B., Dugué, V. and Poinsot, T., 2012. Large-Eddy Simulation and experimental study of cycle-to-cycle variations of stable and unstable operating points in a spark ignition engine. *Combustion and Flame*, *159*(4), pp.1562-1575.

[101] Knop, V. and Essayem, E., 2013. Comparison of PFI and DI operation in a downsized gasoline engine. *SAE International Journal of Engines*, *6*(2), pp.941-952.

[102] Chevillard, S., Colin, O., Bohbot, J., Wang, M., Pomraning, E. and Senecal, P.K., 2017. *Advanced methodology to investigate knock for downsized gasoline direct injection engine using 3D RANS simulations* (No. 2017-01-0579). SAE Technical Paper.

[103] Meneveau, C. and Poinsot, T., 1991. Stretching and quenching of flamelets in premixed turbulent combustion. *Combustion and Flame*, *86*(4), pp.311-332.

[104] Chen, Z., Burke, M.P. and Ju, Y., 2009. Effects of compression and stretch on the determination of laminar flame speeds using propagating spherical flames. *Combustion Theory and modelling*, *13*(2), pp.343-364.

[105] Duclos, J.M. and Zolver, M. (1998) 3D Modeling of Intake, Injection and Combustion in a DI-SI Engine under Homogeneous and Stratified Operating Conditions. *International Symposium COMODIA*.

[106] Knop, V., Benkenida, A., Jay, S. and Colin, O., 2008. Modelling of combustion and nitrogen oxide formation in hydrogen-fuelled internal combustion engines within a 3D CFD code. *International Journal of Hydrogen Energy*, *33*(19), pp.5083-5097.

[107] M. Baratta, D. Misul, E. Spessa, L. Viglione, G. Carpegna, and F. Perna, "Experimental and numerical approaches for the quantification of tumble intensity in high-performance SI engines," *Energy Convers. Manag.*, vol. 138, pp. 435–451, 2017.

[108] B. Yan, L. Tong, H. Wang, Z. Zheng, Y. Qin, and M. Yao, "Experimental and numerical investigation of the effects of combustion chamber reentrant level on combustion characteristics and thermal efficiency of stoichiometric operation natural gas engine with EGR," *Appl. Therm. Eng.*, vol. 123, pp. 1473–1483, Aug. 2017.

[109] Warsi, Z.U., 2005. *Fluid dynamics: theoretical and computational approaches*. CRC press.

[110] Launder BE and Spalding DB. The numerical computation of turbulent flows. *Comput Methods Appl Mech Eng* 3(2):269-89, 1974.

[111] Kaario, O., Nuutinen, M., Lehto, K. and Larmi, M., 2010. Real gas effects in high-pressure engine environment. *SAE International Journal of Engines*, *3*(1), pp.546-555.

[112] Angelberger, C., Poinsot, T., and Delhaye, B., "Improving Near-Wall Combustion and Wall Heat Transfer Modeling in SI Engines Computations," SAE Paper 972881, 1997. DOI:10.4271/972881

[113] Ma, P.C., Ewan, T., Jainski, C., Lu, L., Dreizler, A., Sick, V. and Ihme, M., 2017. Development and analysis of wall models for internal combustion engine simulations using high-speed micro-PIV measurements. *Flow, Turbulence and Combustion*, *98*(1), pp.283-309.

[114] Rhie, C.M., and Chow, W.L., "Numerical Study of the Turbulent Flow Past an Airfoil with Trailing Edge Separation," AIAA Journal, 21(11), 1525-1532, 1983. DOI: 10.2514/3.8284

[115] Baratta, M. and Rapetto, N., 2014. Fluid-dynamic and numerical aspects in the simulation of direct CNG injection in spark-ignition engines. *Computers & Fluids*, *103*, pp.215-233.

[116] Scarcelli, R., Wallner, T., Matthias, N., Salazar, V. and Kaiser, S., 2011. *Numerical and optical evolution of gaseous jets in direct injection hydrogen engines* (No. 2011-01-0675). SAE Technical Paper.

[117] K. Richards, D. Probst, E. Pomraning, P. K. Senecal, and R. Scarcelli, "The observation of cyclic variation in engine simulations when using rans turbulence modeling," *ASME 2014 Intern. Combust. Engine Div. Fall Tech. Conf. ICEF 2014*, vol. 2, pp. 1–19, 2014.

[118] R. Scarcelli, K. Richards, E. Pomraning, P. K. Senecal, T. Wallner, and J. Sevik, "Cycle-to-Cycle Variations in Multi-Cycle Engine RANS Simulations," *SAE Tech. Pap.*, 2016.

[119] Scarcelli, R., Sevik, J., Wallner, T., Richards, K., Pomraning, E. and Senecal, P.K., 2015, November. Capturing cyclic variability in EGR dilute SI combustion using multi-cycle RANS. In *Internal Combustion Engine Division Fall Technical Conference* (Vol. 57281, p. V002T06A010). American Society of Mechanical Engineers.

[120] Brunt, M.F., Rai, H. and Emtage, A.L., 1998. The calculation of heat release energy from engine cylinder pressure data. *SAE transactions*, pp.1596-1609.

[121] Zhang, Z., Zhang, H., Wang, T. and Jia, M., 2014. Effects of tumble combined with EGR (exhaust gas recirculation) on the combustion and emissions in a spark ignition engine at part loads. *Energy*, *65*, pp.18-24.

[122] Szybist, J.P. and Splitter, D., 2016. Effects of fuel composition on EGR dilution tolerance in spark ignited engines. *SAE International Journal of Engines*, *9*(2), pp.819-831.

[123] Haskara, I., Zhu, G.G. and Winkelman, J., 2006, June. Multivariable EGR/spark timing control for IC engines via extremum seeking. In *2006 American Control Conference* (pp. 6-pp). IEEE.

[124] Lou, D., Ren, Y., Zhang, Y. and Sun, X., 2020. Study on the Effects of EGR and Spark Timing on the Combustion, Performance, and Emissions of a Stoichiometric Natural Gas Engine. *ACS omega*, *5*(41), pp.26763-26775.

[125] Baratta, M., d'Ambrosio, S., Misul, D. and Spessa, E., 2014. Effects of H2 addition to compressed natural gas blends on cycle-to-cycle and cylinder-to-cylinder combustion variation in a spark-ignition engine. *Journal of engineering for gas turbines and power*, *136*(5).

[126] Baratta, M., D'Ambrosio, S. and Misul, D.A., 2013. Performance and emissions of a turbocharged spark ignition engine fuelled with CNG and CNG/hydrogen blends (No. 2013-01-0866). *SAE Technical Paper*.

[127] Wang, J., Huang, Z., Tang, C. and Zheng, J., 2010. Effect of hydrogen addition on early flame growth of lean burn natural gas–air mixtures. *international journal of hydrogen energy*, *35*(13), pp.7246-7252.

[128] Ma, F., Liu, H., Wang, Y., Li, Y., Wang, J. and Zhao, S., 2008. Combustion and emission characteristics of a port-injection HCNG engine under various ignition timings. *International Journal of Hydrogen Energy*, *33*(2), pp.816-822.

[129] Halter, F., Chauveau, C. and Gökalp, I., 2007. Characterization of the effects of hydrogen addition in premixed methane/air flames. *International Journal of Hydrogen Energy*, *32*(13), pp.2585-2592.

[130] Hu, E., Huang, Z., Liu, B., Zheng, J. and Gu, X., 2009. Experimental study on combustion characteristics of a spark-ignition engine fueled with natural gas–hydrogen blends combining with EGR. *International journal of hydrogen energy*, *34*(2), pp.1035-1044.

[131] Huang, Z., Zhang, Y., Zeng, K., Liu, B., Wang, Q. and Jiang, D., 2007. Natural gas− hydrogen− air premixed mixture combustion with a constant volume bomb. *Energy & fuels*, *21*(2), pp.692-698.

[132] Serrano, D., Laget, O., Soleri, D., Richard, S., Douailler, B., Ravet, F., Moreau, M. and Dioc, N., 2010. Effects of Methane/Hydrogen blends on engine operation: experimental and numerical investigation of different combustion modes. *SAE International Journal of Engines*, *3*(2), pp.223-243.

[133] http://www.gason.eu/documents/get_doc/1168.

[134] Paredi, D., Lucchini, T., D'Errico, G., Onorati, A., Golini, S. and Rapetto, N., 2017. Gas exchange and injection modeling of an advanced natural gas engine for heavy duty applications. In *SAE 13th International Conference on Engines and Vehicles, ICE 2017* (Vol. 2017, pp. 1-15). SAE International.

[135] IEA, Transport sector CO2 emissions by mode in the Sustainable Development Scenario, 2000-2030, IEA, Paris https://www.iea.org/data-and-statistics/charts/transport-sector-co2-emissions-by-mode-in-the-sustainable-development-scenario-2000-2030

[136] Sevik, J., Pamminger, M., Wallner, T., Scarcelli, R., Boyer, B., Wooldridge, S., Hall, C. and Miers, S., 2016. Influence of injector location on part-load performance characteristics of natural gas direct-injection in a spark ignition engine. *SAE International Journal of Engines*, *9*(4), pp.2262-2271.

[137] Senecal, K. and Leach, F., 2021. Racing Toward Zero: The Untold Story of Driving Green.

[138] Di Maio, D., Beatrice, C., Fraioli, V., Napolitano, P., Golini, S. and Rutigliano, F.G., 2019. Modeling of three-way catalyst dynamics for a compressed natural gas engine during lean–rich transitions. Applied Sciences, 9(21), p.4610.

[139] Gremminger, A., Pihl, J., Casapu, M., Grunwaldt, J.D., Toops, T.J. and Deutschmann, O., 2020. PGM based catalysts for exhaust-gas after-treatment under typical diesel, gasoline and gas engine conditions with focus on methane and formaldehyde oxidation. Applied Catalysis B: Environmental, 265, p.118571.

[140] Ren, Y., Lou, D., Tan, P., Zhang, Y. and Sun, X., 2021. Emission reduction characteristics of after-treatment system on natural gas engine: Effects of platinum group metal loadings and ratios. Journal of Cleaner Production, 298, p.126833.

[141] Chen, J., Wu, Y., Hu, W., Qu, P., Zhang, G., Granger, P., Zhong, L. and Chen, Y., 2020. New insights into the role of Pd-Ce interface for methane activation on monolithic supported Pd catalysts: A step forward the development of novel PGM Three-Way Catalysts for natural gas fueled engines. Applied Catalysis B: Environmental, 264, p.118475.